TOWARD NEXT-GENERATION NANOPHOTONIC DEVICES

DOCTORAL THESIS

Dissertation submitted by

RENWEN YU

for the degree of

Doctor of Philosophy

Supervisor: PROF. FRANCISCO JAVIER GARCÍA DE ABAJO

ICFO - INSTITUT DE CIÈNCIES FOTÒNIQUES

BARCELONA, 2019

This doctoral dissertation has been carried out in the Nanophotonics Theory Group at ICFO - The Institute of Photonic Sciences in Castelldefels, Barcelona, thanks to the funding of a predoctoral grant from the FPI programme of the Ministry of Economy and Competitiveness (MINECO), of the Spanish Government (Ref. BES-2015-072184).

To my parents and Yingying

格物以致知　宁静以致远

《礼记·大学》
《诫子书》

Acknowledgments

Time flies, indeed. Without a doubt, it has been a fruitful, busy, and enjoyable journey. Although during the last five years it was not all the way as sunny as the first day when I arrived in Castelldefels, I could always find an umbrella during those rainy days (which are of course rather rare due to the weather here in Barcelona). This is why I would like to thank here all those who have passed me the umbrella and helped me make this journey possible.

First of all, I would like to thank Javier for continuously passing me his wisdom and trustfully giving me lots of opportunities during my PhD study. Fortunately for me, it has been a privilege to grow as a scientist under his dedicated guidance, without which it would be impossible for the existence of this thesis. His great passion for research, creative enthusiasm for physics, and active optimism for life will always inspire me wherever I go, both in work and in life.

In addition to Javier, I would like to thank all the members in the Nanophotonics Theory group at ICFO to create such a wonderful atmosphere: Andrea, Joel, José, Sandra, Ivan, Ana, Christin, Lijun, Wei, Deng, Álvaro, Zaka, Vahagn, Eduardo, Valerio, and George. Thank you all for the company not only in the office but also in the ICFO cafeteria, conferences... and restaurants.

Specifically, I would like to thank my initial office mates: Dr. Andrea Marini and Dr. Joel Cox for their willingness to answer many naive questions from a PhD student and for many other interesting and unforgettable discussions. I would like to thank José for helping me translate the Abstract and for his great kindness since continuously. I would like to thank the Chinese community at ICFO: Lijun, Wei, Deng, Hanyu, and Quan for the cozy company. Moreover, I would like to thank the native Spanish speakers in the group: José, Sandra, Ivan, and Álvaro for their numerous selfless assistanc in the post office, police station, bank, hospital,...

As a theoretician, I was very lucky to collaborate with many outstanding experimentalists during my PhD period. First, I would like to thank Prof. Valerio Pruneri and Prof. Niek van Hulst together with their group members at ICFO: Rinu, Dani, Josep, Alex, Matz, Albert, and Dhriti for delivering several beautiful experiments. Also, I would like to thank Prof. Claus Ropers, Prof. Ramón Álvarez-Puebla, and Prof. Miguel

Correa-Duarte together with their groups for the impressive experimental outcomes. I would like to thank Prof. Luis Liz-Marzán for the fruitful collaboration. Furthermore, I am grateful to Prof. Fengnian Xia for his generous support and hosting my visit to Yale University, and also to all his group members to make my three-month stay pleasant: Qiushi, Shaofan, Cheng, Chao, Bingchen, Xiaolong, and Chen. Their beautiful experiments greatly improve this thesis.

I would like to thank Yang, Yunlu, Haotian, Amanda, Jue, and Xingyue for their enthusiastic hospitality and assistance when I was traveling in US. I would also like to thank Lichun, Hao, and Jiamin for their warm reception when I was traveling in Europe.

Last but not least, I would like to thank my parents and my family for their endless love and support. Thanks to Yingying for having accompanied me on this journey, for having always been willing to encourage and take care of me, and for all those lovely distractions during my PhD study.

Contents

List of Figures

List of Tables

List of Acronyms

2D Two-Dimensional

3D Three-Dimensional

BEM Boundary Element Method

BN Boron Nitride

CW Continuous Wave

DC Direct Current

DLC Diamond-Like Carbon

DOS Density of State

FWHM Full Width at Half Maximum

FP Fabry-Perot

GDPR Graphene-Disk Plasmonic Resonator

GHQD Graphene Hexagon Quantum Dot

GNH Graphene Nanohexagon

GNR Graphene Nanoribbon

HTP Heat Transfer Power

LDOS Local Density of Optical States

LSP Localized Surface Plasmon

NIR Near-Infrared

NNH Nearest-Neighbor Hopping

PWF Plasmon Wave Function

RPA Random-Phase Approximation

SERS Surface-Enhanced Raman Spectroscopy

SHG Second-Harmonic Generation

SPP Surface Plasmon-Polariton

TCE Thermal Carrier Excitation

TE Transverse Electric

TM Transverse Magnetic

UGM Ultrathin Graphene-Metal Hybrid Film

Abstract

The understanding and control of light-matter interactions at the nanoscale are of great importance for the design of efficient and compact nanophotonic devices for diverse applications such as energy production, communications, and biomedicine. It is also a fruitful playground for academic investigations at the intersection of light (photon), electron, and atomic-lattice (phonon) interactions.

Graphene, a truly two-dimensional material composed of carbon atoms, possessing extraordinary electrical, thermal, and optical properties, has emerged as a promising platform for strong light-matter interaction, which makes graphene a promising candidate as a major building block for the next-generation nanophotonic devices.

In this thesis, we aim to explore several novel designs of nanostructures based on graphene to realize various functionalities. We briefly introduce the fundamental concepts and theoretical models used in this thesis in Chapter 1. Following the macroscopic analytical method outlined in the first chapter, in Chapter 2 we show that simple simulation methods allow us to accurately describe the optical response of plasmonic nanoparticles, including retardation effects, without the requirement of vast computational resources.

We then move to our proposed first type of device: optical modulators. We explore graphene sheets coupled to different kinds of optical resonators to enhance the light intensity at the graphene plane, and so also its absorption, which can be switched on/off and modulated through varying the level of doping, as explored in Chapter 3. Unity-order changes in the transmission and absorption of incident light are predicted upon electrical doping of graphene.

Heat deposition via light absorption can severely degrade the performance and limit the lifetime of nano-devices (*e.g.*, aforementioned optical modulators), which makes the manipulation of nanoscale heat sources/flows crucial. In Chapter 4, we exploit the extraordinary optical and thermal properties of graphene to show that ultrafast radiative heat transfer can take place between neighboring nanostructures facilitated by graphene plasmons, where photothermally induced effects on graphene plasmons are taken into account. Our findings reveal a new regime for the nanoscale thermal

management, in which non-contact heat transfer becomes a leading mechanism of heat dissipation.

Apart from the damage caused by heat deposition, generated thermal energy can be in fact used as a tool for photodetection (*e.g.*, silicon bolometers for infrared photodetection). In Chapter 5, we show that the excitation of a single plasmon in a graphene nanojunction produces profound modifications in its electrical properties through optical heating, which we then use to demonstrate an efficient mid-infrared photodetector working at room temperature based on theoretical predictions that are corroborated in an experimental collaboration with the group of Prof. Fengnian Xia in Yale University.

Finally, in Chapter 6, we show through microscopic quantum-mechanical simulations, introduced in the first chapter, that both the linear and nonlinear optical responses of graphene nanostructures can be dramatically altered by the presence of a single neighboring molecule that carries either an elementary charge or a small permanent dipole. Based on these results, we claim that nanographenes can serve as an efficient platform for detecting charge- or dipole-carrying molecules.

In summary, in this thesis we first develop a universal macroscopic analytical model to calculate the optical response of plasmonic nanoparticles. By using this method along with atomistic quantum-mechanical simulations, we explore and propose a series of nanophotonic devices based on graphene, ranging from optical modulators to sensors displaying different types of functionalities. We hope that these proposals can provide deep insight and general guidance for the development of next-generation ultra-compact nanophotonic devices.

Resumen

La comprensión y el control de la interacción luz-materia en la nanoescala son de gran importancia para el diseño de dispositivos nanofotónicos eficientes y compactos, con aplicaciones en campos tan dispares como la producción de energía, las comunicaciones, el control de calidad o la biomedicina. Asimismo, la nanofotónica es también un campo fructífero para la investigación académica, por ejemplo en el estudio fundamental de la interacción entre la luz (fotones) y las partículas presentes en la materia, como los electrones y los fonones.

Entre todos los materiales utilizados en nanofotónica, el grafeno (un material verdaderamente bidimensional compuesto de átomos de carbono), gracias a sus extraordinarias propiedades eléctricas, térmicas y ópticas, ha surgido como una plataforma prometedora para una interacción fuerte entre la luz y la materia, convirtiéndolo en un candidato prometedor e importante en el diseño de la próxima generación de dispositivos nanofotónicos.

En esta tesis, pretendemos explorar varios diseños novedosos de nanoestructuras basadas en grafeno, con diversas funcionalidades. Tras presentar brevemente los conceptos fundamentales y los modelos teóricos utilizados en esta tesis en el Capítulo 1, en el Capítulo 2 mostramos la posibilidad de describir la respuesta de nanopartículas plasmónicas (incluyendo efectos de retardo) mediante métodos de simulación semi-analíticos sencillos y sin la necesidad de emplear grandes recursos computacionales.

Posteriormente, empleamos estos modelos en el desarrollo de un primer tipo de dispositivo: moduladores ópticos. Añadiendo láminas de grafeno acopladas a diferentes tipos de resonadores ópticos, podemos mejorar la intensidad de la luz en el plano del grafeno, y por lo tanto también su nivel de absorción, la cual puede ser modulada a voluntad mediante el nivel de dopado electrostático del grafeno, como se explora en el Capítulo 3. Los modelos empleados predicen cambios en la transmisión del orden de la unidad, produciendo así la absorción total por parte del dispositivo de la luz incidente.

En esta clase de dispositivos, así como en todos los dispositivos nanofotónicos, la producción de calor mediante la absorción de la luz puede degradar severamente

su rendimiento, así como limitar su vida útil, lo que hace que la manipulación de la fuente y el flujo de calor en la nanoescala sea una componente crucial del desarrollo. En el Capítulo 4, empleamos las extraordinarias propiedades ópticas y térmicas del grafeno para mostrar que puede tener lugar una transferencia ultrarrápida de calor radiativo entre nanoestructuras vecinas, facilitada por los plasmones del grafeno, los cuales a su vez experimentan efectos fototérmicos asociados con este proceso de disipación. Nuestros hallazgos revelan un nuevo régimen para la energía térmica a nanoescala, en la que la transferencia de calor radiativa se convierte en el mecanismo principal de disipación de calor.

Además de los daños causados por la deposición de calor, la energía térmica generada puede ser de hecho usada como herramienta para la fotodetección: tal es el caso, por ejemplo, de los bolómetros de silicona, empleados para la fotodetección por infrarrojos. En el Capítulo 5, mostramos que la excitación de un solo plasmón en una unión de grafeno altera radicalmente sus propiedades eléctricas debido al calentamiento óptico. Este hecho puede ser empleado para demostrar el funcionamiento eficaz de un fotodetector en la región media de los infrarrojos a temperatura ambiente, tanto a través de predicciones teóricas como su corroboración experimental (en colaboración con el grupo del Prof. Fengnian Xia de la Universidad de Yale).

Finalmente, en el Capítulo 6, mostramos a través de simulaciones mecánico-cuánticas (introducidas en el Capítulo 1), que tanto la respuesta óptica lineal como la no lineal de las nanoestructuras de grafeno pueden ser dramáticamente alteradas por la presencia de una sola molécula vecina que transporte o bien una carga elemental o un dipolo permanente. En base a estos resultados, afirmamos que las estructuras de grafeno nanoscópicas podrían ser una plataforma eficiente para detectar moléculas portadoras de carga o dipolos.

En resumen, en esta tesis primero desarrollamos un modelo analítico con carácter universal para calcular la respuesta óptica de las nanopartículas plasmónicas a escala macroscópica. Usando este método, en conjunto con simulaciones mecánico-cuánticas de la estructura atómica, exploramos y proponemos una serie de dispositivos nanofotónicos basados en el grafeno (desde moduladores ópticos a sensores) con toda una serie de funcionalidades aumentadas. Esperamos que estas propuestas puedan proporcionar una profunda visión y orientación para el desarrollo de la próxima generación de dispositivos ultracompactos basados en nanofotónica.

1
Introduction

Optics is the science of light, which has been visible and accessible to everyone since ancient times. Indeed, many developments in optics, such as the invention of the laser as a coherent light source, the successful reduction of optical losses in optical fibers, and the revolutionary introduction of semiconductor-based photonic devices, have been central to the formulation of fundamental scientific principles as well as various modern technologies, ranging from submarine communications cables deep in the ocean to highly-integrated biosensors on a chip, therefore covering a manifestly diverse range of applications and permitting us to explain a wide range of natural phenomena on purely rational grounds.

Among all the advances in the field of optics, the emergence of the fascinating field of nanophotonics provides a prolific platform to investigate light-matter interactions at the nanoscale. When the characteristic size of the structure is comparable to the wavelength of light, a plethora of extraordinary optical effects are triggered, such as enhanced light absorption/scattering from colloidal nanostructures,[1] sub-wavelength light focusing,[2] and perfect lens.[3]

In the wake of this background, plasmons, the collective oscillations of electrons in metals, have acquired major importance in the field of nanophotonics. They possess the ability of concentrating light down to nanometer-sized regions, where the optical field intensity can be amplified by several orders of magnitude.[4] These properties have been extensively used to develop sensing techniques that can detect the presence of single molecules,[5–9] enhance optoelectronic devices for light harvesting,[10,11] spectrometry,[12–14] and photocatalysis,[15–20] trigger efficient nonlinear processes at the nanoscale,[21–23] and assist tumor diagnosis/treatment,[24,25] among other feasts.

As an introduction to understand these applications, and further as a background on which the main findings of this thesis are based, in this chapter we begin by reviewing some fundamentals of plasmonics in the macroscopic and classical regime, and introduce a powerful theoretical framework to describe the optical response of plasmonic nanostructures. We continue with a microscopic and quantum description to characterize the linear/nonlinear plasmonic response of nanostructures with dimensions comparable to the electron mean free path. We conclude by introducing the foundations of nanoscale heat transport induced by plasmons.

1.1 Fundamentals of plasmonics

1.1.1 Classical electromagnetism

From a classical and macroscopic point of view, in order to study light-matter interactions, light can be described as an electromagnetic wave, generated by free charge ρ

and current **j** density distributions. Such interactions can be described by Maxwell's macroscopic equations, which we write in Gaussian units (used throughout this thesis) as[26]

$$\nabla \cdot \mathbf{D}(\mathbf{r},t) = 4\pi\rho(\mathbf{r},t), \tag{1.1a}$$

$$\nabla \cdot \mathbf{B}(\mathbf{r},t) = 0, \tag{1.1b}$$

$$\nabla \times \mathbf{E}(\mathbf{r},t) = -\frac{1}{c}\frac{\partial}{\partial t}\mathbf{B}(\mathbf{r},t), \tag{1.1c}$$

$$\nabla \times \mathbf{H}(\mathbf{r},t) = \frac{1}{c}\frac{\partial}{\partial t}\mathbf{D}(\mathbf{r},t) + \frac{4\pi}{c}\mathbf{j}(\mathbf{r},t), \tag{1.1d}$$

where **E** is the electric field, **D** is the electric displacement field, **H** is the magnetic field, **B** is the magnetic induction, and c is the speed of light in vacuum. By combining Eqs. 1.1a and 1.1d, one can find that local conservation of charge can be obtained from Maxwell's equations as

$$\frac{\partial}{\partial t}\rho(\mathbf{r},t) + \nabla \cdot \mathbf{j}(\mathbf{r},t) = 0, \tag{1.2}$$

which is known as the continuity equation.

The effect of the bound charge and current densities in matter is incorporated into the electric displacement and magnetic fields, which essentially specify the dependence of polarization and magnetization inside a material on the electric and magnetic fields, leading to the so-called constitutive relations that express **D** and **B** in terms of **E** and **H**. Specifically, in a homogenous, isotropic, non-magnetic, and linear material, the constitutive relations can be expressed as

$$\mathbf{D}(\mathbf{r},t) = \int\int d\mathbf{r}'dt'\epsilon(\mathbf{r}-\mathbf{r}',t-t')\mathbf{E}(\mathbf{r}',t'), \tag{1.3a}$$

$$\mathbf{B}(\mathbf{r},t) = \mathbf{H}(\mathbf{r},t), \tag{1.3b}$$

where $\epsilon(\mathbf{r}-\mathbf{r}',t-t')$ is the permittivity (dielectric or response function) of the material.

Equation 1.3a describes nonlocality in both space and time, which means that the electric displacement field induced at the space point **r** and time t may depend on the electric field at different space-time points $\mathbf{r}' \neq \mathbf{r}$ and $t' \neq t$. From the causality condition, the electric displacement field $\mathbf{D}(\mathbf{r},t)$ at time t cannot depend on the electric field $\mathbf{E}(\mathbf{r}',t')$ at later times t', and it follows that $\epsilon(\mathbf{r}-\mathbf{r}',t-t') = 0$ if $t < t'$. We now perform a time-Fourier transform according to

$$\mathbf{E}(\mathbf{r},\omega) = \int dt\,\mathbf{E}(\mathbf{r},t)e^{i\omega t}, \tag{1.4}$$

which allows us to work in frequency space ω, so that the time dependence $t-t'$ of the response function ϵ translates to a frequency ω dependence according to

$$\mathbf{D}(\mathbf{r},\omega) = \int d\mathbf{r}'\epsilon(\mathbf{r}-\mathbf{r}',\omega)\mathbf{E}(\mathbf{r}',\omega). \tag{1.5}$$

In this scenario, we say that the medium is temporally dispersive (*i.e.*, the permittivity depends on frequency). Additionally, the spatial dispersion, also known as nonlocality, plays a pivotal role only under extreme conditions, such as when the characteristic length of the structure approaches the few-nanometer/sub-nanometer range. In the local approximation we have $\epsilon(\mathbf{r}-\mathbf{r}',\omega) = \delta(\mathbf{r}-\mathbf{r}')\epsilon(\omega)$ in a homogenous medium, and thus, the constitutive relations given in Eq. 1.3 reduce in the frequency domain to

$$\mathbf{D}(\mathbf{r},\omega) = \epsilon(\omega)\mathbf{E}(\mathbf{r},\omega), \tag{1.6a}$$
$$\mathbf{B}(\mathbf{r},\omega) = \mathbf{H}(\mathbf{r},\omega). \tag{1.6b}$$

Maxwell's equations together with the continuity equation displayed in Eqs. 1.1 and 1.2 can be also rewritten in the frequency domain after applying the time-Fourier transform (see Eq. 1.4) as

$$\nabla\cdot\mathbf{D}(\mathbf{r},\omega) = 4\pi\rho(\mathbf{r},\omega), \tag{1.7a}$$
$$\nabla\cdot\mathbf{B}(\mathbf{r},\omega) = 0, \tag{1.7b}$$
$$\nabla\times\mathbf{E}(\mathbf{r},\omega) = \mathrm{i}k\mathbf{B}(\mathbf{r},\omega), \tag{1.7c}$$
$$\nabla\times\mathbf{H}(\mathbf{r},\omega) = -\mathrm{i}k\mathbf{D}(\mathbf{r},\omega) + \frac{4\pi}{c}\mathbf{j}(\mathbf{r},\omega), \tag{1.7d}$$
$$\nabla\cdot\mathbf{j}(\mathbf{r},\omega) = \mathrm{i}\omega\rho(\mathbf{r},\omega), \tag{1.7e}$$

where $k = \omega/c$ is the wave vector of light.

When the system is composed of more than one material, the electromagnetic fields must satisfy a series of interface conditions at the boundaries separating every two media. These boundary conditions can be derived from the integral forms of Maxwell's equations as[26]

$$\mathbf{n}_{12}\times(\mathbf{E}_2-\mathbf{E}_1) = 0, \tag{1.8a}$$
$$\mathbf{n}_{12}\cdot(\mathbf{D}_2-\mathbf{D}_1) = 4\pi\sigma_s, \tag{1.8b}$$
$$\mathbf{n}_{12}\cdot(\mathbf{B}_2-\mathbf{B}_1) = 0, \tag{1.8c}$$
$$\mathbf{n}_{12}\times(\mathbf{H}_2-\mathbf{H}_1) = \frac{4\pi}{c}\mathbf{j}_s, \tag{1.8d}$$

where $\mathbf{n}_{12}$ is the normal vector pointing from medium 1 to the medium 2, and $\sigma_s/\mathbf{j}_s$ is the surface charge/current density at the interface.

Applying the interface conditions displayed in Eq. 1.8, one can obtain the so-called Fresnel coefficients describing the reflection and transmission of light at a planar interface between two materials in terms of reflection r and transmission t coefficients as

$$r_s = \frac{k_{1\perp} - k_{2\perp}}{k_{1\perp} + k_{2\perp}}, \qquad t_s = 1 + r_s, \tag{1.9a}$$

$$r_p = \frac{\epsilon_2 k_{1\perp} - \epsilon_1 k_{2\perp}}{\epsilon_2 k_{1\perp} + \epsilon_1 k_{2\perp}}, \qquad t_p = \sqrt{\frac{\epsilon_2}{\epsilon_1}} \frac{k_{1\perp}}{k_{2\perp}} \left(1 - r_p\right), \tag{1.9b}$$

where the subscript s/p corresponds to s/p-polarized light (electric/magnetic fields perpendicular to the plane of incidence), and $k_{i\perp} = \sqrt{k^2 \epsilon_i - k_\parallel^2}$ is the normal component (perpendicular to the interface) of the wave vector in the medium i (of permittivity ϵ_i) with the parallel component of the wave vector $\mathbf{k}_\parallel$ conserved across the interface.

1.1.2 Dielectric functions of noble metals

Noble metals play a particularly important and active role in the field of plasmonics, serving as the building blocks for many plasmonic nanosystems (see next subsection). Their optical response in a broad frequency range can be understood as a gas of free electrons moving in a fixed background of positively charged ions. In particular, gold, silver, and copper exhibit a Drude-like response[27] that can be characterized through the permittivity

$$\epsilon_m(\omega) = \epsilon_b - \frac{\omega_p^2}{\omega\left(\omega + i\tau^{-1}\right)}, \tag{1.10}$$

where τ is the relaxation time of the electron gas, ϵ_b accounts for the residual polarization of the background of positive ion cores and interband transitions, and $\omega_p = \sqrt{4\pi n e^2 / m_e}$ is the plasma frequency with e the elementary charge, n the electron density, and m_e the electron mass. Values of the parameters ϵ_b, ω_p, and τ are shown in Table 1.1 for common good plasmonic metals. This model provides a reasonable description of the measured dielectric function[28] using constant values of ϵ_b for wavelengths above the interband transitions (solid and dotted curves in Fig. 1.1). Those transitions contribute with a polarization component to the real part of ϵ_m (the ϵ_b term in Eq. 1.10) and also with an increase in the imaginary part (*i.e.*, actual excitations) at short wavelengths below $\sim 370\,\text{nm}$, $\sim 500\,\text{nm}$, and $\sim 550\,\text{nm}$ for Ag, Au, and Cu, respectively. In those regions, Eq. 1.10 can be still applied by including a frequency dependence in ϵ_b, as shown in Fig. 1.1 (dashed curves) and Table 1.1 (see caption). Typically, we are interested in the frequency range $\omega < \omega_p/\sqrt{\epsilon_b}$, where noble metals are dominated by a Drude-like behavior, so their character remains metallicity, defined as $\text{Re}\{\epsilon_m\} < 0$ here, while $|\text{Re}\{\epsilon_m\}| \gg |\text{Im}\{\epsilon_m\}|$.

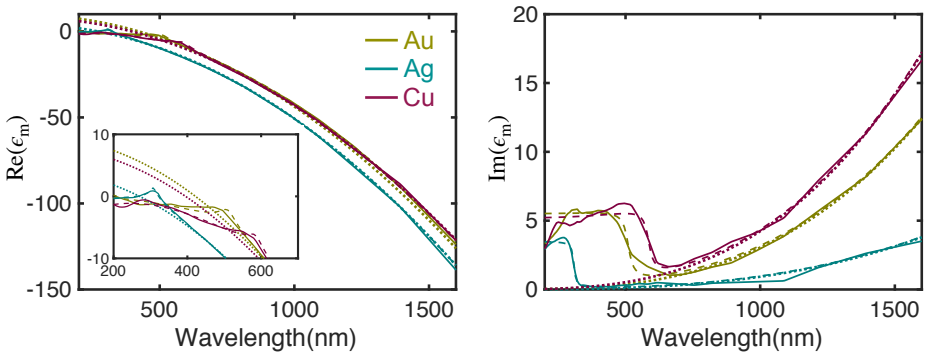

Figure 1.1: **Dielectric functions of noble metals.** We show the dielectric functions of gold, silver, and copper taken from tabulated measured data (solid curves) compared with the Drude model (Eq. 1.10, dotted curves) and a more accurate analytical fit (dashed curves) using the parameters listed in Table 1.1. Adapted from Ref. [29].

	ϵ_b	$\hbar\omega_p$ (eV)	$\hbar\tau^{-1}$ (eV)	τ (fs)	A	B	C	$\hbar\omega_1$ (eV)	$\hbar\tau_1^{-1}$ (eV)	$\hbar\omega_2$ (eV)
Au	9.5	9.06	0.071	9.3	0.132	-1.755	20.43	2.43	0.0716	1.52
Ag	4.0	9.17	0.021	31	-9.71	-1.111	13.77	4.02	0.0760	18.5
Cu	8.0	8.88	0.103	6.4	-4.36	-1.655	12.31	2.12	0.0528	5.43

Table 1.1: Parameters entering the Drude dielectric function $\epsilon_m(\omega) = \epsilon_b - \omega_p^2/\omega(\omega + i\tau^{-1})$ with either a constant value of ϵ_b (Fig. 1.1, dotted curves) or with this constant replaced by an ω-dependent analytical fitting function $\epsilon_b(\omega) = A + B\log\left[(\omega_1 - \omega - i\tau_1^{-1})/(\omega_1 + \omega + i\tau_1^{-1})\right] + C\exp(-\omega/\omega_2)$ (Fig. 1.1, dashed curves) for gold, silver, and copper. Adapted from Ref. [29].

1.1.3 Surface plasmon polaritons

Surface plasmon polaritons (SPPs) are surface waves propagating at the interface between a dielectric (of permittivity ϵ_d, which is typically real and positive) and a metal (of permittivity ϵ_m with a small positive imaginary part and a negative real part), confined in the direction perpendicular to the interface. They originate from the surface charge oscillations coupled to the incident electromagnetic field at the interface. Since they are the eigensolutions/eigenmodes of the metal-dielectric interfaces, they are subject to Maxwell's equations in the absence of external sources, which in the wave-equation representation reduce to

$$\nabla \times \nabla \times \mathbf{E}(\mathbf{r},\omega) - k^2 \epsilon(\mathbf{r},\omega)\mathbf{E}(\mathbf{r},\omega) = 0. \tag{1.11}$$

Additionally, these eigenmodes correspond to the poles of the Fresnel coefficients given in Eq. 1.9. Therefore, for the s-polarization, we have $k_{\mathrm{d}\perp} = -k_{\mathrm{m}\perp}$, which contradicts the mode confinement requirement $\mathrm{Im}\{k_{\mathrm{d}\perp}\} > 0$ and $\mathrm{Im}\{k_{\mathrm{m}\perp}\} > 0$. In contrast, for p-polarization, we find $\epsilon_\mathrm{d} k_{\mathrm{m}\perp} = -\epsilon_\mathrm{m} k_{\mathrm{d}\perp}$ (this means that SPPs only exist at interfaces between two materials of opposite signs of $\mathrm{Re}\{\epsilon\}$) and obtain the dispersion relation of SPPs as

$$k_\mathrm{spp} = \frac{\omega}{c}\sqrt{\frac{\epsilon_\mathrm{m}\epsilon_\mathrm{d}}{\epsilon_\mathrm{m}+\epsilon_\mathrm{d}}}. \tag{1.12}$$

Figure 1.2 shows the dispersion relation of SPPs at an air-gold interface, where we use the Drude model (Eq. 1.10 with parameters $\epsilon_\mathrm{b} = 9.5$, $\hbar\omega_\mathrm{p} = 9.06\,\mathrm{eV}$, and $\hbar\tau^{-1} = 0.071\,\mathrm{eV}$ as listed in Table 1.1) to describe the gold permittivity. In the low-frequency range (mid-infrared or below), the dispersion follows closely the light line, with slightly higher plasmon wave vector than that of light, and the surface wave is widely extended along the direction perpendicular to the interface. When the energy of the surface mode approaches $\hbar\omega_\mathrm{p}/\sqrt{\epsilon_\mathrm{b}+\epsilon_\mathrm{d}}$, the dispersion starts to depart and bend from the light line, and eventually a maximum $\mathrm{Re}\left\{k_\mathrm{spp}\right\}$ is reached, which sets a lower bound on the SPP wavelength $\lambda_\mathrm{spp} = 2\pi/\mathrm{Re}\left\{k_\mathrm{spp}\right\}$. The momentum mismatch $\mathrm{Re}\left\{k_\mathrm{spp}\right\} > k$ implies that well-confined SPPs cannot directly couple to free radiation. The quantity $\lambda/\lambda_\mathrm{spp}$, with λ the light wavelength in the ambient environment, provides a measure of the mode confinement perpendicular to the interface. Another important quantity known as the propagation length of SPPs is determined by the imaginary part of the wave vector as $L_\mathrm{spp} = 1/2\mathrm{Im}\left\{k_\mathrm{spp}\right\}$, which is defined as the distance where the intensity of the SPP decays to $1/e \approx 1/2.718$ of its initial value. As shown in Fig. 1.2, $1/\mathrm{Im}\left\{k_\mathrm{spp}\right\}$ reaches its minimum while $\mathrm{Re}\left\{k_\mathrm{spp}\right\}$ reaches its maximum, which implies a tradeoff between the propagation length and the mode confinement for SPPs.

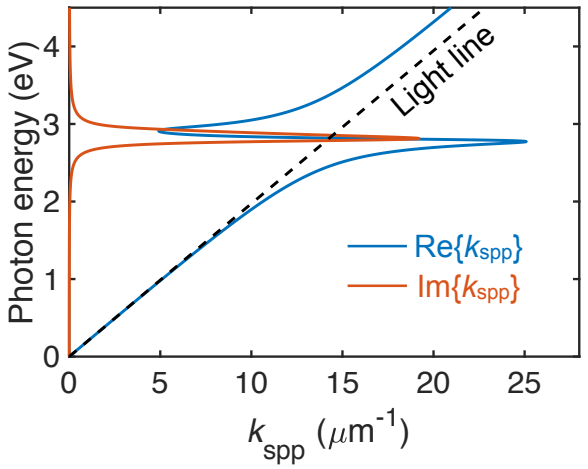

Figure 1.2: **Dispersion relation of surface plasmon polaritons at an air-gold interface.** We show the real and imaginary parts of the SPP wave vector k_{spp}, given by Eq. 1.12, at an air-gold interface. We use Eq. 1.10 to characterize the gold permittivity with parameters (constant $\epsilon_b = 1$) listed in Table 1.1.

1.1.4 Localized surface plasmons

When the geometry of the metal-dielectric structure is transformed from a planar interface to a closed or half-closed form object (*e.g.*, metallic nanoparticles), SPPs supported by those metallic nanoparticles are termed as localized surface plasmons (LSPs). They are again the eigensolutions of Maxwell's equations in the absence of external sources satisfying appropriate boundary conditions defined by the geometry of the nanoparticles.

LSPs can directly interact with free radiation due to the geometric constraint of nanoparticles, providing an effective momentum to assist the coupling. In general, when the particles are small compared with the light wavelength, the optical response of those plasmonic nanoparticles can be characterized in terms of the extinction σ^{ext}, scattering σ^{sca}, and absorption σ^{abs} cross-sections, given as

$$\sigma^{ext} = \frac{4\pi\omega}{\sqrt{\epsilon_h}c}\mathrm{Im}\{\alpha\}, \tag{1.13a}$$

$$\sigma^{sca} = \frac{8\pi\omega^4}{3c^4}|\alpha|^2, \tag{1.13b}$$

$$\sigma^{abs} = \sigma^{ext} - \sigma^{sca}, \tag{1.13c}$$

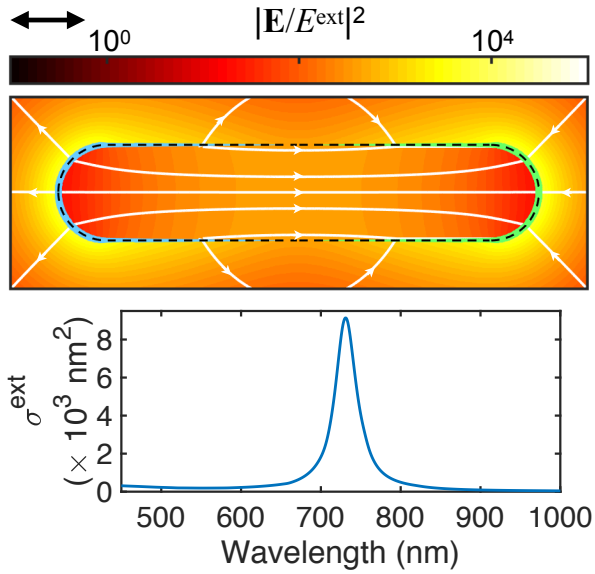

Figure 1.3: **Generic characteristics of localized surface plasmons supported by nanoparticles.** In an illuminated nanoparticle (a nanorod of a 10 nm width, contour indicated by a dashed line, the extinction spectrum σ^{ext} of which is shown in the bottom panel), under the influence of the external optical electric field $\mathbf{E}^{\mathrm{ext}}$, at the resonance wavelength ($\sim$ 731 nm, see bottom panel) conduction electrons move in an oscillatory motion back and forth between the ends of the structure, where induced charges pile up (blue (positive) and green (negative) curves of thickness proportional to the induced surface-charge density) and the total field $\mathbf{E}$ is enhanced (underlying density plot). The orientation of $\mathbf{E}$ (field lines, also parallel to the induced current inside the metal) is nearly perpendicular to the surface in the regions of maximum enhancement. Adapted from Ref. [29].

where α is the polarizability of the nanoparticle, and ϵ_h is the permittivity of the host medium.

As an example, we discuss the first dipolar LSP mode supported by a gold nanorod (with a permittivity given by Eq. 1.10), the extinction cross-section of which is shown in the bottom panel of Fig. 1.3. Under the influence of the oscillatory external electric field $\mathbf{E}^{ext}$ of the incident light, at the resonance wavelength (~ 731 nm, see bottom panel) conduction electrons in an illuminated nanoparticle move in its interior and give rise to charge pileup at the surface, as illustrated in the top panel of Fig. 1.3. This charge accumulation produces in turn an enhanced electric field $\mathbf{E}$ (density plot and field lines in the top panel of Fig. 1.3), which has maximum intensity in the proximity of the particle. The induced part of $\mathbf{E}$ is nearly perpendicular to the surface, and because of the continuity of the normal electric displacement, the magnitude of $\mathbf{E}$ is drastically reduced when moving from outside to inside the particle. Interestingly, the region where the inner field is maximum is roughly situated near the particle center, away from the surface charge pileup. Intuitively, this is expected because the current must be proportional to the field in the metal, which flows in such a way that the surface charge oscillates at the ends of the particle. Like $\mathbf{E}$, the induced current $\mathbf{j}^{ind}$ is divergence-less in the metal ($\nabla \cdot \mathbf{j}^{ind} = 0$), so that, in virtue of the continuity equation, there is no induced charge in the bulk of the particle. However, the current is maximum in the central region, which is also the place where there is more power dissipation ($\propto |\mathbf{E}|^2$) via inelastic coupling of the plasmon to electron-hole pairs in the metal. The dynamics of this type of decay is a complex process,[30] which can be described through a phenomenological relaxation time.

1.1.5 Graphene plasmonics

In the last decade, graphene, a two-dimensional (2D) honeycomb lattice consisting of carbon atoms, has emerged as a very promising material due to its unique mechanical, electric, magnetic, and thermal properties with a plethora of exciting applications pursued by both the academia and industry.[31–33] Those extraordinary properties derive from its peculiar band structure where the conduction and valence bands touch each other at the Dirac points.[33] Close to the Dirac points, the dispersion relations for electrons and holes (with energy E and in-plane wave vector $\mathbf{k}$) become linear and symmetric, given by $E = s\hbar v_F |\mathbf{k}|$, where $s = \pm$ indicates the conduction (+) and the valence (−) bands, respectively, and $v_F \approx c/300$ is the Fermi velocity in the material. The band structure of graphene near the Dirac point is illustrated in Fig. 1.4a.

Another unique property of graphene lies in its strong tunability, thanks again to its peculiar band structure near the Dirac point. Through electrical gating[31] or chemical doping,[34] its Fermi level E_F (relative to the Dirac point) can be largely changed, trans-

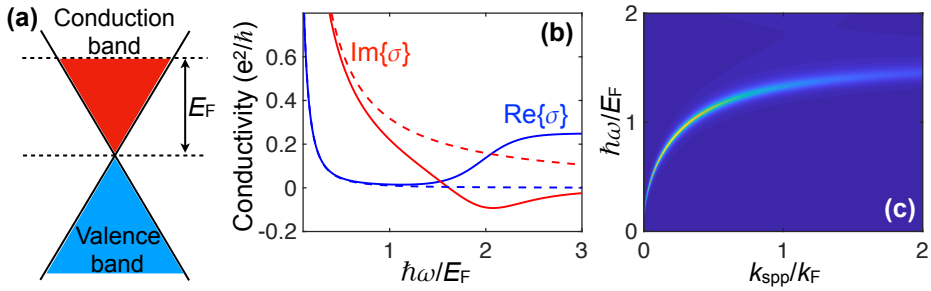

Figure 1.4: **Dispersion relation of surface plasmon polaritons in graphene.** (a) Band structure of graphene near the Dirac point. (b) We show the surface conductivity of graphene calculated under local-RPA by Eq. 1.14 (solid curves, with $E_F = 0.3\,\text{eV}$, $T = 300\,\text{K}$, and $\hbar\tau^{-1} = 10\,\text{meV}$), compared with the Drude model given by Eq. 1.17. (c) We show the loss function $\text{Im}\{r_p\}$, given by Eq. 1.18, for an extended free-standing graphene sheet, the surface conductivity of which is shown as solid curves in panel (b).

forming graphene from a "semiconductor" (with a zero bandgap, $E_F \approx 0$) to a metal ($E_F \neq 0$). The Fermi level E_F and the Fermi wave vector k_F are related to the density of injected charge carriers n by $E_F = \hbar v_F \sqrt{\pi n}$ and $k_F = \sqrt{\pi n}$, respectively.

The optical response of graphene can be characterized by its surface conductivity, given in the local limit (parallel wave vector $\mathbf{k}_\parallel \to 0$) of the random-phase approximation (local-RPA) as[35–38]

$$\sigma(\omega) = \frac{e^2}{\pi\hbar^2}\frac{\mathrm{i}}{(\omega + \mathrm{i}\tau^{-1})}\left\{\mu^D - \int_0^\infty dE\,\frac{f_T(E) - f_T(-E)}{1 - 4E^2/\left[\hbar^2(\omega + \mathrm{i}\tau^{-1})^2\right]}\right\}, \tag{1.14}$$

where $f_T = 1/[1 + e^{(E-\mu)/k_B T}]$ is the Fermi-Dirac distribution, τ is the inelastic decay time, and

$$\mu^D = \mu + 2k_B T \log\left(1 + e^{-\mu/k_B T}\right) \tag{1.15}$$

is a temperature-dependent effective Drude weight that accounts for intraband transitions.[39] The integral term in Eq. 1.14 represents the contribution from interband transitions. Besides the explicit dependence on temperature T, we note that there is an additional dependence through the chemical potential μ, given as[40]

$$\mu = \sqrt{\sqrt{(E_F)^4 + \left(2\log^2 4\right)^2 (k_B T)^4} - \left(2\log^2 4\right)(k_B T)^2}. \tag{1.16}$$

The first term inside the bracket of Eq. 1.14 corresponds to the intraband transitions, whereas the second term corresponds to the interband ones. As displayed by solid curves in Fig. 1.4b, interband transitions arise when $\hbar\omega \approx 2E_{\mathrm{F}}$ (assuming $\mu \approx E_{\mathrm{F}}$ at low temperatures), which leads to a sudden increase in the real part of the surface conductivity $\mathrm{Re}\{\sigma\}$. Under the conditions $\hbar\omega \ll E_{\mathrm{F}}$ and $k_{\mathrm{B}}T \ll E_{\mathrm{F}}$, Eq. 1.14 can be simplified to a Drude-like surface conductivity (shown as dashed curves in Fig. 1.4b) for doped graphene

$$\sigma(\omega) = \frac{e^2}{\pi\hbar^2}\frac{\mathrm{i}E_{\mathrm{F}}}{\omega + \mathrm{i}\tau^{-1}}. \tag{1.17}$$

Therefore, similar to noble metals, doped graphene can support SPPs but at comparably lower frequencies (infrared or terahertz range). They have been experimentally observed by either far-field optical spectroscopy[41–43] or a near-field imaging technique,[44,45] presenting strong dynamic tunability by electrically varying the doping level. The dispersion relation of SPPs in graphene can be obtained again from the pole of the Fresnel reflection coefficient for p-polarized light (similar to Eq. 1.9 for metal-dielectric interfaces), which reads

$$r_{\mathrm{p}} = \frac{\epsilon_2 k_{1\perp} - \epsilon_1 k_{2\perp} + \frac{4\pi\sigma}{\omega}k_{1\perp}k_{2\perp}}{\epsilon_2 k_{1\perp} + \epsilon_1 k_{2\perp} + \frac{4\pi\sigma}{\omega}k_{1\perp}k_{2\perp}}, \tag{1.18}$$

where $\epsilon_{1/2}$ is the permittivity of the material above/below the graphene sheet, and $k_{i\perp}$ is the normal component (perpendicular to the graphene sheet) of the wave vector in the corresponding material. One can obtain the dispersion relation of SPPs in graphene by plotting the loss function, defined as $\mathrm{Im}\left\{\mathrm{r_p}\right\}$, as shown in Fig. 1.4c, where the light line is indistinguishable from the y-axis, indicating a deep sub-wavelength confinement ($k_{\mathrm{spp}} \gg k$, with k the wave vector in the ambient environment) of graphene SPPs.

Another important feature of graphene SPPs is their long lifetime compared with other plasmonic systems (*e.g.*, noble metals or highly-doped semiconductors), leading to a larger value of the quality factor $Q_{\mathrm{p}} = \mathrm{Re}\left\{k_{\mathrm{spp}}\right\}/\mathrm{Im}\left\{k_{\mathrm{spp}}\right\}$ in encapsulated graphene heterostructures, especially at cryogenic temperatures.[46,47]

1.2 Theoretical modeling of localized surface plasmons in the electrostatic limit and beyond

As discussed in the previous section, the lateral size of plasmonic nanoparticles is typically sub-wavelength. Therefore, their optical response is treated in the so-called quasistatic limit. However, in general, it's important to take the retardation effects into account because accurate control over the optical response of metal nanoparticles

and their associated plasmons is currently enabling many promising applications in areas as diverse as biosensing and photocatalysis. In this context, here we present a powerful theoretical framework that can be used to accurately describe the optical response of plasmonic nanoparticles in an analytical manner, including retardation effects.

1.2.1 Optical electric fields in the presence of a particle

We consider a homogeneous three-dimensional (3D) metal particle of local isotropic permittivity $\epsilon_{\rm m}(\omega)$ placed in a uniform host medium of permittivity $\epsilon_{\rm h}(\omega)$ and exposed to an external electric field $\mathbf{E}^{\rm ext}(\mathbf{r},\omega)$. For monochromatic light, the full time-dependent electric field is given by $2{\rm Re}\{\mathbf{E}(\mathbf{r},\omega)e^{-{\rm i}\omega t}\}$, and similarly for other quantities. A current $\mathbf{j}^{\rm ind}(\mathbf{r},\omega)$ is induced in the particle, which permits writing the total electric field as[48]

$$\mathbf{E}(\mathbf{r},\omega)=\mathbf{E}^{\rm ext}(\mathbf{r},\omega)+\frac{\rm i}{\omega\epsilon_{\rm h}}\left(k_{\rm h}^2\mathscr{I}_3+\nabla\otimes\nabla\right)\cdot\int d^3\mathbf{r}'\frac{e^{{\rm i}k_{\rm h}|\mathbf{r}-\mathbf{r}'|}}{|\mathbf{r}-\mathbf{r}'|}\mathbf{j}^{\rm ind}(\mathbf{r}',\omega), \tag{1.19}$$

where $k_{\rm h}=\sqrt{\epsilon_{\rm h}}\,\omega/c$ is the light wave vector in the host medium, and $\mathscr{I}_3$ is the 3×3 identity matrix. Equation E.3 allows us to obtain a self-consistent relation for the electric field by expressing the induced current $\mathbf{j}^{\rm ind}(\mathbf{r},\omega)=f(\mathbf{r})\sigma(\omega)\mathbf{E}(\mathbf{r},\omega)$ in terms of the effective metal conductivity

$$\sigma(\omega)=-{\rm i}\omega\left[\epsilon_{\rm m}(\omega)-\epsilon_{\rm h}(\omega)\right]/4\pi$$

and a filling function $f(\mathbf{r})$ that is 1 for $\mathbf{r}$ inside the metal and takes a vanishing positive value outside of it. Inserting these expressions into Eq. E.3, we obtain

$$\mathbf{E}(\mathbf{r},\omega)=\mathbf{E}^{\rm ext}(\mathbf{r},\omega)+\frac{1}{\mu(\omega)}\left(k_{\rm h}^2\mathscr{I}_3+\nabla\otimes\nabla\right)\cdot\int d^3\mathbf{r}'\,f(\mathbf{r}')\,\frac{e^{{\rm i}k_{\rm h}|\mathbf{r}-\mathbf{r}'|}}{|\mathbf{r}-\mathbf{r}'|}\mathbf{E}(\mathbf{r}',\omega), \tag{1.20}$$

where

$$\mu_{\rm m}(\omega)=\frac{4\pi}{\epsilon_{\rm m}/\epsilon_{\rm h}-1}.$$

Now, multiplying both sides of Eq. 1.20 by $\sqrt{f(\mathbf{r})}$ and defining $\vec{\mathscr{E}}(\mathbf{r},\omega)=\sqrt{f(\mathbf{r})}\,\mathbf{E}(\mathbf{r},\omega)$, we find

$$\vec{\mathscr{E}}(\mathbf{r},\omega)=\vec{\mathscr{E}}^{\rm ext}(\mathbf{r},\omega)+\frac{1}{\mu_{\rm m}(\omega)}\int d^3\mathbf{r}'\mathscr{M}(\mathbf{r},\mathbf{r}')\cdot\vec{\mathscr{E}}(\mathbf{r}',\omega), \tag{1.21}$$

where

$$\mathscr{M}(\mathbf{r},\mathbf{r}')=\sqrt{f(\mathbf{r})f(\mathbf{r}')}\left(k_{\rm h}^2\mathscr{I}_3+\nabla\otimes\nabla\right)\frac{e^{{\rm i}k_{\rm h}|\mathbf{r}-\mathbf{r}'|}}{|\mathbf{r}-\mathbf{r}'|} \tag{1.22}$$

is a linear symmetric operator.

We intend to solve the eigenmodes of Eq. 1.21 through a perturbative manner, and the strength of the perturbation is defined by the power order of the size parameter $s = k_{\mathrm{h}}L/2\pi$ with L the characteristic length of the plasmonic nanoparticle. Detailed theoretical derivation can be found in Appendix A.

1.2.2 Electrostatic limits in two dimensions: plasmon wave functions

As we have seen in the previous section, typically SPPs in graphene are extremely confined (deep sub-wavelength). The optical response of 2D graphene nanostructures is well-described in the electrostatic limit because the characteristic size of the nanostructure is small compared with the incident light wavelength. Following the theoretical framework presented in the previous subsection, we can formulate a self-consistent relation for the electric field similar to Eq. 1.21 in two dimensions and find the eigenmodes for the electric fields. Moreover, due to the two-dimensionality, it is more convenient for us to define another set of eigensolutions, named plasmon wave functions (PWFs), which correspond to the induced charge distributions associated with the eigenmodes for the electric fields. More details about the PWF formalism can be found in Appendix A.

1.3 Microscopic treatment of plasmonic materials

When the characteristic length of the nanostructure is comparable to (or smaller than) the electron mean free path, the classical and macroscopic description of the optical response of plasmonic nanostructures, as presented in Section 1.1, based on solving Maxwell's equations using homogeneous permittivities, is not valid. In this section, we review a microscopic quantum description of the plasmonic response of nanostructures (few nanometers in size; neglect retardation effects) based on the Hartree-Fock approximation and the random-phase approximation (RPA).[49–51] In addition, we provide a formalism to describe the nonlinear plasmonic response using a perturbative approach toward the end of this section.

1.3.1 Hartree-Fock equations

The many-body Hamiltonian for a system composed of N interacting electrons in the presence of nuclei fixed in a spatial configuration (under the rigid lattice approxima-

tion) can be written as[49–51]

$$H_e = \sum_{l}^{N} h(\mathbf{r}_l) + \frac{1}{2}\sum_{l\neq l'}^{N} \frac{e^2}{|\mathbf{r}_l - \mathbf{r}_{l'}|}, \tag{1.23}$$

where

$$h(\mathbf{r}_l) = \frac{\mathbf{p}_l^2}{2m_\mathrm{e}} + V_\mathrm{nucl}(\mathbf{r}_l) \tag{1.24}$$

with $\mathbf{r}_l$, $\mathbf{p}_l$, and m_e denote the electron position, momentum, and mass, respectively. V_nucl represents the potential produced by the nuclei. We intend to describe the ground-state of the many-electron system, given by Eq. 1.23, with a single determinant state (*i.e.*, neglecting configuration interactions) constructed by the one-electron wavefunctions $\psi_j(\mathbf{x})$ with $\mathbf{x}$ indicating both the spatial $\mathbf{r}$ and spin s coordinates (*i.e.*, $\mathbf{x} \equiv (\mathbf{r}, s)$). If we enforce the minimization of the total electron energy, we obtain a set of nonlinear equations, known as the Hartree-Fock equations[49–51]

$$(h + V_\mathrm{HF})\psi_j = \hbar\varepsilon_j\psi_j, \tag{1.25}$$

where $V_\mathrm{HF} = V_\mathrm{H} + V_\mathrm{ex}$ is the Hartree-Fock interaction Hamiltonian, with Hartree and exchange operators defined as

$$V_\mathrm{H}\psi_j(\mathbf{x}) = e^2 \int d\mathbf{x}' v(\mathbf{r}, \mathbf{r}') \sum_{j'}^{N} \left|\psi_{j'}(\mathbf{x}')\right|^2 \psi_j(\mathbf{x}) \tag{1.26}$$

and

$$V_\mathrm{ex}\psi_j(\mathbf{x}) = -e^2 \int d\mathbf{x}' v(\mathbf{r}, \mathbf{r}') \sum_{j'}^{N} \psi_{j'}(\mathbf{x})\psi_{j'}^*(\mathbf{x}')\psi_j(\mathbf{x}'), \tag{1.27}$$

respectively. In the above expressions, $v(\mathbf{r}, \mathbf{r}') = 1/|\mathbf{r} - \mathbf{r}'|$ gives the spatial dependence of the Coulomb interaction between electrons, and the index j indicates the one-electron electronic states of the system, with energies $\hbar\varepsilon_j$.

Now, we consider a periodic arrangement of atoms (forming a crystal lattice), which are represented by orbitals $|l, s\rangle$ located at the atomic sites $\mathbf{r}_l$. The wave functions ψ_j are expressed in terms of these orbitals through the expansion

$$\psi_j(\mathbf{x}_l) \equiv |j\rangle = \sum_{l,s} a_{jls} |l, s\rangle, \tag{1.28}$$

where the coefficients a_{jls} give the amplitude of orbital $|l, s\rangle$ projected in the state $|j\rangle$. The expansion coefficients satisfy the orthogonality condition

$$\sum_{l,s} a_{jls} a_{j'ls}^* = \delta_{jj'},$$

and the closure relation

$$\sum_j a^*_{jls} a_{jl's'} = \delta_{ll',ss'},$$

with δ the Kronecker delta. Using the above expressions, and replacing the continuous variable $\mathbf{r}$ by $\mathbf{r}_l$, after taking the spin degeneracy into account, Eqs. 1.26 and 1.27 can be expressed into a set of matrix elements as

$$[V_{\mathrm{H}}]_{ll'} = 2e^2 \delta_{ll'} \sum_{l''}^{N} v_{ll''} \sum_j^N f_j \left| a_{jl''} \right|^2 \tag{1.29}$$

and

$$[V_{\mathrm{ex}}]_{ll'} = -e^2 v_{ll'} \sum_j^N f_j a_{jl} a^*_{jl'}, \tag{1.30}$$

respectively, where $[A]_{ij}$ indicates the matrix element (i, j) of A, $v_{ll'} = v(\mathbf{r}_l, \mathbf{r}_{l'})$, and f_j is the occupation level of the state j according to the Fermi-Dirac statistics.

The one-electron density matrix can be defined as[52]

$$\rho(\mathbf{x}, \mathbf{x}', t) = \sum_{jj'} \psi_j(\mathbf{x}) \psi_{j'}(\mathbf{x}') \rho_{jj'},$$

keeping in mind that the matrix elements $\rho_{jj'}$ are time-dependent quantities. Using Eq. 1.28, we can also express the density matrix elements in terms of the site orbitals as

$$\rho_{ll'} = \langle l | \rho | l' \rangle = \sum_{jj'} \rho_{jj'} a_{jl} a^*_{j'l'},$$

and find the complementary relation $\rho_{jj'} = \sum_{ll'} \rho_{ll'} a^*_{jl} a_{j'l'}$. The equation of motion for the density matrix is given by[52]

$$\mathrm{i}\hbar \frac{\partial \rho}{\partial t} = [H, \rho] - \frac{\mathrm{i}\hbar}{2\tau} \left(\rho - \rho^{(0)} \right), \tag{1.31}$$

where H is the system Hamiltonian, τ is the phenomenological relaxation time, and $\rho^{(0)}$ is the equilibrium density matrix (*i.e.*, ρ at $t \to -\infty$). In graphene, the optical response is dominated by electrons in the π band, which can be characterized by a tight-binding Hamiltonian with a hopping energy of 2.8 eV between neighboring orbitals.[33,35,53]

1.3.2 Linear response theory

In the linear response regime, it is assumed that the external perturbing potential ϕ^{ext} is small enough so that higher-order terms in the perturbation expansion of the density matrix can be neglected. We use this assumption to describe the first-order (linear) response. Expressed in state representation, the density matrix equation of motion (see Eq. 1.31) is

$$\begin{aligned} \mathrm{i}\hbar\frac{\partial \rho_{jj'}}{\partial t} &= \sum_{j''}\left(H_{jj''}\rho_{j''j'} - \rho_{jj''}H_{j''j'}\right) - \frac{\mathrm{i}\hbar}{2\tau}\left(\rho_{jj'} - \rho^{(0)}_{jj'}\right) \\ &= \hbar\varepsilon_j\rho_{jj'} - \hbar\varepsilon_{j'}\rho_{jj'} - \frac{\mathrm{i}\hbar}{2\tau}\left(\rho_{jj'} - \rho^{(0)}_{jj'}\right) - e\sum_{j''}\left(\phi_{jj''}\rho_{j''j'} - \rho_{jj''}\phi_{j''j'}\right), \end{aligned} \tag{1.32}$$

where we have used $H = H_0 - e\phi$, with H_0 the unperturbed Hamiltonian ($H_0\,|j\rangle = \hbar\varepsilon_j\,|j\rangle$) and $\phi = \phi^{\text{ind}} + \phi^{\text{ext}}$ the total potential acting on the system, which is the sum of the potential from the induced charge distribution ϕ^{ind} and the external potential ϕ^{ext} due to the applied electric field.

To first order, Eq. 1.32 then becomes

$$\mathrm{i}\hbar\frac{\partial \rho^{(1)}_{jj'}}{\partial t} = \hbar\left(\varepsilon_j - \varepsilon_{j'}\right)\rho^{(1)}_{jj'} - \frac{\mathrm{i}\hbar}{2\tau}\rho^{(1)}_{jj'} - e\sum_{j''}\left(\phi^{(1)}_{jj''}\rho^{(0)}_{j''j'} - \rho^{(0)}_{jj''}\phi^{(1)}_{j''j'}\right). \tag{1.33}$$

Note that the total potential is also taken to first order due to its dependence on the density matrix through ϕ^{ind}. The equilibrium density matrix is given by $\rho^{(0)}_{jj'} = f_j\delta_{jj'}$, and thus the equation of motion becomes

$$\mathrm{i}\hbar\frac{\partial \rho^{(1)}_{jj'}}{\partial t} = \hbar\left(\varepsilon_j - \varepsilon_{j'}\right)\rho^{(1)}_{jj'} - \frac{\mathrm{i}\hbar}{2\tau}\rho^{(1)}_{jj'} - e\left(f_{j'} - f_j\right)\phi^{(1)}_{jj'}. \tag{1.34}$$

We assume the time dependence of the external potential to be harmonic, *i.e.*, $\phi^{\text{ext}} \propto \mathrm{e}^{-\mathrm{i}\omega t}$. This allows us to write

$$\rho^{(1)}_{jj'} = -\frac{e}{\hbar}\left(f_{j'} - f_j\right)\frac{\phi^{(1)}_{jj'}}{\omega + \mathrm{i}/2\tau - \left(\varepsilon_j - \varepsilon_{j'}\right)}. \tag{1.35}$$

To obtain the first-order induced charge density $\rho^{\text{ind}} = -2e\rho^{(1)}_{ll}$, after converting the density matrix to the site representation by using $\phi_{jj'} = \sum_l a^*_{jl}a_{j'l}\phi_l$, we find

$$\begin{aligned} \rho^{\text{ind}} &= \sum_{l'}\chi^0_{ll'}\phi^{\text{ext}}_{l'} + \sum_{l'}\chi^0_{ll'}\phi^{\text{ind}}_{l'} \\ &= \sum_{l'}\chi^0_{ll'}\phi^{\text{ext}}_{l'} - 2e\sum_{l'l''}\chi^0_{ll'}v_{l'l''}\rho^{(1)}_{l''l''}, \end{aligned}$$

where

$$\chi^0_{ll'} = \frac{2e^2}{\hbar}\sum_{jj'}\left(f_{j'}-f_j\right)\frac{a_{jl}a^*_{j'l}a^*_{jl'}a_{j'l'}}{\omega+\mathrm{i}/2\tau-\left(\varepsilon_j-\varepsilon_{j'}\right)} \tag{1.36}$$

is the non-interacting susceptibility and $\phi^{\mathrm{ind}}_l = -2e\sum_{l'} v_{ll'}\rho^{(1)}_{l'l'}$. In matrix form, the above expression for the induced charge density becomes

$$\rho^{\mathrm{ind}} = \chi^0\phi = \chi^0\phi^{\mathrm{ext}} + \chi^0 v\rho^{\mathrm{ind}}.$$

Since $v\rho^{\mathrm{ind}} = \phi - \phi^{\mathrm{ext}}$, we find

$$\phi = \left(1-v\chi^0\right)^{-1}\phi^{\mathrm{ext}}.$$

The induced charge density is then obtained as

$$\rho^{\mathrm{ind}} = \chi^0\left(1-v\chi^0\right)^{-1}\phi^{\mathrm{ext}} = \chi\phi^{\mathrm{ext}}, \tag{1.37}$$

where we obtain the susceptibility $\chi = \chi^0\left(1-v\chi^0\right)^{-1}$ under the so-called random-phase approximation (RPA). We can then calculate the polarizability as

$$\alpha = \frac{1}{E_0}\sum_l x_l\rho_l, \tag{1.38}$$

where E_0 is the amplitude of the incident field, and x_l are the projections of the atomic sites along the direction of the incident field.

1.3.3 Nonlinear response

Since the plasmonic resonances produce strong electromagnetic field enhancement, which assists the originally weak nonlinear processes to be also significantly enhanced, it is natural to explore the nonlinear optical response (*e.g.*, high harmonic generation) of plasmonic nanosystems.

Following a previously developed formalism,[23] which we summarize here for completeness, the density matrix can be expanded in harmonics of the incident continuous wave (CW) radiation as

$$\rho = \sum_{n,s}\rho^{ns}\mathrm{e}^{-\mathrm{i}s\omega t},$$

where n is the order of perturbation ($n = 1,2,3,...$) and $|s| \leq n$ is the harmonic order. Using the above expression, the density matrix equation of motion Eq. 1.32

becomes

$$\hbar\sum_{n,s}(s\omega+\mathrm{i}/2\tau)\,\rho^{ns}_{jj'}e^{-\mathrm{i}s\omega t}=\hbar\left(\varepsilon_j-\varepsilon_{j'}\right)\sum_{n,s}\rho^{ns}_{jj'}e^{-\mathrm{i}s\omega t} \\ -e\sum_{j''}\sum_{n,s}\sum_{n',s'}\left(\phi^{n's'}_{jj''}\rho^{ns}_{j''j'}-\rho^{ns}_{jj''}\phi^{n's'}_{j''j'}\right)e^{-\mathrm{i}s\omega t}e^{-\mathrm{i}s'\omega t}, \tag{1.39}$$

where $\phi^{ns}_{jj'}=\sum_l a^*_{jl}a_{j'l}\phi^{ns}_l$ and

$$\phi^{ns}_l=\phi^{\mathrm{ext}}_l\delta_{n,1}\left(\delta_{s,-1}+\delta_{s,1}\right)-2e\sum_{l'}v_{ll'}\rho^{ns}_{l'l'}, \tag{1.40}$$

i.e., the external field only contains components at the fundamental frequency. After identifying the terms with the same $e^{-\mathrm{i}s\omega t}$ dependence on both sides of Eq. 1.39, we can write the equation for $\rho^{ns}_{jj'}$ as a sum of the self-consistent part and the term that depends on lower expansion orders, $\eta^{ns}_{jj'}$, as

$$\rho^{ns}_{jj'}=-\frac{e}{\hbar}\sum_{ll'}\frac{a^*_{jl}a_{j'l'}\left(\phi^{ns}_l-\phi^{ns}_{l'}\right)}{s\omega+\mathrm{i}/2\tau-\left(\varepsilon_j-\varepsilon_{j'}\right)}\rho^{(0)}_{ll'}+\eta^{ns}_{jj'}, \tag{1.41}$$

where

$$\eta^{ns}_{jj'}=-\frac{e}{\hbar}\sum_{n'=1}^{n-1}\sum_{s'=-n'}^{n'}\sum_{ll'}\frac{a^*_{jl}a_{j'l'}\left(\phi^{n's'}_l-\phi^{n's'}_{l'}\right)}{s\omega+\mathrm{i}/2\tau-\left(\varepsilon_j-\varepsilon_{j'}\right)}\rho^{n-n's-s'}_{ll'}. \tag{1.42}$$

To solve the above expression, we use the same approach implemented for the linear response (see above). We begin by using the identity $\rho^{(0)}_{ll'}=\sum_{jj'}a_{jl}a^*_{j'l'}\rho^{(0)}_{jj'}=\sum_j a_{jl}a^*_{jl'}f_j$ to move to the site representation

$$\rho^{ns}_{ll'}=-\frac{e}{\hbar}\sum_{jj'}\sum_{l''}\left(f_{j'}-f_j\right)\frac{a_{jl}a^*_{j'l'}a^*_{jl''}a_{j'l''}}{s\omega+\mathrm{i}/2\tau-\left(\varepsilon_j-\varepsilon_{j'}\right)}\phi^{ns}_{l''}+\sum_{jj'}a_{jl}a^*_{j'l'}\eta^{ns}_{jj'}, \tag{1.43}$$

the diagonal elements of which are given by

$$\rho^{ns}_{ll}=-\frac{1}{2e}\sum_{l'}\chi^0_{ll'}(s\omega)\phi^{ns}_{l'}+\sum_{jj'}a_{jl}a^*_{j'l}\eta^{ns}_{jj'}, \tag{1.44}$$

where $\chi^0_{ll'}$ is the non-interacting RPA susceptibility given in Eq. 1.36. With the total potential given in Eq. 1.40, together with the definition of the induced charge density $\rho^{ns}_{\mathrm{ind}}=-2e\rho^{ns}_{ll}$, we find ϕ^{ns} expressed in matrix form as

$$\phi^{ns}=\left[1-v\chi^0(s\omega)\right]^{-1}\beta^{ns}, \tag{1.45}$$

where

$$\beta_l^{ns} = \phi_l^{\text{ext}} \delta_{n,1} \left(\delta_{s,-1} + \delta_{s,1} \right) - 2e \sum_{l'} v_{ll'} \sum_{jj'} a_{jl'} a^*_{j'l'} \eta^{ns}_{jj'}. \tag{1.46}$$

With the external potential given above, we compute the diagonal elements of the density matrix (in the site representation) using Eq. 1.44, and we can also compute the full density matrix using Eq. 1.41. Finally, the polarizability of order s can be computed from

$$\alpha^{(s)} = -\frac{2e}{E_0^s} \sum_l r_l \rho^{ss}_{ll}, \tag{1.47}$$

where E_0 is the amplitude of the incident field. Especially, for the linear response ($s = 1$), $\alpha^{(s)}$ can be also obtained from Eq. 1.38.

1.4 Fundamentals of nanoscale heat transport

Active control and manipulation of energy dissipation and transport in nanoscale systems are crucial for application to areas ranging from the design of nanoelectromechanical systems[54] to photothermal cancer therapy,[55] nanocatalysis,[56] information storage,[57] and drug delivery.[58] Besides, understanding the interaction between electrons and phonons in different systems is of great importance from a fundamental research viewpoint. In this section, we present several basic concepts of nanoscale heat transport that becomes useful in subsequent chapters.

1.4.1 Nanoscale thermal sources

The excitation of plasmons enhances light absorption in plasmonic nanoparticles, and subsequently the absorbed light energy is converted into heat energy. In this way, this plasmon-assisted photothermal process is emerging as a powerful tool to engineer nanoscale thermally activated applications. The generated heat power density can be expressed as[59]

$$p^{\text{abs}}(\mathbf{r}) = \frac{\omega}{2\pi} \text{Im}\left\{\epsilon(\mathbf{r}, \omega)\right\} |\mathbf{E}(\mathbf{r})|^2, \tag{1.48}$$

where $\epsilon(\mathbf{r}, \omega)$ is the position- and light-frequency-dependent permittivity of the composite material, while $\mathbf{E}(\mathbf{r})$ is the amplitude of the optical electric field (*i.e.*, $\mathbf{E}(\mathbf{r})e^{-\text{i}\omega t} + \mathbf{E}^*(\mathbf{r})e^{\text{i}\omega t}$ gives the full time-dependence of the electric field); Eq. 1.48 reveals that only regions of the material with nonvanishing $\text{Im}\{\epsilon\}$ can directly couple optical energy into heat, typically dominated by electronic excitations. Note that the generated

heat power P^{abs} can be calculated as

$$P^{\text{abs}}(\omega) = \int d\mathbf{r} p^{\text{abs}}(\mathbf{r}) = \sigma_{\text{abs}} I_0, \tag{1.49}$$

where σ_{abs} is the absorption cross-section of the plasmonic nanoparticle and I_0 is the incident light intensity.

Another important aspect to mention is that by manipulating either $\text{Im}\{\epsilon(\mathbf{r},\omega)\}$ through choosing the proper composite material or $\mathbf{E}(\mathbf{r})$ through designing the configuration of the nanostructure, a high degree of nanoscale control over the thermal source can be accomplished.

1.4.2 Two-temperature model

To a good approximation, immediately after the external optical pump is applied, the optically excited electrons are in a non-thermal (non-equilibrium) state at the very initial stage. After a characteristic time of 10s-100s femtoseconds, they reach a thermalized state at an elevated temperature T_{e} due largely to electron-electron interactions.[60–63] Here, we typically have an elevated electron temperature T_{e} much higher than the lattice one T_{l}, and a two-temperature model describing the space-time dynamics between T_{e} and T_{l} can be formulated as[64]

$$C_{\text{e}} \frac{dT_{\text{e}}}{dt} = p^{\text{abs}} + \nabla \cdot (\kappa_{\text{e}} \nabla T_{\text{e}}) - H(T_{\text{e}}, T_{\text{l}}), \tag{1.50}$$

$$C_{\text{l}} \frac{dT_{\text{l}}}{dt} = \nabla \cdot (\kappa_{\text{l}} \nabla T_{\text{l}}) + H(T_{\text{e}}, T_{\text{l}}) - B(T_{\text{l}}, T_0), \tag{1.51}$$

where T_0 is the ambient temperature, C_{e} and C_{l} are the electron and lattice heat capacities, κ_{e} and κ_{l} are the electron and lattice thermal conductivities, $H(T_{\text{e}}, T_{\text{l}})$ describes electron-phonon coupling, and $B(T_{\text{l}}, T_0)$ accounts for the thermal out-coupling to the environment. Note that the dependence of $H(T_{\text{e}}, T_{\text{l}})$ and $B(T_{\text{l}}, T_0)$ on the temperatures is nontrivial, defined by the details of the system under study. Under CW illumination, the temperatures reach a steady-state regime, in which the left-hand sides of Eqs. 1.50 and 1.51 vanish, leading to

$$-\nabla \cdot (\kappa_{\text{e}} \nabla T_{\text{e}}) = p^{\text{abs}} - H(T_{\text{e}}, T_{\text{l}}), \tag{1.52}$$

$$-\nabla \cdot (\kappa_{\text{l}} \nabla T_{\text{l}}) = H(T_{\text{e}}, T_{\text{l}}) - B(T_{\text{l}}, T_0). \tag{1.53}$$

Specifically, in graphene, due to its two-dimensional nature, its electronic heat capacity is rather small, which leads to a very short thermal response time. The heat capacity is needed to relate the electronic thermal energy Q to the electronic temperature T_{e}.

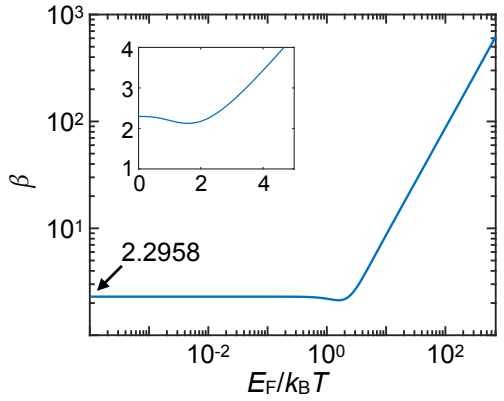

Figure 1.5: **Graphene electronic heat.** We show the dependence of the thermal coefficient β on $E_F/k_B T_e$, as calculated from Eq. 1.55. This parameter permits obtaining the electronic heat per unit of graphene area as $\beta\,(k_B T_e)^3/(\hbar v_F)^2$ (Eq. 1.54). The inset shows β in a linear scale. Adapted from Ref. [40].

The surface density of electronic thermal energy in the material can be expressed as[40]

$$\frac{Q}{A} = \beta\,\frac{(k_B T_e)^3}{(\hbar v_F)^2}, \tag{1.54}$$

where the thermal coefficient

$$\beta = \frac{2}{\pi}\left[\int_0^\infty x^2 dx \left(\frac{1}{e^{x+\mu/k_B T_e}+1} + \frac{1}{e^{x-\mu/k_B T_e}+1}\right) - \frac{1}{3}\left(\frac{E_F}{k_B T_e}\right)^3\right] \tag{1.55}$$

explicitly depends on $\mu/k_B T_e$, which is in turn a function of $E_F/k_B T_e$ (see Eq. 1.16), so we find that β is only a function of $E_F/k_B T_e$. Numerical evaluation of Eq. 1.55 yields the results shown in Fig. 1.5. For $E_F \ll k_B T_e$, we have $\beta \approx 2.2958$.

1.4.3 Near-field radiative heat transfer

In the nanoscale, besides conventional heat conduction, non-contact radiative heat transfer can play an important role. When the separation distance between two objects is smaller than a characteristic length $\sim 2\pi\hbar c/k_B T$ (*i.e.*, the thermal wavelength at temperature T), radiative heat transfer is dominated by additional channels mediated by evanescent waves.[65–67] These can produce rates exceeding the black-body limit by several orders of magnitude, enhanced by the near-field coupling of resonances

supported by the nanostructures, thus emerging as a potentially relevant transfer mechanism in solid-state devices. In the following, we are going to present the theory of radiative heat transfer.

Here, we consider two structures labeled by the index $\ell = 1, 2$, each of them assumed to be in internal thermal equilibrium at a temperature T_ℓ. Radiative heat transfer can take place if $T_1 \neq T_2$, mediated by electromagnetic interaction at characteristic frequencies $\sim k_B T_\ell/\hbar$.[68] We further assume the corresponding light wavelengths $\sim 2\pi\hbar c/k_B T_\ell$ to be much smaller than the size of the structures. The response of the latter can be then described in the quasistatic limit through their susceptibilities $\chi_\ell(\mathbf{r},\mathbf{r}',\omega)$, which are defined as the induced charge density distribution at $\mathbf{r}$ produced by a unit point charge oscillating with frequency ω at $\mathbf{r}'$. The charge density induced in the ℓ structure by a monochromatic potential $\phi(\mathbf{r})\exp(-\mathrm{i}\omega t) + \text{c.c.}$ is then given by $\int d^3\mathbf{r}'\chi_\ell(\mathbf{r},\mathbf{r}',\omega)\phi(\mathbf{r}')\exp(-\mathrm{i}\omega t) + \text{c.c.}$

We express the net power received by structure 2 as the work $P_{2\leftarrow 1}$ done on 2 by charges fluctuating in 1 minus the work $P_{1\leftarrow 2}$ done on 1 by charges fluctuating in 2. It is enough to calculate the latter in detail because the former is simply obtained by interchanging the subindices 1 and 2 in the resulting expression. We start from $P_{1\leftarrow 2} = -\left\langle \int d^3\mathbf{r}\,\mathbf{j}_1(\mathbf{r},t)\cdot\nabla\phi_2(\mathbf{r},t)\right\rangle$, which is the work exerted by the electric field $-\nabla\phi_2(\mathbf{r},t)$ produced by fluctuations in 2, acting on the current $\mathbf{j}_1(\mathbf{r},t)$ of 1. Here, $\langle\ldots\rangle$ denotes the average over thermal fluctuations. After some lengthy but straightforward algebra, we find

$$\begin{aligned} P_{1\leftarrow 2} &= \mathrm{i}\iint \frac{d\omega d\omega'}{(2\pi)^2}\,\omega\, e^{-\mathrm{i}(\omega+\omega')t}\left\langle \int d^3\mathbf{r}d^3\mathbf{r}'\,\rho_1(\mathbf{r},\omega)v(\mathbf{r},\mathbf{r}')\rho_2(\mathbf{r}',\omega')\right\rangle \\ &= \mathrm{i}\iint \frac{d\omega d\omega'}{(2\pi)^2}\,\omega\, e^{-\mathrm{i}(\omega+\omega')t}\left\langle \rho_1(\omega)^{\mathrm{T}}\cdot v\cdot\rho_2(\omega')\right\rangle. \end{aligned} \tag{1.56}$$

The last line of Eq. 1.56 implicitly defines a matrix notation in which $\mathbf{r}$ and $\mathbf{r}'$ are used as matrix indices, while the dot indicates matrix multiplication.

The self-consistent charges ρ_ℓ produced by the fluctuating charge ρ_2^{fl} are now obtained from the relations

$$\rho_1 = \chi_1\cdot v\cdot\rho_2, \qquad \rho_2 = \chi_2\cdot v\cdot\rho_1 + \rho_2^{\mathrm{fl}},$$

where we work in the frequency domain and use the matrix notation introduced above. Inserting the solution of these equations into Eq. 1.56, we find

$$\begin{aligned} P_{1\leftarrow 2} = \mathrm{i}\iint \frac{d\omega d\omega'}{(2\pi)^2}\,\omega\, e^{-\mathrm{i}(\omega+\omega')t} \\ \times \int d^3\mathbf{r}\int d^3\mathbf{r}'\left\langle\left[\chi_1(\omega)\cdot v\cdot\Delta(\omega)\cdot\rho_2^{\mathrm{fl}}(\omega)\right]\Big|_{\mathbf{r}} v(\mathbf{r},\mathbf{r}')\left[\Delta(\omega')\cdot\rho_2^{\mathrm{fl}}(\omega')\right]\Big|_{\mathbf{r}'}\right\rangle, \end{aligned} \tag{1.57}$$

where

$$\Delta = (\mathscr{I} - \chi_2 \cdot v \cdot \chi_1 \cdot v)^{-1}, \tag{1.58}$$

whereas $\mathscr{I}$ is the unit matrix (*i.e.*, $\delta(\mathbf{r}—\mathbf{r}')$). Now, the average over thermal fluctuations can be carried out using the fluctuation-dissipation theorem[69–72]

$$\left\langle \rho_\ell^{\text{fl}}(\mathbf{r},\omega)\rho_{\ell'}^{\text{fl}}(\mathbf{r}',\omega')\right\rangle = -4\pi\hbar\delta_{\ell\ell'}\,\delta(\omega+\omega')\,[n_\ell(\omega)+1/2]\,\text{Im}\left\{\chi_\ell(\mathbf{r},\mathbf{r}',\omega)\right\}, \tag{1.59}$$

where $n_\ell(\omega) = [\exp(\hbar\omega/k_\text{B}T_\ell)-1]^{-1}$ is the Bose-Einstein distribution at temperature T_ℓ (*i.e.*, for structure ℓ).

A detailed self-contained derivation of Eq. 1.59 is offered in Appendix B. We find Eq. 1.57 to reduce to

$$P_{1\leftarrow 2} = \frac{2\hbar}{\pi}\int_0^\infty \omega\, d\omega\, (n_2+1/2)\,\text{Tr}\left[\Delta^\dagger\cdot v\cdot \text{Im}\{\chi_1\}\cdot v\cdot\Delta\cdot\text{Im}\{\chi_2\}\right], \tag{1.60}$$

where Tr[...] stands for the trace, † refers to the conjugate transpose. Finally, the net power received by 2 is obtained from

$$\begin{aligned} P_2 &= P_{2\leftarrow 1} - P_{1\leftarrow 2} \\ &= \frac{2\hbar}{\pi}\int_0^\infty \omega\, d\omega\, (n_1-n_2)\,\text{Tr}\left[\Delta^\dagger\cdot v\cdot \text{Im}\{\chi_1\}\cdot v\cdot\Delta\cdot\text{Im}\{\chi_2\}\right], \end{aligned} \tag{1.61}$$

where the matrix Δ (see Eq. 1.58) accounts for multiple scattering between the two structures. From the invariance of the expression in the square brackets of Eq. 1.61 under exchange of the subindices 1 and 2, we confirm the expected result $P_1 = -P_2$.

Finally, for structures separated by a large distance d compared to their sizes, in virtue of induced-charge neutrality (*i.e.*, $\int d^3\mathbf{r}\,\chi_\ell(\mathbf{r},\mathbf{r}',\omega) = 0$ for each ℓ), the leading contribution to v is the dipole-dipole interaction. Specifically, for parallel disks placed in vacuum, neglecting multiple scattering (*i.e.*, taking $\Delta = \mathscr{I}$), we find from Eq. 1.61

$$P_2 \approx \frac{4\hbar}{\pi d^6}\int_0^\infty \omega\, d\omega\, (n_1-n_2)\,\text{Im}\{\alpha_1\}\text{Im}\,\{\alpha_2\}, \tag{1.62}$$

where

$$\alpha_\ell(\omega) = -\int x\, d^3\mathbf{r}\int x'\, d^3\mathbf{r}'\chi_\ell(\mathbf{r},\mathbf{r}',\omega) \tag{1.63}$$

is the polarizability of disk ℓ along a direction x parallel to it.

2

Advanced analytical modeling of localized surface plasmons

2.1 Introduction

Metal nanoparticles exhibit extraordinary optical properties inherited from the ability of their conduction electrons to sustain collective oscillations known as plasmons, which are key ingredients in those applications. Most notably, (i) plasmons interact strongly with light; (ii) they are robust against imperfections, inhomogeneities, environmental noise; (iii) their frequency and spatial extension are sensitive to the dielectric environment; (iv) the optical electric field can be largely amplified near a nanoparticle when irradiated by light tuned to one of its plasmon resonances; and (v) the optical enhancement can be confined down to a nanometer-sized region, much smaller than the incident light wavelength.

However, despite being the workhorse of plasmonics research, noble metals unfortunately present relatively large inelastic losses, thus limiting plasmon lifetimes in metallic nanostructures[28] and leading to a severe reduction in the optical confinement. Recently, highly-doped graphene has emerged as an outstanding plasmonic material[35,36,41–45,73–79] that simultaneously provides strong field confinement with relatively lower loss.[46] More importantly, plasmons in graphene are sustained by a small number of charge carriers compared to those of traditional noble metals, a property that makes them amenable to display new phenomena, including an unprecedented electro-optical response. Indeed, active tunability of the plasmon resonance frequency has been achieved via electrical gating.[41–45,74,75,77,78]

These extraordinary properties are of paramount importance for a wide range of applications, such as optical sensing and modulation,[5–8,80,81] the enhancement of nonlinear optical processes,[21,22,82–84] photocatalysis,[15–20] and photothermal therapies.[24,25] In these applications, the precise spectral positioning of plasmon resonances is needed to achieve optimal performance. It is commonly achieved by fabricating noble metal nanostructures with specific sizes and morphologies.

In this context, experiments based upon colloid synthesis and nanofabricated structures are assisted by less efficient numerical electromagnetic modeling, which supplies predictive simulations, but not the kind of physical intuition needed for exploration of new ideas, such as one finds when simple mathematical expressions can describe a problem. Therefore, an efficient, ideally analytical, theoretical model is highly demanded to describe the plasmonic response of nanoparticles.

In this chapter, we first present and extend a simple analytical simulation method that allows us to accurately describe the optical response of three-dimensional metal nanoparticles, including retardation effects, without the requirement of large computational resources. More precisely, we show that plasmonic extinction spectra are described through a small set of real numbers for each nanoparticle shape, which we tabulate for a wide selection of common morphologies. Remarkably, these numbers

are independent of size, composition, and environment. We further present a compilation of nanoplasmonic experimental data that are excellently described by the simple mathematical expressions here introduced. Toward the end of this chapter, we further adapt our theoretical model to the two-dimensional regime to study the optical response of graphene structures with arbitrary morphologies based on the concept of plasmon wave functions (PWFs).

2.2 Analytical model

Since a comprehensive description of the theoretical framework to model localized surface plasmons (LSPs) is provided in Section 1.2 and Appendix A, in the current section a brief discussion is given to summarize the main results presented there.

2.2.1 Electrostatic limit

In what follows, we consider illumination with monochromatic light of frequency ω, so that the time dependence of the electric field is given by $\mathbf{E}(\mathbf{r},t) = \mathbf{E}(\mathbf{r},\omega)e^{-\mathrm{i}\omega t} + \mathbf{E}^{*}(\mathbf{r},\omega)e^{\mathrm{i}\omega t}$. Additionally, we focus on homogeneous 3D metallic particles with a characteristic length of L, with the metal described through its frequency-dependent permittivity $\epsilon_{\mathrm{m}}(\omega)$. This is the so-called local approximation (*i.e.*, the assumption that the dielectric displacement $\epsilon_{\mathrm{m}}(\omega)\mathbf{E}(\mathbf{r},\omega)$ depends exclusively on the electric field at the same position $\mathbf{r}$), which only breaks down for very small particles[85] (typically $< 10\,\mathrm{nm}$ for noble metals) and also in the presence of either sharp tips or narrow gaps between metals ($< 1\,\mathrm{nm}$).[86,87]

For small particles compared with the light wavelength, retardation effects are negligible and the optical response can be simulated by solving Poisson's equation $\nabla \cdot \epsilon(\mathbf{r},\omega)\mathbf{E}(\mathbf{r},\omega) = 0$, where $\epsilon(\mathbf{r},\omega) = \epsilon_{\mathrm{m}}(\omega)f(\mathbf{r}) + (1-f(\mathbf{r}))\epsilon(\omega)$, ϵ_{h} is the permittivity of the host dielectric, and $f(\mathbf{r})$ is a filling function that takes a value of 1 inside the particle and 0 elsewhere. Modal expansions have been used for a long time to obtain semi-analytical formulations of this electrostatic limit.[29,38,88–92] They essentially rely on the existence of a complete, orthogonal set of real eigenmodes $\mathbf{E}_j(\mathbf{r})$ and eigenvalues ϵ_j labeled by j and satisfying

$$\nabla \cdot \big[\epsilon_j f(\mathbf{r}) + 1 - f(\mathbf{r})\big]\mathbf{E}_j(\mathbf{r}) = 0.$$

In other words, $\mathbf{E}_j$ is the self-standing electrostatic field for a particle of the same geometry placed in vacuum and filled with a medium of permittivity ϵ_j. Remarkably, these modes are independent of material composition.

The particle polarizability along a symmetry direction also admits an expansion in terms of contributions from different eigenmodes as

$$\alpha(\omega) = \frac{\epsilon_\mathrm{h}}{4\pi} \sum_j V_j \left(\frac{1}{\epsilon_\mathrm{m}/\epsilon_\mathrm{h} - 1} - \frac{1}{\epsilon_j - 1} \right)^{-1}, \tag{2.1}$$

where

$$V_j = (1/L^3) \left| \int d^3\mathbf{r}\, f(\mathbf{r})\, \mathbf{E}_j(\mathbf{r}) \right|^2 \tag{2.2}$$

are mode volumes. For example, for each of the symmery axes $l = x, y, z$ of an ellipsoid, there is only one electrostatic dipolar mode, and in turn, also only one term ($j = 1$) in Eq. 2.1, with $V_1 = V$ and $\epsilon_1 = 1 - 1/L_l$, where $L_l = (a_x a_y a_z/2) \int_0^\infty ds (s + a_l^2)^{-1} [(s + a_x^2)(s + a_y^2)(s + a_z^2)]^{-1/2}$ is the corresponding depolarization factor[93] and $a_{x,y,z}$ are the half-axis lengths.

2.2.2 Retardation corrections

We now extend the electrostatic limit to include effects derived from the finite size of the particle relative to the free-space light wavelength λ. In particular, we use the size factor $s = \sqrt{\epsilon_\mathrm{h}} L/\lambda$ as a convenient perturbation parameter that already incorporates the reduction of the wavelength in the host medium relative to free space due to the refractive index $\sqrt{\epsilon_\mathrm{h}}$. The polarizability of Eq. 2.1 can be rigorously corrected as

$$\alpha(\omega) = \frac{\epsilon_\mathrm{h}}{4\pi} \sum_j V_j B_j(s) \left(\frac{1}{\epsilon_\mathrm{m}/\epsilon_\mathrm{h} - 1} - \frac{1}{\epsilon_j - 1} - A_j(s) \right)^{-1}, \tag{2.3}$$

where $A_j(s)$ and $B_j(s)$ are s-dependent functions. Here, we are interested in practice in situations for which s is not too large (see results below), so it is natural to expand these functions in power series of s. We note that the plasmon resonances are shifted and broadened due to the presence of nonzero real and imaginary parts in A_j, respectively, for which we derive the expansion

$$A_j = a_{j2} s^2 + \frac{4\pi^2 \mathrm{i} V_j}{3L^3} s^3 + a_{j4} s^4 + \ldots, \tag{2.4}$$

where

$$\begin{aligned} a_{jn} = \frac{(2\pi\mathrm{i})^n}{4\pi n(n-2)! L^{n+3}} \int d^3\mathbf{r} f(\mathbf{r}) \int d^3\mathbf{r}' f(\mathbf{r}') \\ \times \Big\{ (n-3) |\mathbf{r} - \mathbf{r}'|^{n-5} \big[(\mathbf{r} - \mathbf{r}') \cdot \mathbf{E}_j(\mathbf{r}) \big] \big[(\mathbf{r} - \mathbf{r}') \cdot \mathbf{E}_j(\mathbf{r}') \big] \\ + (1-n) |\mathbf{r} - \mathbf{r}'|^{n-3} \mathbf{E}_j(\mathbf{r}) \cdot \mathbf{E}_j(\mathbf{r}') \Big\}. \end{aligned} \tag{2.5}$$

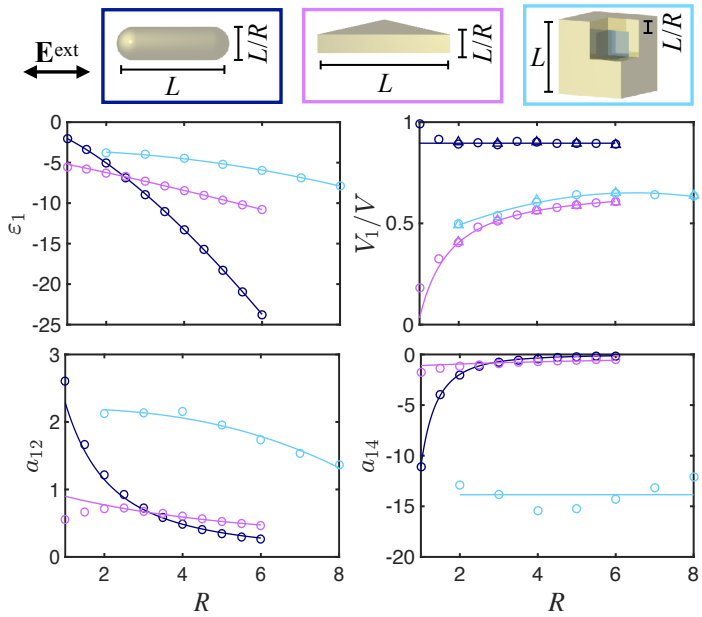

Figure 2.1: **Analytical model parameters for selected particle morphologies.** We show the resonant permittivity ϵ_1, the mode volume V_1 normalized to the particle volume V, and the two retardation parameters a_{12} and a_{14} for the lowest-order dipole plasmon of rods, triangles, and cubic cages as a function of aspect ratio R. We define R and the polarization direction (double arrows) in the upper insets. Symbols for ϵ_1 are obtained by fitting the numerically calculated absorption spectra in the electrostatic limit. The rest of the symbols for other parameters are computed by integrating the electrostatic mode fields as shown in Eqs. 2.2 and 2.5, except the triangular symbols for V_1, which are extracted from the peaks in the noted spectra for comparison. Solid curves represent analytical interpolations (see Table 2.1).

shape	ϵ_1	V_1/V	a_{12}	a_{14}
rod	$-1.73R^{1.45}$ -0.296	0.896	$6.92/(1-\epsilon_1)$	$6.69/(\epsilon_1-1)$
triangle	$-0.87R^{1.12}$ -4.33	$-0.645R^{-1.24}$ $+0.678$	$5.57/(1-\epsilon_1)$	$6.83/(\epsilon_1-1)$
cage	$-0.0678R^{2.02}$ -3.42	$-0.008R^2$ $+0.103R$ $+0.316$	$-0.00405R^{2.59}$ $+2.21$	-13.9

Table 2.1: Fitting functions for $\epsilon_1, V_1/V, a_{12}$, and a_{14} corresponding to selected particle morphologies as a function of aspect ratio R (as defined in Fig. 2.1).

Additionally, the correction in the resonance strengths (the numerator of Eq. 2.3) is small for the values of s under consideration, so we can safely approximate $B_j \approx 1$. As we show in the results presented below, we can describe the far-field scattering (through α in Eq. 2.3) for metal nanoparticles including retardation using the set of four real numbers ϵ_j, V_j, a_{j2} and a_{j4}.

The resonant permittivities ϵ_j are found by fitting the position and strength of the peak associated with mode j in the absorption spectrum of the particle, calculated in the electrostatic limit. The near field $\mathbf{E}_j$ is then taken as the induced field computed when the light frequency is tuned to the absorption maximum. Upon normalization of the field according, we further compute the mode volume V_j from Eq. 2.2, and a_{j2} and a_{j4} from Eq. 2.5. We plot these four parameters in Fig. 2.1 for three common morphologies (rods with hemispherical caps at the tips, equilateral triangles, and cubic cages), as a function of aspect ratio R (see upper insets). We also provide analytical R-dependent fits in Table 2.1. Additional sets of parameters are provided in Appendix C (Fig. C.1 and Table C.1) for other geometries. The latter is used in the analytical calculations of Fig. 2.8. For axially symmetric structures, the electrostatic modes are obtained using the boundary element method (BEM),[94] whereas for other morphologies we use a finite-difference method (COMSOL). As expected, we observe a trend toward larger negative values of ϵ_j with increasing R (*i.e.*, with decreasing metal volume for fixed length), which implies a redshift in plasmon frequency as the metal shapes are thinned. Additionally, the lowest-order plasmon mode generally contributes with a large fraction to the total volume, indicating that this is the dominant mode in the spectrum.

2.2.3 Plasmon frequency

Plasmons are associated with resonant values of the dielectric function of the metal close to one of the eigenvalues ϵ_j, which are negative real numbers. Losses in actual

metals are proportional to $\mathrm{Im}\{\epsilon_\mathrm{m}\} > 0$, implying finite plasmon lifetimes. It is instructive to approximate $\epsilon_\mathrm{m}(\omega) \approx \epsilon_\mathrm{m}(\omega_j) + \epsilon'_\mathrm{m}(\omega_j)(\omega - \omega_j)$ around the real frequency ω_j, defined by $\mathrm{Re}\{\epsilon_\mathrm{m}(\omega_j)\} = \epsilon_\mathrm{h}\epsilon_j$, where the prime denotes differentiation with respect to the argument. In the absence of retardation, the complex plasmon frequency $\tilde{\omega}_j$ must satisfy $\epsilon_\mathrm{m}(\tilde{\omega}_j) = \epsilon_\mathrm{h}\epsilon_j$, which, using the above approximation and assuming $\mathrm{Im}\{\epsilon_\mathrm{m}\} \ll |\epsilon_\mathrm{m}|$, leads to $\tilde{\omega}_j \approx \omega_j - \mathrm{i}/2\tau_j$, where $\tau_j = \mathrm{Re}\{\epsilon'_\mathrm{m}(\omega_j)\}/\mathrm{Im}\{\epsilon_\mathrm{m}(\omega_j)\}$. From the physical condition[48] $\mathrm{Re}\{\epsilon_\mathrm{m} + \omega\epsilon'_\mathrm{m}\} \geq 0$, we find $\tau_j > 0$. Additionally, the time dependence of the intensity $\propto |e^{-\mathrm{i}\tilde{\omega}_j t}|^2 = e^{-t/\tau_j}$ clearly reveals τ_j as the plasmon lifetime.

Among common materials, the condition of relatively small $\mathrm{Im}\{\epsilon_\mathrm{m}\}$ is best satisfied by noble metals in the visible and near-infrared spectral regimes. In particular, gold, silver, and copper, exhibit a Drude-like response that can be characterized by the expression given in Eq. 1.10 as

$$\epsilon_\mathrm{m}(\omega) = \epsilon_\mathrm{b} - \frac{\omega_\mathrm{p}^2}{\omega(\omega + \mathrm{i}\tau^{-1})} \tag{2.6}$$

with parameters ϵ_b, ω_p, and τ as shown in Table 1.1. This model provides a reasonable description of the measured dielectric function[28] using constant values of ϵ_b for wavelengths above the interband transitions. At longer wavelengths, the lifetime of nonretarded plasmons is directly inherited from the Drude model ($\tau_j \approx \tau$).

Retardation enters through $A_j(s)$ Eq. 2.4, which for small values of the size parameter s (*i.e.*, $|A_j| \ll 1$), using Eq. 2.6 to calculate the corresponding pole of Eq. 2.3, leads to the complex plasmon frequency

$$\tilde{\omega}_j \approx \frac{\omega_\mathrm{p}}{\sqrt{\epsilon_\mathrm{b} - \epsilon_\mathrm{h}\epsilon_j}}\left[1 - \frac{A_j}{2}\frac{\epsilon_\mathrm{h}(\epsilon_j - 1)^2}{\epsilon_\mathrm{b} - \epsilon_\mathrm{h}\epsilon_j}\right] - \frac{\mathrm{i}}{2\tau}. \tag{2.7}$$

This expression predicts both a frequency redshift (note that the a_{j2} term in Eq. 2.4 is positive, see Fig. 2.1) roughly proportional to $-\epsilon_\mathrm{h}(L/\lambda)^2$, accompanied by an increase in plasmon linewidth from $1/\tau$ to

$$\Delta\omega_j \approx \frac{1}{\tau} + \frac{4\pi^2\omega_\mathrm{p}}{3}\frac{V_j}{\lambda^3}\frac{\epsilon_\mathrm{h}^{5/2}(\epsilon_j - 1)^2}{(\epsilon_\mathrm{b} - \epsilon_\mathrm{h}\epsilon_j)^{3/2}}, \tag{2.8}$$

where the second term accounts for the contribution of radiative damping.

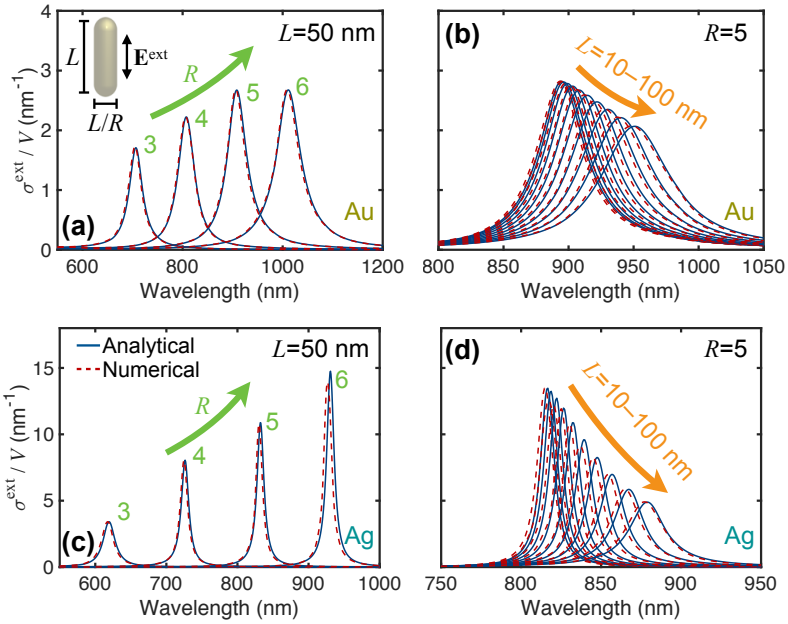

Figure 2.2: **Analytical description of light extinction by gold and silver nanorods.** We illustrate the power of the present analytical method by comparing extinction spectra calculated either with the analytical model (solid curves) or via numerical solution of Maxwell's equations[94] (broken curves) for gold (a,b) and silver (c,d) nanorods immersed in water. We consider several aspect ratios R for fixed length $L = 50\,\text{nm}$ in (a,c) and various rod lengths L for fixed aspect ratio $R = 4$ in (b,d).

2.3 Optical response for different morphologies

2.3.1 Extinction spectra

Gold and silver nanorods are among the most common anisotropic nanoparticles, for which colloid synthesis protocols are well established.[95] Rod-like particles are also extensively fabricated by nanolithography for plasmonic studies, offering a broader versatility in the choice of material and particle location at the expense of a lower degree of control over size and defects. We thus put our analytical method to the test by comparing its ability to predict plasmons for a vast range of nanorod sizes and aspect ratios. We concentrate on modes with polarization along the length of the rods, as these are more sensitive to retardation and shape effects. Figure 2.2 presents a study for gold and silver nanorods ($\epsilon_{\rm m}$ taken from measured data[28]) embedded in water ($\epsilon_{\rm h} = 1.77$). We plot extinction cross-section spectra calculated from Eq. 1.13

$$\sigma^{\rm ext}(\omega) = \frac{8\pi^2}{\sqrt{\epsilon_{\rm h}}\lambda}{\rm Im}\{\alpha(\omega)\}, \tag{2.9}$$

using the polarizability of Eq. 2.3 with the parameters of Table 2.1 (solid curves). These results are compared with full numerical solutions of Maxwell's equations obtained from the BEM[94] (dashed curves). We concentrate on the region around the lowest-order dipolar mode, for which the analytical model is found to be in excellent agreement with the full numerical results. In particular, it accurately predicts the redshift in plasmon energy with increasing aspect ratio R and rod length L for both metals under consideration. The redshift with R was anticipated in Fig. 2.1 from the evolution of the mode permittivity ϵ_1 and is generally known to be the result of a shape-dependent depolarization. In contrast, the redshift with L originates from retardation: as the size increases, it takes a longer time for the electromagnetic field generated by induced changes in one end of the rod to reach the other end, thus reducing the frequency at which they oscillate collectively. Additionally, plasmons in silver nanorods are blue shifted with respect to those in gold, for the same geometry, as a result of weaker d-band screening (*i.e.*, $\epsilon_{\rm b}$ is smaller in silver, see Eq. 2.6 and Table 1.1). Also, gold plasmons are broader because the intrinsic lifetime τ is shorter in this material.

2.3.2 Plasmon wavelength and width

An overview of the resonance wavelengths for gold rods and triangles as a function of size and aspect ratio is presented in Fig. 2.3a-b, where we observe again a systematic redshift with increasing L and R. A similar trend is observed for other types of particles composed of gold (Fig. 2.3c-d). In all cases, the agreement between analytical (solid

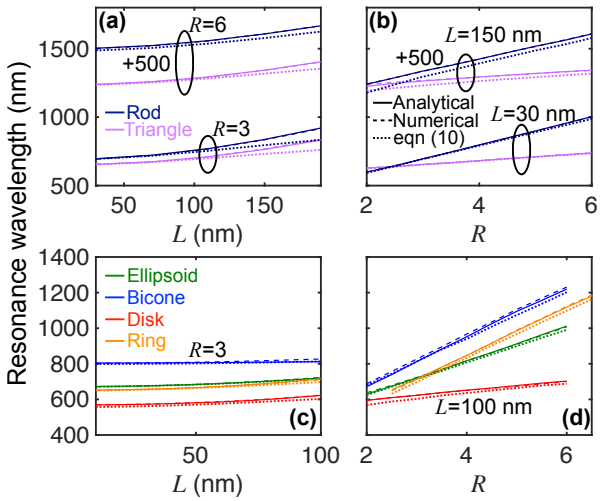

Figure 2.3: **Overview of the analytical model performance: plasmon wavelengths.** We show the resonance wavelength corresponding to the maximum optical extinction for various types of gold nanoparticles embedded in water with either fixed aspect ratio (a,c) or fixed size length (b,d) as obtained from our analytical model (solid curves) or from fully numerical solution of Maxwell's equations (broken curves). Results from the simple Drude-model expression of Eq. 2.7 are shown as dotted curves (plasmon wavelength taken as $2\pi c/\mathrm{Re}\{\tilde{\omega}_j\}$).

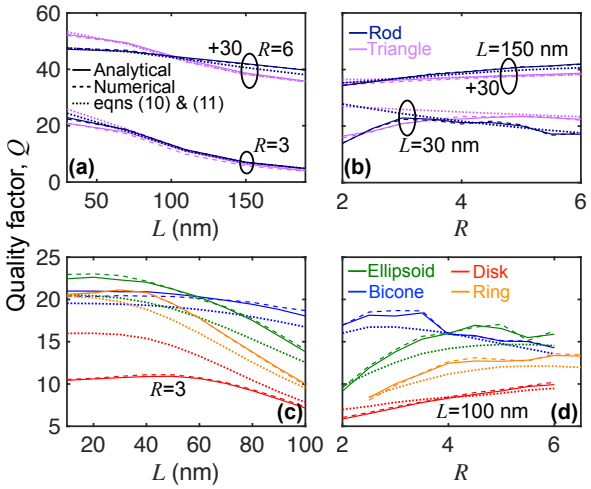

Figure 2.4: **Overview of the analytical model performance: quality factors.** We show the plasmon quality factor Q under the same conditions as in Fig. 2.3. Dotted curves are obtained from the simple analytical approximation $Q = \mathrm{Re}\{\tilde{\omega}_j\}/\Delta\omega_j$ (Eqs. 2.7 and 2.8) with $\epsilon_\mathrm{b} = 9.5$ in (a) and (b) and with a frequency-dependent $\epsilon_\mathrm{b}(\omega)$ in the rest of the panels (see Table 1.1).

curves) and numerical (dashed curves) calculations is excellent. Remarkably, the shape and size dependence of the plasmon wavelengths are also well predicted by approximating the metal response in the Drude limit (*i.e.*, with a constant value of ϵ_b to represent interband transitions (dotted curves in Fig. 2.3, calculated from Eq. 2.7).

In general, plasmons with longer lifetime emerge as narrower features in the spectra, and they are associated with stronger near fields. A quantification of these properties is provided by the plasmon quality factor $Q = \omega/\Delta\omega$, which we define as the ratio of peak frequency to the full width at half maximum (FWHM) of the plasmon feature in the extinction spectrum. This quantity is also equal to 2π times the number of self-sustained plasmon charge oscillations before the near-field intensity decreases by a factor of e after the external illumination ceases. Quality factors in the range of a few tens are common in noble metals nanoparticles, as illustrated in the summary presented in Fig. 2.4 for different particle morphologies and compositions. Once more, excellent agreement in plasmon width is observed between the analytical model and full numerical calculations. In contrast to the systematic redshift of the plasmon with increasing size and aspect ratio, the quality factor exhibits a more complex behavior, which can be understood from the interplay between the L and R dependences of the

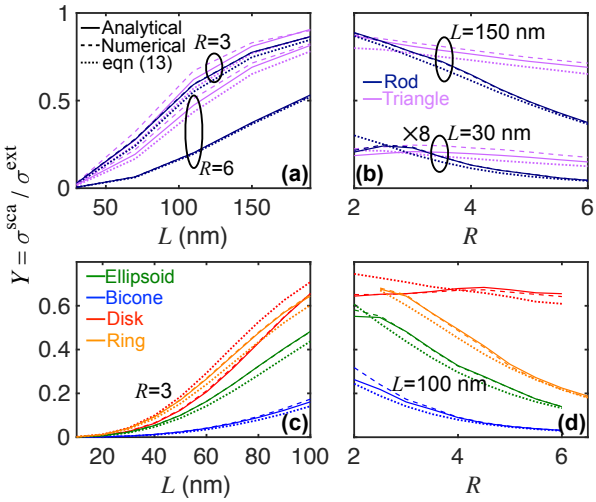

Figure 2.5: **Plasmon quantum yield.** We show the ratio between electric-scattering and extinction cross-sections at the peak extinction frequency under the same conditions as in Fig. 2.3. Dotted curves correspond to the approximate expression of Eq. 2.10, where we use the analytically fitted permittivities of Table 1.1 (for a frequency-dependent $\epsilon_b(\omega)$ term).

plasmon lifetime (see Eq. 2.8): for fixed R (Fig. 2.4a,c), the quality factor decreases with increasing L as a result of radiation losses; for fixed size (Fig. 2.4b,d), there is a relatively mild dependence with aspect ratio that is inherited from the redshift (higher resonant $-\mathrm{Re}\{\epsilon_m\}$) with increasing R. Incidentally, the simple expressions of Eqs. 2.7 and 2.8 constitute an excellent approximation to calculate the quality factor as $Q = \mathrm{Re}\{\tilde{\omega}_j\}/\Delta\omega_j$ (Fig. 2.4, dotted curves), which works well for gold rods and triangles even when taking a constant value of the interband contribution to the permittivity ($\epsilon_b = 9.5$), although a frequency-dependent $\epsilon_b(\omega)$ (see Table 1.1 for a detailed expression) is necessary to obtain good agreement in the rest of the cases (Fig. 2.4c-d).

2.3.3 Plasmon quantum yield

Plasmons are extensively used to modify the lifetime and emission characteristics of point emitters such as molecules and quantum dots. Before we analyze plasmon-emitter coupling in more detail (see below), let us consider an important figure of merit that characterizes plasmons in this respect: the fraction of energy emanating from them in the form of propagating light. This is the so-called quantum yield of the

plasmon, which can be extracted from far-field measurements as the ratio between elastic-scattering and extinction cross-sections. For small particles described through their polarizability, the extinction cross-section is given by Eq. 2.9, whereas the elastic scattering cross-section reduces to[96] $\sigma^{\text{sca}} = (128\pi^5/3\lambda^4)|\alpha(\omega)|^2$ (see also Eq. 1.13). The ratio between these two quantities (*i.e.*, the quantum yield) then becomes

$$Y = \frac{\sigma^{\text{sca}}(\omega)}{\sigma^{\text{ext}}(\omega)} = \frac{16\pi^3\sqrt{\epsilon_{\text{h}}}}{3\lambda^3}\frac{1}{\text{Im}\{-1/\alpha(\omega)\}} \approx \left[1 + \frac{3\lambda^3}{4\pi^2\sqrt{\epsilon_{\text{h}}}V_1}\,\text{Im}\left\{\frac{1}{\epsilon_{\text{h}} - \epsilon_{\text{m}}}\right\}\right]^{-1}. \tag{2.10}$$

The approximate expression at the end of Eq. 2.10 is obtained by making use of Eq. 2.3, assuming that a single mode $j = 1$ dominates the scattering spectra. It is remarkable that the retardation parameters a_{12} and a_{14} do not appear explicitly in this result.

The quantum yield is plotted in Fig. 2.5 as a function of particle size and aspect ratio for gold nanorods and nanotriangles. We find again an excellent agreement between the analytical model (solid curves) and numerical electromagnetic simulations (broken curves), for which Y is computed as the ratio of cross sections at the peak frequency of σ^{ext}. Additionally, excellent agreement is obtained with the analytical approximation of Eq. 2.10 (dotted curves), using Eq. 2.6 for ϵ_{m} with the frequency-dependent fits of $\epsilon_{\text{b}}(\omega)$ given in Table 1.1. These results confirm the expected increase in quantum yield with increasing particle size (Fig. 2.5a) because the radiative loss channel becomes more relevant due to stronger coupling to radiation (*i.e.*, the particle dipole roughly scales linearly with particle volume). Additionally, the quantum yield decreases with increasing aspect ratio for a fixed size (Fig. 2.5b) because of the combination of two effects: the volume is reduced, thus making the plasmon dipole smaller; and the plasmon redshift discussed above contributes to make the particle comparatively smaller in front of the emission wavelength, therefore reducing the relative contribution of radiation losses.

2.4 Overview comparison with experiments

We illustrate the versatility of the analytical model to cope with other types of metals in Fig. 2.6, where we compare experiments taken from Zoric *et al.*[97] for lithographically-patterned gold, platinum, and aluminum nanodisks (upper panels) with theory (lower panels). Excellent results are obtained, except for very small aluminum disks, where the presence of a self-limited oxide layer[97] (not accounted for in theory) can influence the optical response. We stress that the simulations are obtained using just the entries for disks in Table C.1 of Appendix C, which are independent of size and

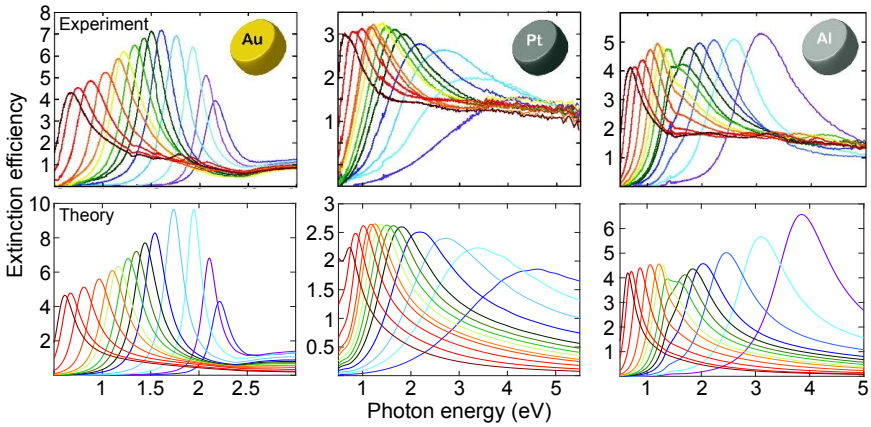

Figure 2.6: **Comparison of measured (upper panels) and analytically-calculated (lower panels) spectra for disks of varied sizes and compositions.** We show experimental spectra taken from Zoric *et al.*[97] for disks lithographically patterned on gold, platinum, and aluminum (see insets), compared with calculations performed using our analytical model. Calculations use the measured dielectric functions for Au,[28] Pt,[98] and Al.[98] The disk thickness is 20 nm in all cases, while the disk diameter varies from ∼50-550 nm, ∼40-500 nm, and ∼70-550 nm in Au, Pt, and Al, respectively. We take the host permittivity $\epsilon_{\mathrm{h}} = 1.26$ as the average value between air and the supporting glass substrate.

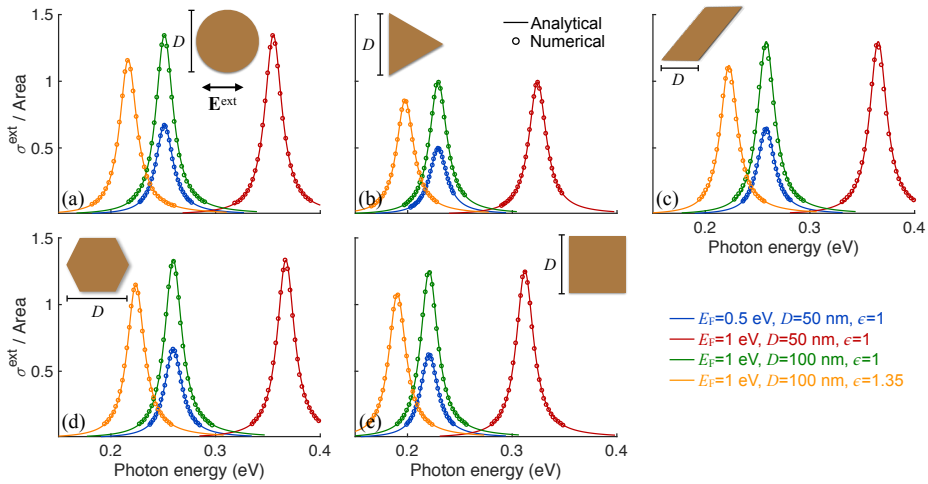

Figure 2.7: **Analytical description of plasmons in graphene islands of different morphology.** We present the extinction cross-section for (a) disks, (b) triangles, (c) ribbons, (d) hexagons, and (e) squares. In each figure, analytical results obtained using the plasmon wave function (PWF) of the lowest-order dipolar mode (solid curves) are compared with numerical simulations (symbols) for different combinations of characteristic size D, graphene Fermi energy E_F, and surrounding dielectric permittivity ϵ (see color-coded legend). We describe the graphene surface conductivity using the Drude model (Eq. 1.17), adopting a phenomenological inelastic damping energy $\hbar\tau^{-1} = 20\,\text{meV}$ (*i.e.*, $\tau \approx 33\,\text{fs}$) and considering normally-impinging light polarized in the direction indicated in the inset of panel (a).

material, and they cover a wide range of aspect ratios $R = 2-27$. Also, the optical response of dewetted nanoparticles has been successfully described by this analytical model.[80]

2.5 Plasmon wave functions in different graphene morphologies

The optical response of graphene nanoislands is well-described in the electrostatic limit, as their plasmon resonance wavelengths typically appear in the infrared regime, where the light wavelength is much larger than the plasmon wavelength of the material.[38,99] In Section 1.2.2 and Appendix A, an eigenmode expansion method has been adopted to express the linear optical response of a graphene nanostructure in

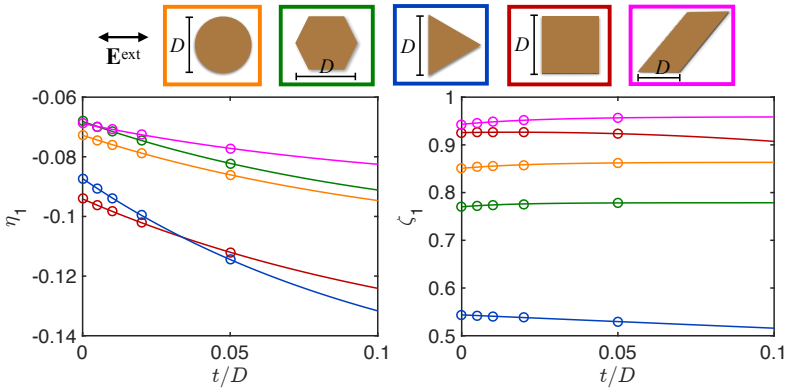

Figure 2.8: **Thickness dependence of the PWF analytical parameters.** We present the eigenvalue η_1 and normalized dipole moment ζ_1 for the lowest-order dipolar plasmon mode of disks, triangles, ribbons, hexagons, and squares (see symbols, which are color-coded with the borders of the upper inset figures) as a function of the normalized effective graphene thickness t/D, where the characteristic size D of a structure is indicated in the upper insets along with the light polarization direction (double arrow). Symbols for η_1 are obtained by fitting the numerically computed extinction spectra in the electrostatic limit, while ζ_1 is calculated using Eq. A.23. Solid curves, color-coded to the borders of the upper inset figures, correspond to the fitted expressions provided in Table 2.2.

terms of its supported plasmon modes. Alternatively, one can associate a plasmon mode j with its induced charge distribution, which we refer to as the plasmon wave function (PWF) of mode j.[100] We demonstrate the power of the PWF formalism in Fig. 2.7. In the spectral region dominated by the lowest-order plasmon mode ($j = 1$) supported by graphene islands of different morphology, we compare extinction spectra predicted in the analytical PWF description (solid curves) with those obtained upon a fully-numerical finite-element solution of Maxwell's equations (dashed curves). We find excellent agreement among analytical and numerical results, regardless of the nanostructure characteristic size D, graphene Fermi energy E_F, or dielectric permittivity of the surrounding environment ϵ (see colored labels). Here and in what follows in this chapter, we describe the graphene surface conductivity in the Drude approximation (see Eq. 1.17), adopting a phenomenological inelastic damping rate $\hbar\tau^{-1} = 20\,\text{meV}$ (*i.e.*, $\tau \approx 33\,\text{fs}$, see Eq. 1.17).

The analytical model used to produce the results presented in Fig. 2.7 is based on two parameters: the plasmon mode eigenvalue η_j and dipole moment ζ_j, where the index j is a mode index and in this figure we focus on $j = 1$, the lowest-order plasmon

	disk	hexagon	triangle	square	ribbon
a_η	0.03801	0.03846	0.07418	0.05537	0.02326
b_η	-8.569	-9.105	-9.106	-7.795	-8.878
c_η	-0.1108	-0.1066	-0.1615	-0.1495	-0.09208
a_ζ	-0.01267	-0.008482	1	-2.752	-0.01572
b_ζ	-45.34	-62.02	-0.2826	0.09027	-39.21
c_ζ	0.8635	0.7787	-0.4563	0.9258	0.9588

Table 2.2: Fitting functions for $\eta_1 = a_\eta \exp\left(b_\eta x\right) + c_\eta$ and $\zeta_1 = a_\zeta \exp\left(b_\zeta x\right) + c_\zeta$ corresponding to graphene islands of different morphologies as a function of the normalized thickness $x = t/D$. We apply these expressions for all morphologies considered in Fig. 2.8 except the graphene square, for which we have $\zeta_1 = a_\zeta x^2 + b_\zeta x + c_\zeta$.

supported by each of the graphene islands under consideration. These two parameters are independent of the material properties, and in fact, they are determined by geometrical features alone. This means that the PWF treatment can also be used to describe other nanostructured 2D materials characterized by an isotropic surface conductivity. More precisely, the eigenvalue η_j corresponds to the resonant value of the quantity $\eta = \mathrm{i}\sigma(\omega)/D\omega\epsilon$, where $\sigma(\omega)$ is the graphene conductivity. Using the Drude model for graphene conductivity (Eq. 1.17), the plasmon frequency of mode j can be analytically resolved in terms of the eigenvalue as[38] $\omega \approx \omega_j - \mathrm{i}\tau^{-1}/2$ with

$$\omega_j = \frac{e/\hbar}{\sqrt{-\pi\eta_j\epsilon}} \sqrt{\frac{E_\mathrm{F}}{D}}. \tag{2.11}$$

Plasmons are then associated with negative eigenvalues $\eta_j < 0$. This expression explains why the analytical model undergoes a minor redshift of the plasmon resonance peaks in all cases considered in Fig. 2.7 when the average surrounding permittivity ϵ increases from 1 to 1.35. We note that according to Eq. 2.11 the resonance positions for structures with the same value of $\sqrt{E_\mathrm{F}/D\epsilon}$ should coincide, as illustrated by the green and blue curves.

The results of Fig. 2.7 correspond to islands of zero thickness. However, the charge that is optically induced on the graphene as the result of the excitation of a plasmon spans a finite thickness determined by the spatial extension of the out-of-plane carbon p orbitals. A value of $\sim 0.34\,\mathrm{nm}$ is typically used, corresponding to the inter-plane distance in graphite. Although this is an *ad hoc* parameter, it has been used in many prior studies of graphene plasmonics. Then, the thickness of the island t has a finite value that can influence the plasmons. We thus present in Fig. 2.8 the dependence of the eigenvalue and dipole-moment parameters on the normalized thickness t/D. We

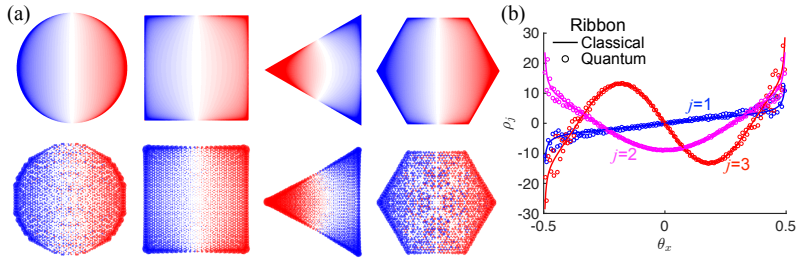

Figure 2.9: **Classical vs quantum PWFs.** (a) Density plots of the PWFs for the lowest-order ($j = 1$) dipole mode are presented in the top row for several graphene geometries using the classical quasistatic model, whereas in the bottom row we show the induced charge distributions at the spectral position of the lowest-order plasmon resonance computed using an atomistic quantum model (see Section 1.3). Blue and red colors represent charges of opposite signs. (b) PWFs of the first three lowest-order ($j = 1-3$, see labels) plasmon modes in graphene ribbons along the transversal ribbon direction x are obtained using the classical model (solid curves). The induced charge distribution from the quantum model is presented as symbols for the two dipole-active bright modes ($j = 1, 3$). The orientation of the incident light is along the ribbon width. In the quantum calculations we take $D = 10\,\text{nm}$, $8.8\,\text{nm}$, $15\,\text{nm}$, $10\,\text{nm}$, and $20\,\text{nm}$ for the disk, square, triangle, hexagon, and ribbon, respectively (see upper insets of Fig. 2.8). These values correspond to $\sim 2000-3000$ carbon atoms for the finite islands.

find that the mode eigenvalue, which determines the plasmon resonance frequency, is more sensitive to variations of t/D, while the mode dipole moment ζ_1 is relatively robust. We thus conclude that the spectral position of a plasmon resonance predicted for a graphene nanostructure described with a nonzero thickness is more prone to inaccuracy unless a proper treatment of the thickness parameter is performed. Incidentally, the mode eigenvalues η_1 are obtained by fitting numerically-computed extinction spectra in the electrostatic limit for the lowest-order plasmon mode, while ζ_1 is calculated using Eq. A.23. We also provide t/D-dependent fits (solid curves in Fig. 2.8) in Table 2.2.

We present in Fig. 2.9 the spatial distributions of PWFs $\rho_1(\vec{\theta})$ as a function of the normalized in-plane position vector $\vec{\theta} \equiv \mathbf{R}/D$ corresponding to the lowest-order plasmon mode contained in the collection of graphene structures considered here. In the upper row of Fig. 2.9a, we present PWFs obtained using the classical model, with blue and red colors representing charges of opposite sign, so that the charge neutrality condition $\int d^2\vec{\theta}\, \rho_1(\vec{\theta}) = 0$ is evident upon inspection. For comparison, the induced charge distributions of the same modes obtained from an atomistic quantum

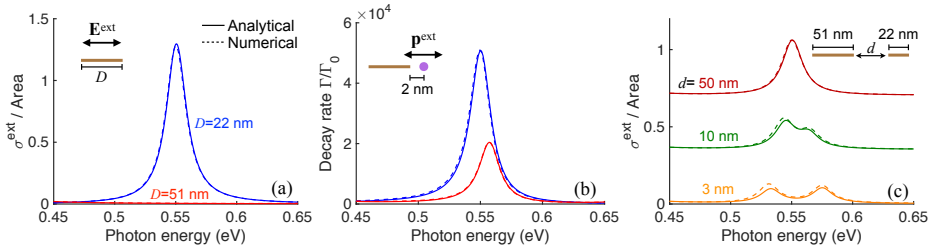

Figure 2.10: **Plasmon-induced transparency in paired graphene ribbons.** (a) Optical response of individual graphene ribbons of widths $D = 22\,\text{nm}$ (blue curves) and 51 nm (red curves) under normal incidence with light polarization across the width of the ribbon. We assume $E_F = 1\,\text{eV}$ in all cases. The peak in extinction around 0.55 eV corresponds to the lowest-order plasmon mode in the smaller ribbon, while the contribution from the larger ribbon is negligible in the frequency range shown. (b) Decay-rate enhancement for an external unit dipole $\mathbf{p}^{\text{ext}}$ placed 2 nm away from the edge of the ribbons considered in panel (a). The dipole is oriented along the ribbon width. (c) Optical response of dimers composed of the two ribbons presented in panel (a) separated by an edge-to-edge distance d in a co-planar configuration. When the separation distance d decreases from 50 to 3 nm (see labels), a transparency window appears around 0.55 eV in the extinction spectra as a result of the interaction between the $j = 1$ mode (lowest-order dipole mode) in the smaller ribbon and the $j = 2$ mode (first dark mode) in the larger one. Our analytical results (solid curves) agree well with numerical simulations (broken curves) in all cases.

model, introduced in Section 1.3, for graphene islands with lateral sizes on the order of $\sim 10\,\text{nm}$ are presented in the lower row of Fig. 2.9a. We denote these induced charges associated with the plasmons as quantum PWFs. The similarity between PWFs obtained from the classical and quantum models clearly indicates that the concept also holds in the quantum regime. In Fig. 2.9b, PWFs for the first three lowest-order plasmon modes ($j = 1 - 3$, see labels) are shown for a 1D graphene nanoribbon, where the $j = 2$ mode, yielding $\zeta_2 = 0$, is a dark plasmon.

2.6 Graphene-nanostructure interactions and plasmon-induced transparency

We consider a system composed of multiple graphene structures, indexed by n and centered at the positions $\mathbf{r}_n$. We now define $\vec{\theta} \equiv (\mathbf{r}_\parallel - \mathbf{r}_n)/D_n$, where $\mathbf{r}_\parallel$ indicates the in-plane position vector of the corresponding island and D_n is a characteristic

normalization length. We also define the eigenvalue η_{nj}, eigenmode $\vec{\mathscr{E}}_{nj}$, PWF ρ_{nj}, and mode dipole moment $\vec{\zeta}_{nj}$ for the plasmon mode j associated with the corresponding graphene island n. Then, the self-consistent electric field $\vec{\mathscr{E}}$, having contributions from each island, can be expressed as $\vec{\mathscr{E}} = \sum_{nj} a_{nj}\vec{\mathscr{E}}_{nj}$. From Eqs. A.17-A.19, we obtain the self-consistent expression

$$a_{nj}(\omega) = \frac{\epsilon}{D_n/\eta_{nj} - D_n/\eta^{(n)}(\omega)} \left[C_{nj} + \sum_{n'\neq n} \sum_{j'} V_{nj,n'j'} a_{n'j'} \right]$$

for the expansion coefficients $a_{nj}(\omega)$, where $C_{nj} = -D_n \vec{\zeta}_{nj} \cdot \mathbf{E}^{\text{ext}}$ and $\eta^{(n)}(\omega) = \mathrm{i}\sigma^{(n)}(\omega)/(D_n \omega \epsilon)$ with the conductivity $\sigma^{(n)}(\omega)$ of island n. Here,

$$V_{nj,n'j'} = \frac{D_{n'}^2}{\epsilon} \int d^2\vec{\theta} \int d^2\vec{\theta}' \frac{\rho_{nj}(\vec{\theta})\rho_{n'j'}(\vec{\theta}')}{|D_n\vec{\theta} - D_{n'}\vec{\theta}' + \mathbf{d}_{nn'}|}$$

describes the interaction between plasmon modes j and j' in two islands separated by a vector $\mathbf{d}_{nn'} = \mathbf{r}_n - \mathbf{r}_{n'}$. After solving for all a_{nj}'s, the total induced dipole moment can be expressed as

$$\mathbf{p}^{\text{tot}} = \sum_{nj} D_n^3 a_{nj} \vec{\zeta}_{nj}.$$

Eventually, the extinction cross-section of the whole system can be calculated as

$$\sigma^{\text{ext}}(\omega) = \frac{4\pi\omega}{\sqrt{\epsilon}|\mathbf{E}^{\text{ext}}|^2 c} \mathrm{Im}\left\{ (\mathbf{E}^{\text{ext}})^* \cdot \mathbf{p}^{\text{tot}} \right\}. \tag{2.12}$$

As a way to demonstrate the versatility of above PWF formalism for interacting graphene nanostructures, we study the optical response of graphene structures interacting with external elements or with one another, as shown in Fig. 2.10. In Fig. 2.10a we first present the optical extinction spectra of isolated graphene nanoribbons with different widths D, both of which are doped to $E_{\text{F}} = 1$ eV, and we include modes up to $j \leq 3$ (see Fig. 2.9b). The decay-rate enhancement for an external unit dipole $\mathbf{p}^{\text{ext}}$ (solid curves, shown in Fig. 2.9b) is calculated analytically from Eq. A.25. In the frequency range shown, a prominent peak associated with the $j = 1$ dipolar mode supported in the smaller ribbon ($D = 22$ nm, blue curves) appears around 0.55 eV, whereas the contribution from the larger ribbon ($D = 51$ nm, red curves) is negligible at that energy. However, as shown in Fig. 2.10b, where we simulate the decay rate of an oscillating unit dipole $\mathbf{p}^{\text{ext}}$ in the presence of either ribbon, a resonance feature appears in the spectrum for the larger one, which corresponds to its $j = 2$ dark mode. This dark mode plays an important role when considering the optical response of a dimer formed by the co-planar combination of the two ribbons, with an edge-to-edge

separation distance d, as shown in Fig. 2.10c. The interaction between the bright and dark plasmonic modes in the small and large ribbons, respectively, results in a transparency window appearing around 0.55 eV, which becomes more pronounced as the separation distance decreases from $d = 50\,\text{nm}$ to $d = 3\,\text{nm}$. This phenomenon is known as plasmon-induced transparency, and has several applications, including slow light generation.[101, 102] We note that results based on the PWF formalism are found to be in excellent agreement with fully-numerical simulations.

2.7 Conclusions

As a solution to the complex electromagnetic problem and the sometimes involved details of the optical response presented by metallic nanoparticles, we have extended an analytical model capable of describing such a response accurately when compared with both state-of-the-art numerical methods and experimental data. Remarkably, each particle shape requires only four real numbers to describe the extinction spectrum, wavelength, width, and quantum yield associated with each of its plasmons. These quantities are computed by means of simple analytical expressions involving those real parameters, which are valid for any composition and size of the particles. Importantly, plasmon broadening and redshifts due to retardation are correctly described for a wide variety of particle sizes and morphologies.

The analytical model takes negligible computation time and can be readily applied to any particle shape once the noted parameters are available. As a suggested application to sensing, this method allows a fast assessment of the ability of a given nanoparticle morphology to detect changes in the dielectric environment (*i.e.*, the permittivity of the host medium ϵ_h, which enters the analytical expressions explicitly) through observed variations in the plasmonic response. Insight into inhomogeneities of a colloidal sample can be gained by comparing measurements of the optical extinction to calculated values convoluted with distributions of particle size and aspect ratio, for which the analytical model presents clear advantages. A similar optimization scheme could be applied to systems for surface-enhanced Raman spectroscopy (SERS). The model may also be used to engineer particle shape, in order to render a desired balance between quantum-yield and strength of coupling to localized optical emitters, with potential applications in nanoscale quantum optics. Optical heating assisted by plasmons (thermoplasmonics) may also benefit from this analytical theory.

Finally, we further adapt the theory to two-dimensional materials for studying the optical response of graphene structures with arbitrary morphologies based on plasmon wave functions (PWFs). The present model is analytical and characterizes a plasmon resonance in a given geometry using only two real-valued parameters. The spatial distribution of PWFs calculated from classical modeling is found to be in excellent agreement with those obtained from atomistic quantum-mechanical simulations, even

for structures of small ($\sim 10\,\mathrm{nm}$) lateral size. We apply our analytical model to the study of graphene ribbon dimers, which accurately describes the plasmon-induced transparency that arises when bright and dark modes couple strongly. We note that the present analytical PWF formalism is universal and can be applied to model the optical response of other two-dimensional materials or thin films using their local 2D conductivities as input.

3

Light modulation with graphene

3.1 Introduction

Fast electro-optical modulation of visible and near-infrared (NIR) light is important for a wide variety of applications, ranging from communications, considering the exponential growth of the data traffic in the last decade, to sensing and smart windows. No fundamental limit appears to prevent us from designing wavelength-sized devices capable of controlling the light phase and intensity at gigahertz (and even terahertz) speeds in those spectral ranges. However, this problem remains largely unsolved, despite recent advances in the use of quantum wells and phase-change materials for that purpose. Currently available approaches result in rather bulky devices, suffer from low integrability, and can hardly operate at the low power consumption levels and fast switching rates required by microelectronic drivers.

A possible strategy to achieve visible-NIR (vis-NIR) light modulation consists in exploiting the switching off of graphene absorption when it transits from undoped to doped states: indeed, undoped graphene absorbs 2.3% of the incident light over the vis-NIR range[103,104] as a result of direct electron-hole pair transitions between its lower occupied Dirac cones and the upper unoccupied cones (two inequivalent ones in every Brillouin zone[33,53]); in contrast, when doped to a Fermi energy E_F, an optical gap of size $2E_F$ opens up in which absorption is drastically reduced via Pauli blocking.[105,106] Electrical gating has been used to show $E_F \sim 1$ eV doping,[106] which in principle enables intrinsically fast vis-NIR light modulation. However, the poor amount of absorption produced by this material is limited by its atomic thickness, and consequently, order-one modulation requires coupling it to either strong optical resonances or large structures in which a substantial effect builds up. The latter strategy has been followed to demonstrate active modulation in the NIR light transmitted through graphene-loaded waveguides[107] and photonic crystals,[108,109] although the resulting structures are rather bulky and extend over many optical wavelengths.

In this chapter, we first explore graphene sheets coupled to dielectric planar cavities operating under either tunneling or Fabry-Perot resonant transmission conditions, as well as Mie modes in silicon nanospheres and lattice resonances in metal particle arrays to enhance the light intensity at the graphene plane, and so is its absorption, which can be switched and modulated through varying the level of doping. Unity-order changes in the transmission and absorption of vis-NIR light is produced upon electrical doping of graphene. We also show that planar nanostructures patterned in ultrathin metal-graphene hybrid films sustain highly tunable plasmons in the visible and near-infrared spectral regions. Substantial variations in the reflection and absorption of incident light take place when the plasmons are tuned on- and off-resonance with respect to externally incident light to produce a remarkable modulation depth in both transmission and reflection.

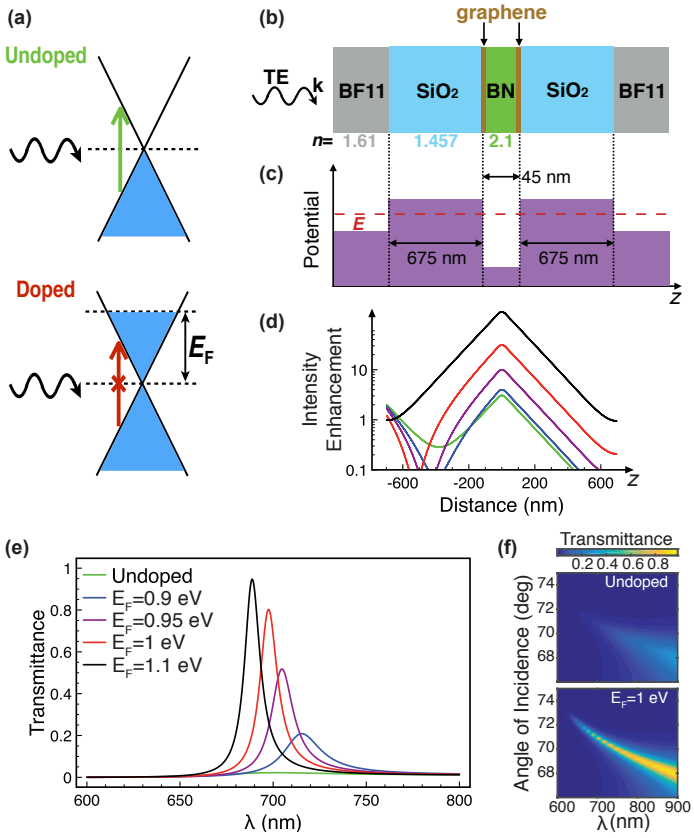

Figure 3.1: **Graphene optical switch based on resonant tunneling transmission.** (a) Doping-induced absorption switching effect: we compare undoped graphene (upper scheme, Fermi level at the Dirac point), which can absorb photons (vertical arrow) over a broad spectral range via interband electron transitions, and doped graphene (lower scheme), in which Pauli exclusion blocks photon absorption when the Fermi energy E_F exceeds half the photon energy. (b) Planar multilayer structure considered for resonant tunneling transmission of light, including a central BN planar waveguide (not to scale) and two single-layer graphene films intercalated at the BN/SiO_2 interfaces. (c) Potential in the equivalent Schrödinger model. (d) Electric field intensity normalized to the external light intensity for an incidence angle of 71° and a free-space wavelength of 689 nm. Light is s- (TE) polarized and incident from the left. Results for different levels of doping are offered (see legend in (e)). (e) Transmission spectra of the multilayer structure at 71° incidence for different levels of doping. (f) Transmission as a function of incidence angle and wavelength for doped and undoped graphene.

3.2 Graphene optical switch based upon resonant tunneling transmission

Due to the strong tunability of graphene, its optical absorption can be switched on/off via electrical doping. In its undoped state it absorbs a fraction $\pi\alpha \approx 2.3\%$ of the incident light[103,104] over a broad spectral range within the vis-NIR as a result of direct electron-hole pair transitions between its lower occupied Dirac cones and the upper unoccupied cones (two inequivalent ones in every Brillouin zone[33,53]). In contrast, when electrically doped, an optical gap is opened that suppresses vertical optical transitions for photon energies below $2|E_F|$, where E_F is the change in Fermi energy relative to the undoped state (see Fig. 3.1a).

We illustrate the concept of resonant switching and modulation of graphene absorption by coupling to a high-quality-factor planar cavity. In particular, we consider the multilayer structure depicted in Fig. 3.1b, consisting of a high-refractive-index boron nitride (BN) planar waveguide ($n_{BN} = 2.1$) flanked by low-index silica spacers ($n_{SiO_2} = 1.457$). The waveguide hosts guided modes that can be resonantly coupled to light of well-defined parallel wave vector (*i.e.*, for a collimated incident beam). In our case, light is incident from the left under total internal reflection conditions at the BF11-SiO_2 interface ($n_{BF11} = 1.61$). The evanescent spill out of light intensity penetrating inside the left silica spacer can reach the BN waveguide, where it is amplified to further extend towards the rightmost interface. In the absence of absorption, full transmission can always be achieved at a resonant wavelength that depends on the incidence angle. This phenomenon, known as resonant tunneling transmission, was previously explored with electron waves.[110] There is a complete analogy between TE light propagation in the planar structure under consideration and the evolution of an electron according to Schrödinger equation.[111] The equivalent electron has energy E and evolves along a potential profile as shown in Fig. 3.1c. The latter is directly related to the refractive index, with the higher index corresponding to lower values of the potential. The presence of a bound state is always guaranteed in a one-dimensional cavity, and so is the existence of a full transmission resonance when this bound state lies inside the potential barrier.[110] Under complete-transmission conditions, the intensity has to decay exponentially from the waveguide to the far medium (*i.e.*, across the rightmost silica barrier), to reach the same value as the incident intensity, so that the near field has to be strongly amplified at the central waveguide. This type of enhancement, which is clearly illustrated in Fig. 3.1d, has been experimentally corroborated by measuring a > 100-fold increase in the fluorescence from quantum dots placed near the central waveguide under resonance conditions in a structure similar to the one considered here.[111]

The structure under consideration (Fig. 3.1b) contains a graphene film on either side of the central BN waveguide. Besides its high index of refraction, the choice of BN

for the central waveguide is convenient because this combination of materials is compatible with high-quality graphene,[112] which can be realistically described with the models for the conductivity σ given in Eq. 1.14. Nevertheless, we assume a conservative value of the graphene mobility $\mu = 2000\,\mathrm{cm}^2/(\mathrm{V\,s})$ in this chapter. Note that the relaxation time τ can be estimated as $\mu E_\mathrm{F}/e{v_\mathrm{F}}^2$ in the DC limit. When the carbon layer is highly doped ($E_\mathrm{F} = 1.1\,\mathrm{eV}$), it becomes nearly lossless (*i.e.*, small $\mathrm{Re}\{\sigma\}$) at the waveguide resonance wavelength, so that the peak transmission reaches $\sim 95\%$ (Fig. 3.1e) and the light intensity enhancement at the waveguide exceeds a factor of 140. In contrast, in the undoped state, the carbon layer becomes lossy (*i.e.*, nearly real $\sigma \approx e^2/4\hbar$), so the enhancement is strongly suppressed, and the transmission drops to very small values. The extinction ratio (*i.e.*, the ratio of transmissions in doped and undoped states) is $> 15\,\mathrm{dB}$. The transmission can be in fact tuned continuously between these two extreme values by varying the level of doping (see Fig. 3.1e). The decrease in transmission produced when moving from highly doped to undoped graphene is due to both absorption and reflection, as the local change in the response of the carbon layer produces a departure from the conditions of resonant tunneling.

The wavelength of operation of this modulator is essentially determined by the waveguide mode, as coupling to the BF11 media is just producing a slight shift. Understandably, the reflection minimum is observed to be only mildly modified when the rightmost glass is removed. Obviously, the resonance wavelength also depends on the angle of incidence and it can be pushed down to the visible regime (Fig. 3.1f), although the maximum transmission decreases towards smaller wavelengths due to the gradual involvement of interband transitions in the graphene.

3.3 Graphene optical switch based upon dielectric resonators

The concept of the tunneling structure in Fig. 3.1 can be extrapolated to other types of resonators in which the incident field also undergoes a large enhancement at a position decorated with graphene. A particularly convenient implementation of this idea is presented in Fig. 3.2, as it allows operating under normal incidence conditions. More precisely, we replace the tunneling structure by a Fabry-Perot (FP) frequency-selective filter, consisting of a cavity flanked by two non-absorbing, nearly perfectly reflecting mirrors. In practical devices, one generally uses Bragg mirrors such as those sketched in Fig. 3.2a, which are easy to fabricate by multilayer deposition. We consider a separation between the FP mirrors that produces a single resonant transmission peak in the $730 - 748\,\mathrm{nm}$ spectral region. At resonance, light is trapped inside the cavity, so it makes many passes through it before escaping, thus generating a large

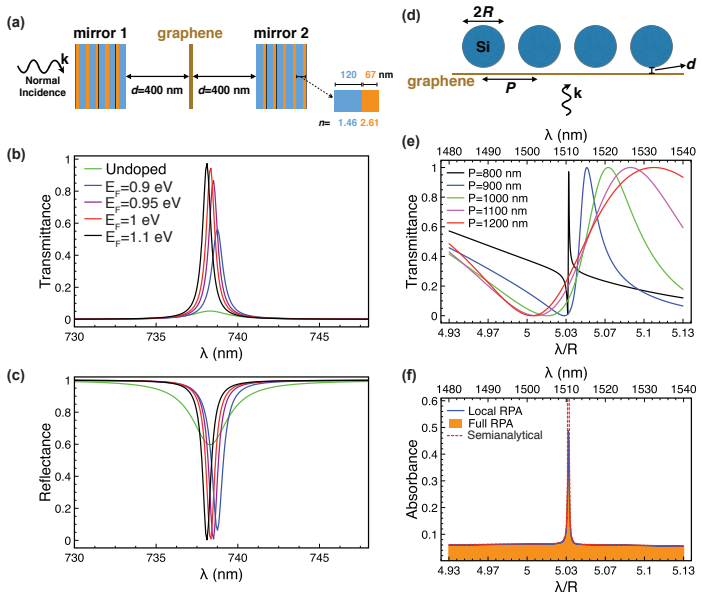

Figure 3.2: **Graphene optical switch based on dielectric resonators.** (a) Fabry-Perot resonator incorporating a tunable graphene layer inside the cavity flanked by two Bragg mirrors (see inset for a sketch of the period and labels for geometrical and optical parameters). (b,c) Normal-incidence transmittance (b) and reflectance (c) for different levels of doping. (d) Geometry and parameters of a triangular array of silicon spheres near graphene. (e) Normal-incidence transmission through the sphere array without graphene for different lattice periods P. The wavelength is shown both normalized to the sphere radius R (lower scale) and for $R = 300\,\text{nm}$ (upper scale). (f) Absorbance of the array when it is placed near undoped graphene (silicon-carbon distance $d = R/150$) under normal incidence. The lattice period is $P = 800\,\text{nm}$. We compare two different approximations for the graphene conductivity (full random-phase approximation[35,36] (RPA) and local-RPA[38]) with a semi-analytical model.

field enhancement at several interference nodes. We place the graphene at one of those nodes. An interplay between absorption (imaginary part of the susceptibility) and polarization (real part) in the graphene is then taking place, leading to large (but not totally complementary) modulations in reflection and transmission, similar to those discussed above for the tunneling device. Similar performance is obtained by filling the cavity with glass and reducing its size, thus configuring a more robust structure.

The transmission/reflection and field enhancement of planar multilayers (results shown in Figs. 3.1 and 3.2b-c) are obtained through a standard transfer matrix approach. In particular, we use the reflection and transmission coefficients for a plane wave of parallel wave vector $k_\parallel$ incident from medium 1 on a graphene layer of conductivity σ placed at the interface with another medium 2, which upon direct solution of Maxwell's equations for the s- (TE) polarization under consideration are found to be[48] $r_{12}^{\rm s}=(k_{z1}-k_{z2}+g_{\rm s})/(k_{z1}+k_{z2}+g_{\rm s})$ and $t_{12}^{\rm s}=2k_{z1}/(k_{z1}+k_{z2}+g_{\rm s})$, respectively, where $g_{\rm s}=4\pi\sigma\omega/c^2$ and $k_{zj}=\sqrt{k^2\epsilon_j-k_\parallel^2+{\rm i}0^+}$. For completeness, we give the coefficients for p- (TM) polarization: $r_{12}^{\rm p}=(\epsilon_2k_{z1}-\epsilon_1k_{z2}+g_{\rm p})/(\epsilon_2k_{z1}+\epsilon_1k_{z2}+g_{\rm p})$ and $t_{12}^{\rm p}=2\sqrt{\epsilon_1\epsilon_2}k_{z1}/(\epsilon_2k_{z1}+\epsilon_1k_{z2}+g_{\rm p})$, where $g_{\rm p}=4\pi\sigma k_{z1}k_{z2}/\omega$. Incidentally, the sign of the square root is chosen to yield positive real values. These expressions also describe the coefficients of interfaces without graphene, simply by taking $g_{\rm s}=g_{\rm p}=0$.

As illustrated in Fig. 3.2e, we consider the silicon spheres to be arranged in a triangular lattice, which we simulate using a layer-KKR approach.[113] This method relies on an expansion of the electromagnetic field in terms of spherical vector waves around the particles and plane waves near the graphene. The scattering by the spheres then involves multiplication by Mie coefficients, whereas the graphene enters through its reflection coefficients (see above). Plane and spherical waves are analytically transformed into each other, giving rise to a self-consistent system of equations projected on the coefficients of the sphere multipoles. Translational lattice symmetry is used to reduce the number of plane waves to those of a discrete set corresponding to different diffraction orders (*i.e.*, two waves of orthogonal polarizations for each reciprocal lattice vector).

Interestingly, there is strong interaction between the particles for the lattice spacings P under consideration, which can be intuitively quantified from the fact that the extinction cross section of the sphere equals the area of a circle of diameter $1.75\,\mu$m. The transmission of the particle array experiences dramatic spectral variations as P is changed, eventually generating a narrow transmission peak, which is relatively close, but not on top of the lowest-order Wood anomaly, occurring when the wavelength is equal to the period at normal incidence; we thus attribute this feature to the interaction between Mie modes of the spheres, as the wavelength is close (but not right on)

a lattice resonance that narrows the resulting spectral feature. A similar mechanism leading to sharp, narrow asymmetric resonances has already been described in the context of cavity-waveguide coupling.[114] The absorbance associated with this narrow peak is boosted, approaching 50% with undoped graphene (Fig. 3.2f), whereas doped graphene shows comparatively negligible absorbance.

In the layer-KKR simulation method,[113] the homogeneous graphene film enters through its reflection and transmission coefficients for different diffracted orders (*i.e.*, a collection of propagating and evanescent plane waves, each of them corresponding to a fixed value of the parallel wave vector). This allows us to use the full random-phase approximation (RPA) conductivity[35,36] $\sigma(k_{\parallel},\omega)$, which includes nonlocal effects associated with finite parallel wave vectors $k_{\parallel}$ corresponding to those diffracted orders. Because the size of the spheres and the lattice periods under consideration are large compared with v_{F}/ω (*i.e.*, the ratio of the graphene Fermi velocity to the light frequency, $\sim 0.8\,\mathrm{nm}$ for a wavelength of $1.5\,\mu\mathrm{m}$), nonlocal effects are in fact negligible, which explains why we obtain the same results on the scale of the figure by just using the value $\sigma = e^2/e\hbar$ for the conductivity in undoped graphene instead of the full RPA. The same argument explains why plasmons are not excited here in doped graphene. Additionally, we obtain very similar results with the semi-analytical model given as

$$\delta\sigma^{\mathrm{abs}} \approx \pi\alpha \int dxdy\, |\mathbf{E}_{\parallel}/E_0|^2, \tag{3.1}$$

where α is the fine structure constant, $\mathbf{E}_{\parallel}$ is the parallel component of the total electric field, E_0 is the incident field, and we apply by averaging the parallel electric-field intensity enhancement over a unit cell. The intensity in the semi-analytical model is calculated without the graphene, just to provide insight into the absorption process. However, when we calculate it including the carbon layer, the absorbance A predicted by Eq. 3.1 cannot be told apart on the scale of the figure from the one given by the far-field transmittance and reflectance (*i.e.*, $A = 1 - T - R$), thus corroborating the numerical accuracy of our calculations.

3.4 Enhanced graphene optical absorption and switching by coupling to lattice resonances

We now discuss the absorption enhancement produced by lattice resonances, for which strong scatters such as metallic particles are preferable. Although metals introduce additional losses, their absorbance is relatively small in the NIR, so graphene can still make a big difference. This is corroborated in Fig. 3.3, where we consider a graphene layer decorated with a 2D square array of gold spheres surrounded by silica for different values of the lattice spacing P. The transmission (Fig. 3.3b) and

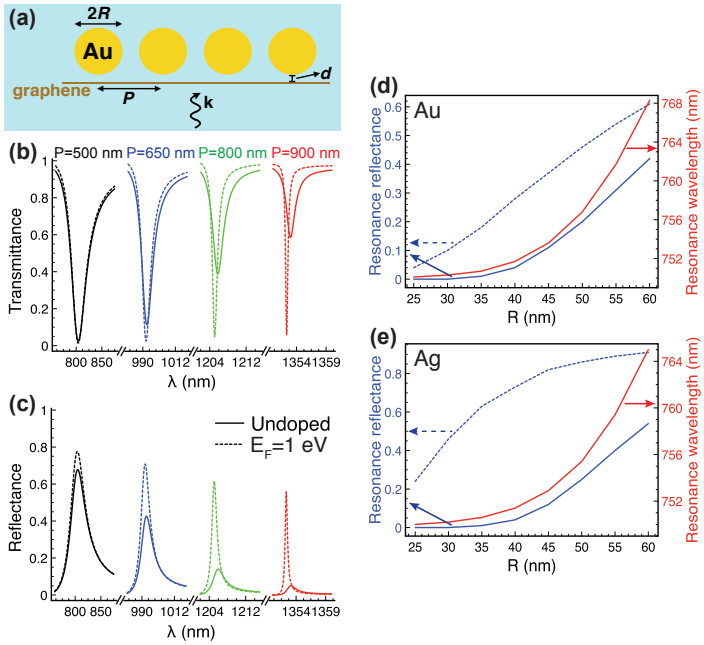

Figure 3.3: **Enhanced tunable graphene absorption by coupling to lattice resonances in 2D metal particle arrays.** (a) A square array of gold spheres (radius R) placed above graphene (2 nm gold-to-carbon separation). The entire system is assumed to be embedded in silica ($\epsilon = 2.25$). (b,c) Normal-incidence transmission (b) and reflection (c) spectra for $R = 80$ nm and different lattice periods P with either doped (broken curves, $E_F = 1$ eV) or undoped (solid curves) graphene. The spectra are dominated by lattice resonances occurring near a free-space light wavelength $\lambda \sim P\sqrt{\epsilon}$. (d) Peak wavelength with doped graphene (right scale) and transmission at that wavelength with either doped or undoped graphene (left scale) as a function of gold sphere radius for a period $P = 500$ nm. (e) Same as (d) for silver particles.

reflection (Fig. 3.3c) spectra (computed by the layer-KKR approach) of these structures exhibit sharp features emerging near the Wood anomaly condition (*i.e.*, when the wavelength in the surrounding dielectric is close to the period, or equivalently, when a diffraction order becomes grazing), which can be easily understood in terms of lattice resonances.[115,116] As the period is increased, these features move to the red, where the metal is less lossy, and consequently, the resonances become narrower. The additional absorption produced by the undoped graphene then becomes more noticeable, eventually causing a decrease in peak transmittance of $\sim 60\%$, accompanied by a 28-fold reduction in reflectance.

3.5 Active modulation of visible light with ultrathin graphene-metal hybrid films (UGMs)

3.5.1 Tunable plasmon quenching in ultrathin UGMs

It is instructive to first discuss plasmons in extended ultrathin graphene-metal hybrid films (UGMs), the dispersion relation of which can be easily obtained by tracing the reflectance of p-polarized light as a function of the parallel component of the wave vector $k_\parallel$ and photon energy.

The $k_\parallel$-dependent reflection coefficient $r_{\rm p}^{\rm UGM}$ for p-polarized light incident on the sandwich structure of Fig. 3.4a can be simply constructed from the air-graphene-metal reflection ($r_{\rm gm} = \Delta_{\rm gm}^-/\Delta_{\rm gm}^+$) and transmission ($t_{\rm gm} = 2\sqrt{\epsilon_{\rm m}}k_{\perp 0}/\Delta_{\rm gm}^+$) coefficients, the metal-graphene-air reflection ($r_{\rm mg} = \Delta_{\rm mg}^-/\Delta_{\rm mg}^+$) and transmission ($t_{\rm mg} = 2\sqrt{\epsilon_{\rm m}}k_{\perp {\rm m}}/\Delta_{\rm mg}^+$) coefficients, and the metal-silica reflection coefficient ($r_{\rm ms} = (\epsilon_{\rm s}k_{\perp {\rm m}} - \epsilon_{\rm m}k_{\perp {\rm s}})/(\epsilon_{\rm s}k_{\perp {\rm m}} + \epsilon_{\rm m}k_{\perp {\rm s}})$). Here $\epsilon_0 = 1$, $\epsilon_{\rm m}$, and ϵ are the permittivities of air, metal, and silica, respectively; $k_{\perp j} = \sqrt{(\omega/c)^2\epsilon_j - k_\parallel^2 + {\rm i}0^+}$ is the normal wave vector in medium $j = 0$, m, s, with the square root chosen such that ${\rm Im}\{k_{\perp j}\} > 0$; and we have defined $\Delta_{\rm gm}^\pm = \epsilon_{\rm m}k_{\perp 0} \pm k_{\perp {\rm m}} + A$, $\Delta_{\rm mg}^\pm = k_{\perp {\rm m}} \pm \epsilon_{\rm m}k_{\perp 0} + A$, and $A = 4\pi\sigma_{\rm g}k_{\perp 0}k_{\perp {\rm m}}/\omega$. From a simple multiple-scattering analysis, we find $r_{\rm p}^{\rm UGM} = r_{\rm gm} + t_{\rm gm}r_{\rm ms}t_{\rm mg}{\rm e}^{2{\rm i}k_{\perp {\rm m}}t}/(1 - r_{\rm ms}r_{\rm mg}{\rm e}^{2{\rm i}k_{\perp {\rm m}}t})$, where t is the metal thickness.

We plot the resulting reflectance $|r_{\rm p}^{\rm UGM}|^2$ for doped and undoped graphene in Fig. 3.4b. Despite the relatively large thickness of the silver layer compared to the monolayer carbon film, it is clear that undoped graphene produces a stronger plasmon damping by coupling to interband transitions,[117] while the opened optical gap in the doped graphene leaves the plasmons almost intact below $\sim 2E_{\rm F}$. External doping can therefore considerably modulate the plasmon strength in UGMs. Obviously, most of the region explored in Fig. 3.4b is far from the light cone, and this indicates that

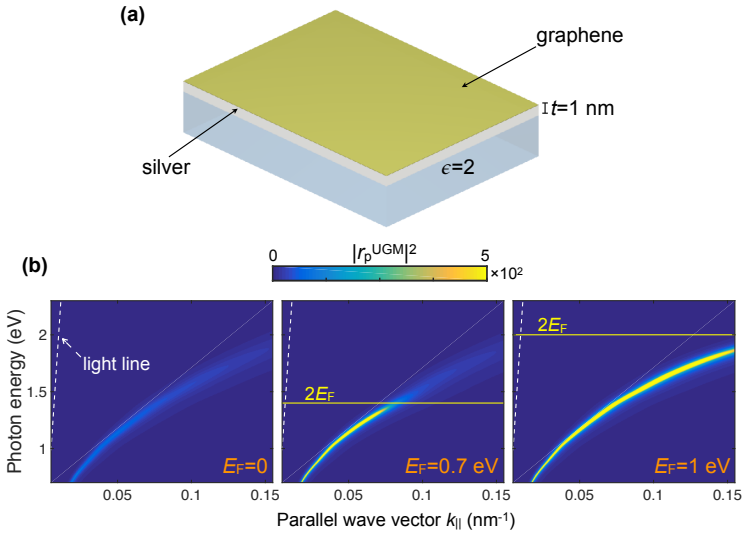

Figure 3.4: **Tunable plasmon quenching in ultrathin graphene-metal hybrid films (UGMs).** (a) Sketch of a UGM consisting of a graphene monolayer on top of an ultrathin silver film (thickness $t = 1\,\text{nm}$), supported in turn by a silica substrate ($\epsilon = 2$). (b) Plasmon dispersion of the structure in (a) when the graphene is either undoped ($E_\text{F} = 0$, left) or highly doped ($E_\text{F} = 0.7\,\text{eV}$, center; $E_\text{F} = 1\,\text{eV}$, right), as illustrated by the photon-energy and parallel-wave-vector dependence of the reflectance for p-polarization. Interband transitions produce strong plasmon quenching in the undoped structure when the photon energy exceeds $2E_\text{F}$ (*i.e.*, above the yellow lines). We model graphene with the local-RPA conductivity (see Eq. 1.14) assuming a mobility $\mu = 2000\,\text{cm}^2/(\text{V s})$, while silver is described by its measured permittivity.[28] The light cone (dashed lines) is shown as a reference.

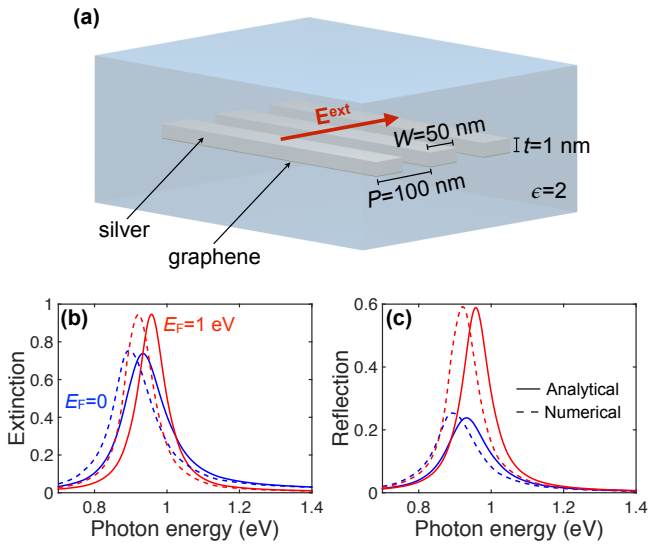

Figure 3.5: **Optical switch based upon a periodic array of silver/graphene UGM ribbons.** (a) Scheme of the structure under consideration. The ribbon array (metal thickness $t = 1$ nm, width $W = 50$ nm, period $P = 100$ nm, embedded in silica, $\epsilon = 2$) is illuminated under normal incidence with transversal polarization. (b,c) Extinction (b) and reflection (c) spectra for either doped (red curves, $E_F = 1$ eV) or undoped (blue curves, $E_F = 0$) graphene, showing $\sim 26\%$ ($\sim 36\%$) modulation depth in extinction (reflection) at 0.92 eV photon energy. Full numerical simulations (dashed curves) are in good agreement with analytical theory (solid curves).

additional sources of momentum are needed to access plasmons from the external illumination, for example by nanostructuring the film, as we will see below.

3.5.2 Tunable light modulation through UGM ribbon arrays

In order to more efficiently couple incident light to the plasmons in UGMs, we study the effect of patterning it into a periodic array of ribbons. These structures are simulated using a finite element method in the frequency domain (COMSOL), and the numerical results are compared to a simple analytical model, where we approximate the transversal ribbon polarizability per unit length α/L by the contribution of the lowest-order dipolar plasmon, which yields[38] (see Section 2.5)

$$\frac{\alpha}{L} = \frac{0.889\,\epsilon\,W^2}{14.5 - i\omega W\epsilon/\sigma},$$

where W is the ribbon width, ϵ is the permittivity of the homogeneous environment, and the surface conductivity $\sigma = \sigma_{\mathrm{m}} + \sigma_{\mathrm{g}}$ is the sum of metal and graphene contributions. The latter is given by Eq. 1.14, while we calculate the former as

$$\sigma_{\mathrm{m}} = \frac{\mathrm{i}\omega t}{4\pi}(1-\epsilon_{\mathrm{m}}),$$

where t and ϵ_{m} are the thickness and permittivity of the ultrathin metal. We take ϵ_{m} from optical measurements.[28] Under the conditions of Fig. 3.5a, the reflection and transmission coefficients of the array for normal-incidence p-polarized light are[38,77]

$$r_{\mathrm{p}}^{\mathrm{array}} = \frac{-\mathrm{i}S}{(\alpha/L)^{-1} - G},$$
$$t_{\mathrm{p}}^{\mathrm{array}} = 1 - r_{\mathrm{p}}^{\mathrm{array}},$$

where $S = 2\pi\omega/\left(cP\sqrt{\epsilon}\right)$, $G \approx 2\pi^2/\left(3P^2\epsilon\right) + \mathrm{i}S$, and P is the array period.

We consider a graphene-silver ribbon array embedded in silica shown in Fig. 3.5a (ribbon width $W = 50\,\mathrm{nm}$, array period $P = 100\,\mathrm{nm}$, silver thickness $t = 1\,\mathrm{nm}$) and study the extinction $(1-T)$ and reflection of normally-incident light polarized across the ribbons. The resulting spectra have prominent characteristics associated with the lowest-order dipolar mode of the ribbon,[38] corresponding approximately to the condition that the width W is half the plasmon wavelength in the planar film at that energy (*i.e.*, $k_{\parallel} \sim \pi/W$ in Fig. 3.4b). The effect of doping is three-fold: (1) the plasmon peak is blue shifted, (2) the extinction and reflection maxima increase, and (3) the resonance line shape becomes narrower for larger E_{F}. Therefore, an extinction (a reflection) modulation depth of $\sim 26\%$ ($\sim 36\%$) is observed at a photon energy $\sim 0.92\,\mathrm{eV}$ by changing from undoped graphene to $E_{\mathrm{F}} = 1\,\mathrm{eV}$. The effects of doping lead to the suppression of damping channels (interband transitions) at photon energies below $2E_{\mathrm{F}}$. In addition, it is expected that the increase in the number of available free carriers produced by doping will cause the noted blue shift. Remarkably, despite the simplicity of the analytical model (Fig. 3.5b, solid curves), it is in an excellent agreement with the full numerical calculations (dotted curves), except for a small blue shift in the latter. In particular, the relative effect of doping should be the same for both types of simulations.

The tunable modulation of light in reflection and absorption for the class of structures shown in Fig. 3.4a is a robust effect that occurs up to a relatively large metal thickness, as shown in Fig. 3.6. These results clearly show that an increase (decrease) in reflectance (absorbance) occurs when Fermi energy exceeds about half the plasmonic energy for each of the three metal thicknesses considered. At the same time, the plasmonic resonance becomes narrower and slightly blue shifted in all cases. It is important to note that in addition to the width of the ribbon, the thickness of

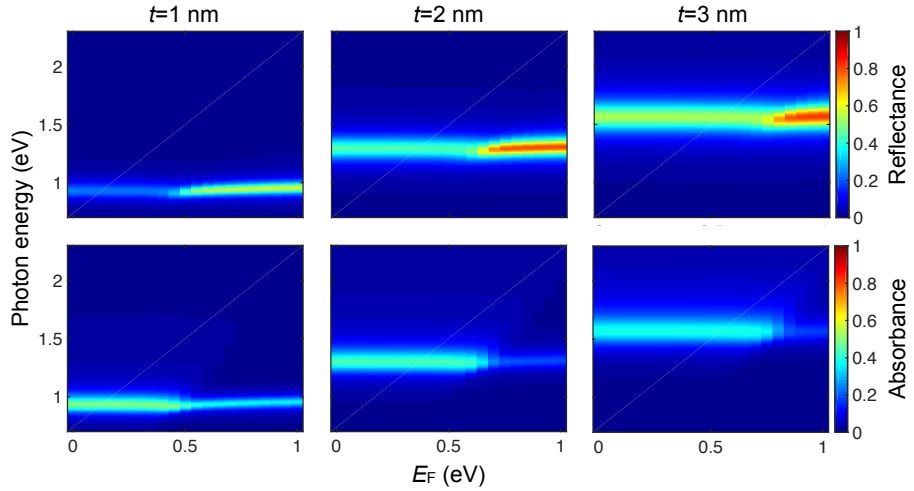

Figure 3.6: **Tunable light modulation through UGM ribbon arrays.** We show the normal-incidence reflectance (top) and absorbance (bottom) analytically calculated for the structure considered in Fig. 3.5a (graphene-silver ribbons in silica, width $W = 50\,\text{nm}$, period $P = 100\,\text{nm}$) with different metal thicknesses $t = 1 - 3\,\text{nm}$ (left to right) as a function of graphene Fermi energy (horizontal axis) and photon energy (vertical axis).

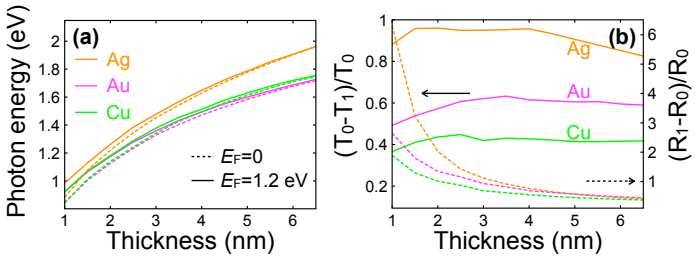

Figure 3.7: **Dependence of light modulation on the choice of metal and metal thickness.** Here we consider a periodic array of metal ribbons ($W = 50\,\text{nm}$, $P = 100\,\text{nm}$) on top of a continuous graphene sheet. (a) Peak extinction energy with highly doped (solid curves) and undoped (dashed curves) graphene as a function of metal thickness for different noble metals. (b) Metal thickness dependence of the modulation depth for transmission (solid curves, left scale) and reflection (dashed curves, right scale), defined in terms of the normal-incidence, p-polarization transmittance and reflectance coefficients for undoped (T_0 and R_0) and doped (T_1 and R_1) graphene, evaluated at the peak photon energy of the doped structure.

the silver offers another degree of freedom to control the plasmon energy. Moreover, the absorbance for $t = 1\,\text{nm}$ and undoped graphene reaches the maximum value of 50%, which is possible for optically thin films.[118] In addition, the modulation depth extracted from these results can be as high as $\sim 23\%$ in absorption and $\sim 59\%$ in reflection.

3.5.3 Dependence of light modulation on the type of metal

Although silver is the least lossy noble metal in the spectral region considered, gold and copper can also do a fairly good job in UGMs. In Fig. 3.7 we present an overview of the plasmon energy corresponding to the maximum extinction as a function of metal thickness for these three different metals. These results are obtained for a periodic array of metal ribbons ($W = 50\,\text{nm}$, $P = 100\,\text{nm}$) on an extended graphene sheet (with and without doping). Plasmon energy increases with the thickness (*i.e.*, when the aspect ratio of the ribbons decreases) and takes similar values for the three metals, as they also have similar conduction electron densities, although silver plasmons are slightly blue shifted because the d-band screening is less efficient in this material. Moreover, as the thickness increases, the structure is less sensitive to doping since graphene has to compete with a comparatively larger metal volume.

The modulation depth (Fig. 3.7b), defined as the relative change in transmission (or reflection) between doped and undoped structures (see vertical axis labels), is an

important parameter to consider potential applications. Obviously, this quantity degrades when the thickness of the metal is large, again because the weight of graphene is comparatively lower, so it is submerged by the metal. Within the small thickness limit, the transmittance increases, which also results in a reduction in the depth of the transmission modulation, while the reflection modulation reaches values well above 1 for all three metals, and approaches ~ 6 for silver. We therefore conclude that optimal modulation in reflection is obtained for the thinnest metallic films, while maintaining reasonable modulation in transmission. Clearly, silver has the best performance among the noble metals for the modulation of vis-NIR light, reaching a depth that exceeds 90% in transmission for metal thicknesses between 1 and 5 nm and >100% in reflection below 3 nm.

3.6 Conclusions

In conclusion, monolayer graphene can be used to produce unity-order changes in the transmission, reflection, and absorption of light down to the vis-NIR domain when comparing its electrically doped and undoped states. It should be emphasized that the calculations here presented for geometries containing only graphene and dielectrics are scalable, so that the main requirement is that the graphene can be switched back and forth between $E_F = 0$ and $E_F > E_\mathrm{p}/2$, where E_p is the photon energy under operation; provided this condition is satisfied, all geometrical lengths and the light wavelength can be scaled by a common factor, leading to the same values for the transmission and absorption. For example, the modulation at 700 nm wavelength predicted in Fig. 3.1 with doping up to $E_F = 1.1$ eV can be also extrapolated to the 1550 nm telecom wavelength with doping up to $E_F = 0.5$ eV after scaling all lengths by a factor of ~ 2.

Interestingly, we find that undecorated graphene in a planar multilayer dielectric structure can modulate transmission near the point of resonant tunneling under total internal reflection, with absolute changes exceeding 90% and an extinction ratio > 15 dB. Similar levels of modulation are found for graphene placed inside a realistic Fabry-Perot cavity. Large vis-NIR modulation depths are also predicted in a graphene layer decorated with periodic arrays of silicon or gold particles. Obviously, the depth of modulation is reduced by coupling to impurities in low-quality graphene, where optical losses can be still significant under high doping. Nonetheless, we find a substantial degree of modulation even in the presence of large residual absorption (*e.g.*, $\sim 50\%$ modulation in the device of Fig. 3.1 when the residual optical loss amounts to 14% of the ideal absorption-free highly doped material).

We also demonstrate that graphene can be used to modulate the optical response of thin metals, taking advantage of both the strong spectral weight of the resulting plasmons in the hybrid structure and the comparatively large volume of the carbon

film when the metal thickness is reduced to only a few nanometers. Graphene doping causes a suppression of interband transitions, and in consequence, a reduction of plasmon damping, which is accompanied by blue shifts due to the addition of doping charges. We find a remarkable $> 90\%$ modulation depth in transmission by using graphene-loaded silver ribbon arrays for metal thicknesses in the $1-5$ nm range and lateral dimensions of tens of nanometers, which are attainable with currently available lithographies. The modulation of reflection is even more dramatic for metal thickness below 3 nm. The plasmon energies cover the 1—1.8 eV photon energy interval for these thicknesses, thus enabling the design of wide-spectral-range devices. Additionally, a continuous graphene layer appears to be advantageous to increase the modulation depth, and thus, only the thin metal film needs to be patterned.

The mechanisms here considered for light modulation by graphene can be integrated into devices spanning only a few square microns in size, so they require a relatively small amount of doping charge to operate. We thus anticipate that these systems will be able to modulate vis-NIR light at high speeds with a minute consumption of power, typical of capacitive devices. This is an advantage with respect to alternative commutation devices based on quantum-wells[119] and phase-change materials.[120] The large electro-optical response of graphene combined with its small volume is thus ideal attributes for the design of fast optical modulators and switches operating in the vis-NIR, which can benefit from the coupling to optical resonators such as those explored in this chapter. These findings open a new avenue for the development of compact electro-optical components such as tunable light filters, switches, and sensors in the vis-NIR spectral region, that are appealing for micro integration and mass production.

4

Nanoscale thermal management with graphene

4.1 Introduction

Heat deposition via light absorption in nanostructures constitutes a useful tool for controlling nanoscale thermal sources,[59,121–123] with potential application in photothermal therapy,[55,124,125] nanoimaging,[126,127] nanocatalysis,[56] data storage,[57] and hot-electron devices.[19,128] Importantly, plasmons in metallic nanostructures enable resonant enhancement of photothermal effects, which can be manipulated down to the nanometer scale.[59,121] Recently, highly doped graphene has emerged as an outstanding two-dimensional material capable of supporting extremely confined surface plasmons that can be actively tuned by varying its Fermi energy through electrical gating and chemical doping, with application in optical modulation,[78,118,129,130] light detection,[41,42,131–133] and sensing.[134–136] Additionally, the photothermal response of graphene is particularly appealing because of the combination of the following three properties: (i) the low number of electrons needed to sustain plasmons in this material compared with conventional three-dimensional metallic structures; (ii) its low electronic heat capacity; and (iii) the strong variation of its optical response produced by electronic heating. Properties (i) and (ii) lead to unusually high electron temperatures under resonant pumping conditions,[38–40] while properties (ii) and (iii), which originate in the conical electronic bands of graphene,[38] give rise to an extraordinary photothermal response.

On the other hand, energy dissipation in nanoscale devices produces heat accumulation that can result in structural damage and poor performance. Understandably, heat management constitutes an important aspect when designing thermoelectric,[137] optoelectronic,[138] electromechanical,[139] and photovoltaic[140] elements. However, the relatively slow thermal conduction in most materials[141] imposes a serious limitation. Finding new means of cooling nanostructures is therefore critical. An interesting possibility is provided by coupling to radiative degrees of freedom. Indeed, the absorption and emission of radiation by a material structure contributes to reach thermal equilibrium with other surrounding structures and the electromagnetic environment. This is the dominant cooling channel for thermally isolated (non-contact) structures,[142] in which energy is released through the emission of photons with wavelengths $\sim \lambda_T = \sim 2\pi\hbar c/k_B T$ (*i.e.*, the thermal wavelength at temperature T). When the structures are separated by vacuum gaps of large size compared with λ_T, the Planck and Kirchhoff laws determine the exchanged power.[143] In contrast, for neighboring objects separated by a small distance compared with λ_T, radiative heat transfer is dominated by evanescent waves.[65–67] As these waves are incapable of propagating energy, their associated transfer rates can exceed the black-body limit by several orders of magnitude, enhanced by the near-field coupling of resonances supported by the nanostructures, thus emerging as a potentially relevant transfer mechanism in solid state devices.

In the first part of this chapter, we exploit the extraordinary optical and thermal properties of graphene to show that ultrafast radiative heat transfer can take place between neighboring nanoislands. The commonly accepted scheme for dissipation of the thermal energy produced by electronic and optical inelastic losses (*i.e.*, energy transfer to valence and conduction electrons of the system, followed by relaxation into phonons and subsequent heat flow into the surrounding media) is here challenged by the radiative transfer mechanism taking place between neighboring structures within femtosecond timescales, thus overcoming electron relaxation into the atomic lattice. Using attainable graphene nanostructure designs, we find that ultrafast radiative heat transfer produces thermalization of two neighboring islands that results in >50% of the electronic heat of the hot one being radiatively transferred to its colder neighbor. This extraordinary phenomenon is made possible by the large plasmonic field concentration that mediates the coupling between the neighboring graphene structures, as well as by the low specific electronic heat of this material[38] (see Section 1.4.2).

In the second part of this chapter, we investigate the photothermally induced optical response of graphene and reveal a radically different behavior (different strength of electron-phonon coupling) in clean and disordered layers leading to unprecedented plasmonic behavior. More precisely, we account in a self-consistent manner for the interplay between optical absorption, heat dissipation, and spatial modification of the electron temperature and optical conductivity under optical pumping, and find that weak electron-phonon coupling in clean graphene results in high electron temperatures, while the lattice stays near the ambient level. We exploit this effect to predict (i) a dramatic photothermal modulation of plasmons in graphene ribbons and (ii) the existence of plasmons that couple efficiently to external light in homogeneous extended graphene by photothermally patterning a periodic modulation of the optical response.

4.2 Non-contact thermal management

In the nanoscale, when the separation distance between two structures is smaller than $\sim 2\pi\hbar c/k_B T$, non-contact radiative cooling can have huge impacts in many nanoscale systems, even become a dominant heat dissipation channel while other channels are inactivated. In this section, we present an interesting scenario: we enter a regime where radiative heat transfer becomes ultrafast in a system composed of two graphene disks.

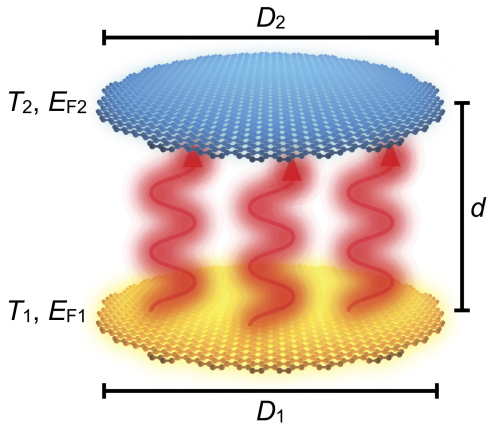

Figure 4.1: **Sketch of the structure considered for ultrafast radiative heat transfer.** We study heat transfer between two parallel coaxial graphene disks placed in vacuum and separated by a small distance d. Each disk $\ell = 1, 2$ is characterized by its diameter D_ℓ, Fermi energy $E_{F\ell}$, and electron temperature T_ℓ, with $T_1 > T_2$.

4.2.1 Radiative heat transfer between graphene nanodisks

We focus on the system depicted in Fig. 4.1, consisting of two parallel coaxial graphene nanodisks of diameters D_1 and D_2, separated by a distance d between carbon planes, doped to Fermi levels E_{F1} and E_{F2}, and having electronic temperatures $T_1 > T_2$. For simplicity, we consider the disks to be placed in vacuum. Heat is radiatively transferred from the hotter disk to the colder one as a result of thermal fluctuations in both disks, whose interaction is mediated by their self-consistent electromagnetic response. In fact, for the small size of the structures under consideration compared with the thermal wavelengths λ_{T_ℓ} (with $\ell = 1, 2$), retardation and magnetic response effects can be dismissed, so we only need to deal with charge fluctuations and their Coulomb interaction.

We calculate the heat transfer power (HTP) as the net balance of the work done by the thermally fluctuating charges of the hotter disk on the colder one minus the work done on the former by the fluctuating charges of the latter. This leads to a classical electromagnetic expression involving thermal fluctuations, which are evaluated by means of the fluctuation-dissipation theorem.[71,72] A detailed description has been offered in Section 1.4.3, leading to a compact expression (Eq. 1.61) that is proportional to the integral over the exchanged frequency ω. The integrand consists of the difference between the Bose-Einstein occupation numbers $n_\ell = [\exp(\hbar\omega/k_B T_\ell) - 1]^{-1}$ of

the two disks at their respective temperatures T_ℓ, multiplied by a *loss* function that is determined by the disk susceptibilities χ_ℓ. The latter are dominated by plasmonic modes, which allow us to formulate a description in terms of plasmon wave functions (PWFs)[99,100] (see also Section 1.2.2). Only the lowest-order PWFs contribute significantly to the HTP for the range of geometrical parameters under consideration. Their explicit form, as well as full details on the PWF-based susceptibilities, are given in Appendix D. For coaxial disks (Fig. 4.1), we find that modes of different azimuthal number m do not mix, so we can separate their contributions to the HTP received by disk 2 as

$$P_2 = \frac{2\hbar}{\pi}\sum_{m=0}^{\infty}(2-\delta_{m0})\int_0^\infty \omega\, d\omega\,(n_1-n_2)\,\mathrm{Tr}\left[\Delta^{m\dagger}\cdot v^m\cdot \mathrm{Im}\{\chi_1^m\}\cdot v^m\cdot\Delta^m\cdot\mathrm{Im}\{\chi_2^m\}\right] \tag{4.1}$$

(and also $P_1=-P_2$), where Tr[...] stands for the trace, the matrix $\Delta^m=(\mathscr{I}-\chi_2^m\cdot v^m\cdot\chi_1^m\cdot v^m)^{-1}$ accounts for multiple scattering between the disks, v^m describes their mutual Coulomb interaction, and $\mathscr{I}$ is a unit matrix. The matrices v^m and χ_ℓ^m contain elements projected on the PWFs with m azimuthal symmetry (see Appendix D for detailed expressions). Incidentally, the leading $(2-\delta_{m0})$ factor reflects the fact that m and $-m$ modes yield the same contribution.

In this formalism, the optical response of graphene is described through its surface conductivity σ, for which we adopt the local-RPA model[38,144,145] (see Eq. 1.14 in Section 1.1.5). We remark that besides the explicit dependence of n_ℓ on T_ℓ, the temperature enters σ through the chemical potential as well (see Eq. 1.16).

Incidentally, as the HTP of Eq. 4.1 is an integrated quantity, it is not too sensitive to the model used for the graphene conductivity σ. The small d region is most sensitive to elements of the formalism such as the inclusion of multiple scattering in the optical response of the disks (Δ^m matrices in Eq. 4.1). Here, we assume $\hbar\tau^{-1}=10\,\mathrm{meV}$ throughout this section. We stress that the relatively high temperatures under consideration (thousands of degrees) refer to the electronic gas of the material, which can be reached by optical pumping in the ultrafast regime.[146]

The disk separation dependence of the HTP is studied in Fig. 4.2a (solid curves) for 20 nm graphene disks doped to a Fermi level $E_\mathrm{F}=0.2\,\mathrm{eV}$, with the hotter disk at different temperatures T_1 (see labels) and the colder one at room temperature $T_2=300\,\mathrm{K}$. In general, higher temperatures T_1 lead to larger HTP, due in part to the (n_1-n_2) factor in Eq. 4.1. At large separations $d\gg D_\ell$, only dipole-dipole interactions between the disks contribute efficiently to the transfer, leading to a $1/d^6$ dependence, in agreement with the asymptotic expression of Eq. 1.62.

As a reference, we compare these results with the HTP for gold disks of the same diameter (Fig. 4.2a, broken curves), which we describe through an effective surface

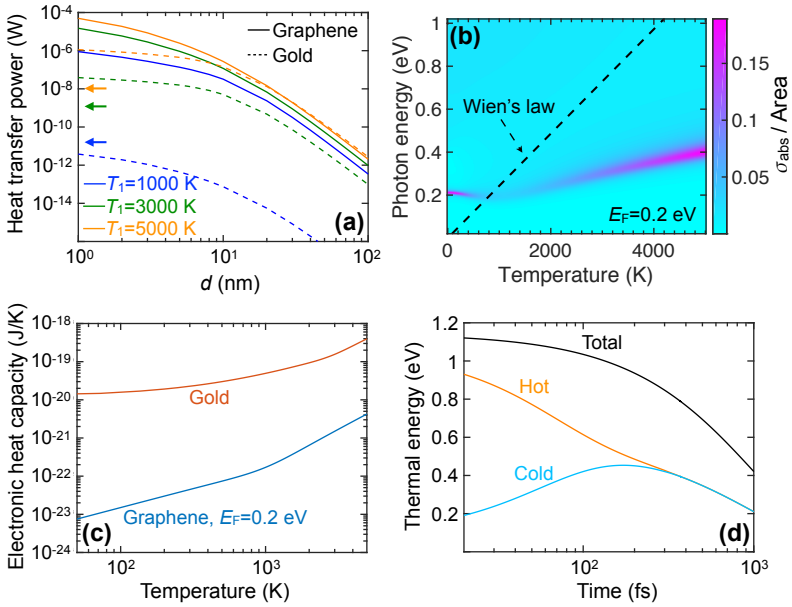

Figure 4.2: **Thermal and optical properties associated with radiative heat transfer.** (a) Dependence of the radiative heat transfer power (HTP) on the separation distance d between two graphene nanodisks (solid curves) compared with two gold nanodisks (dashed curves, disk thickness $t = 2\,\text{nm}$). The HTP is plotted for different values of T_1 (see legend), while the cold disk is at ambient temperature $T_2 = 300\,\text{K}$. The arrows indicate the HTP between two blackbodies (at temperatures T_1 and T_2, respectively) of an area equal to that of the present disks. (b) Optical absorption cross-section σ_{abs} normalized to the graphene area for one of the graphene disks considered in (a) as a function of photon energy $\hbar\omega$ and temperature T. The dashed line corresponds to Wien's law, $\hbar\omega \approx 2.82\,k_B T$. (c) Temperature dependence of the electronic heat capacity for one of the graphene (blue curve) and gold (red curve, taken from Ref. [147]) nanodisks considered in (a). (d) Illustrative example of the femtosecond dynamics of the electronic thermal energy in two graphene nanodisks under the conditions of (a), with initial temperatures $T_1 = 1000\,\text{K}$ and $T_2 = 300\,\text{K}$. The electronic thermal energy is shown for both the initially hot (orange curve) and cold (cyan curve) nanodisks, as well as their sum (black curve).

conductivity obtained from the measured dielectric function[28] ϵ_{Au} as $\sigma_{\mathrm{Au}} = \mathrm{i}\omega t(1-\epsilon_{\mathrm{Au}})/4\pi$, where we take a thickness $t = 2\,\mathrm{nm}$. This approximation, which is reasonable because we are considering a small value of t compared with the diameter (20 nm), allows us to apply the same formalism as for graphene (Eq. 4.1). Despite the larger thickness of the gold disks, their HTP is much smaller than for graphene. In fact, plasmons in the graphene disks lie in the mid-infrared region for the parameters under consideration (*i.e.*, their energies are commensurate with $k_{\mathrm{B}}T_1$), while those of the gold disks appear at much higher energies, and thus do not contribute efficiently to the heat transfer. This mismatch is partly alleviated at the highest temperature under consideration ($T_1 = 5000\,\mathrm{K}$), for which gold and graphene disks exhibit similar HTPs in the large d limit.

As an additional comparison, the left arrows in Fig. 4.2(a) show an estimate obtained from the Stefan-Boltzmann law[148] for radiative heat transfer between two blackbodies of an area equal to that of the present disks. As anticipated above, graphene outperforms blackbodies by several orders of magnitude.

The strength of their optical response influences the ability of the disks to transfer energy radiatively. This is examined in Fig. 4.2b, where we plot the absorption cross-section of one of the graphene disks considered in Fig. 4.2a. An intense plasmon feature is observed in the 0.2-0.4 eV region, whose temperature dependence is inherited from the conductivity (Eq. 1.14). The dashed line in Fig. 4.2b shows the relation between the temperature and the photon energy according to Wien's law (*i.e.*, the value of $\hbar\omega$ at the maximum of $\omega^3 n_\ell(\omega)$ as a function of T_ℓ). This is relevant for the analysis of Eq. 4.1, in which a factor $\omega\, n_\ell(\omega)$ appears explicitly, whereas the remaining ω^2 factor comes from the low ω limit of the $\mathrm{Im}\{\chi_\ell^m\}$ matrices. Additionally, the response functions entering the trace in Eq. 4.1 display maxima near the plasmons, and therefore, the overlap between the dashed line and the plasmon in Fig. 4.2b indicates that this excitation contributes efficiently to the HTP.

The electronic heat capacity provides a relation between the temperature and the amount of energy stored in the electron gas. In this respect, graphene is also advantageous relative to traditional plasmonic materials such as gold because its heat capacity is orders of magnitude smaller (Fig. 4.2c) as a result of its conical band structure, in contrast to the parabolic dispersion of gold conduction electrons. In consequence, cooling the graphene electrons requires transferring a smaller amount of heat, thus making the process potentially faster.

4.2.2 Ultrafast radiative heat transfer regime

We study the heat transfer dynamics by considering the electronic heat Q_ℓ deposited on each graphene disk ℓ and the evolution of these quantities according to the equations

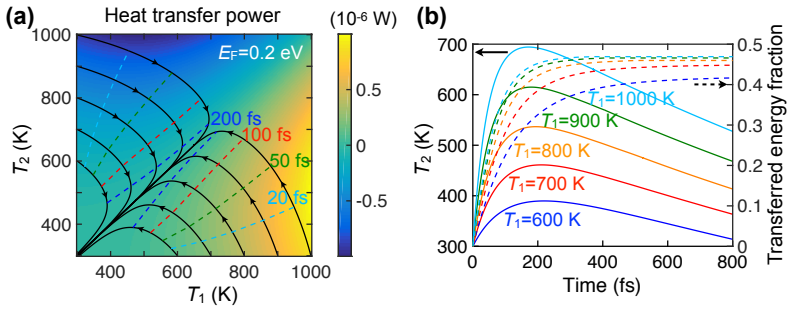

Figure 4.3: **Temperature and temporal dependences of radiative heat transfer.** (a) HTP between two graphene nanodisks (20 nm diameter, 0.2 eV Fermi energy, $d = 1$ nm separation) as a function of T_1 and T_2 for the geometry of Fig. 4.1. Solid black curves represent the evolution of the electron temperatures in the two nanodisks for different initial conditions. Dashed curves indicate the times (see labels) along the evolution of the solid curves from either the vertical or the horizontal axes of the plot. We assume an inelastic relaxation time (electron-lattice coupling) of 1 ps . (b) Temporal evolution of the electron temperature T_2 in the colder disk (initially at $T_2 = 300$ K, left vertical scale, solid curves) and the transferred energy fraction from disk 1 to disk 2 (right vertical scale, dashed curves) for different initial electron temperatures of the hotter disk T_1 (see labels).

$$\dot{Q}_1 = -\tau_{\rm ph}^{-1} Q_1 + P_1, \tag{4.2a}$$

$$\dot{Q}_2 = -\tau_{\rm ph}^{-1} Q_2 + P_2, \tag{4.2b}$$

where P_ℓ are the transfer powers given by Eq. 4.1, while $\tau_{\rm ph}$ is a phenomenological electron relaxation time (to phonons) that we approximate as 1 ps, a value of the order of what is observed in pump-probe experiments.[149,150]

As an illustrative example, we show in Fig. 4.2d the evolution of Q_ℓ according to Eqs. 4.2 for the two graphene disks considered in Fig. 4.2a when they are prepared at initial temperatures $T_1 = 1000$ K and $T_1 = 300$ K: the cold disk more than doubles its electronic energy after ~ 200 fs of evolution (peak of cyan curve), when it has gained nearly the same amount of energy as the one dissipated to the atomic lattice (decay of black curve). Notably, the disks reach mutual thermal equilibrium after only ~ 250 fs, well before full relaxation takes place.

A more detailed study of the heat transfer dynamics is presented in Fig. 4.3 for 20 nm graphene disks separated a distance of 1 nm and doped to a Fermi energy of 0.2 eV. The color plot of Fig. 4.3a shows the HTP as a function of the temperatures in the two

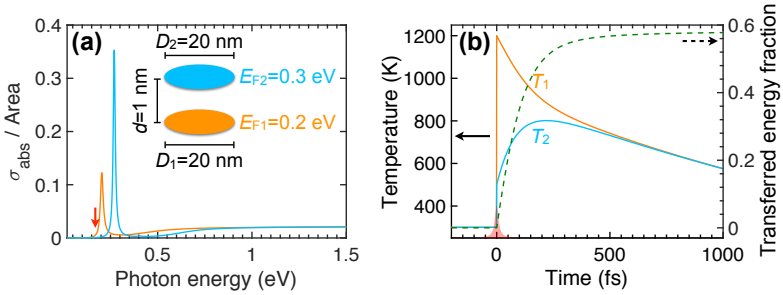

Figure 4.4: **Ultrafast radiative heat transfer induced by optical pumping.** (a) Normalized absorption cross-sections σ_{abs} of two graphene nanodisks (20 nm diameter, $d = 1$ nm separation) at the same initial temperature of 300 K but doped with different Fermi energies (see inset). (b) Time evolution of the electron temperatures T_1 and T_2 (left vertical scale, solid curves) and transferred energy fraction (right vertical scale, dashed curve) after optical pumping (150 mJ/m^2 light fluence, 0.17 eV photon energy, as indicated by the red arrow of (a)).

disks. Obviously, the diagonal of this plot corresponds to zero transfer, when the two particles have the same temperature. The solid black curves represent the evolution of the disk temperatures starting from initial conditions at the plot axes (*i.e.*, with one of the disks at 300 K and the other one at higher temperatures). The evolution is along the direction of the arrows, with positions at specific times indicated by the dashed curves. Interestingly, the evolution toward the diagonal (thermal equilibrium) is characterized by a significant increase in the temperature of the colder disk ($\Delta T \sim 400$ K) within the first 100-200 fs, much faster than relaxation to the atomic lattice. This evolution involves the transfer of a large fraction of electronic heat to the colder disk, as shown in Fig. 4.3b: when the disks are prepared at 1000 K and 300 K initial temperatures, nearly 50% of the electronic heat of the hot disk is transferred to the cold one within the first ~ 200 fs.

In practical implementations, optical pumping with femtosecond laser pulses grants us access into the ultrafast regime, allowing us to reach high electron temperatures such as those considered in this section.[151–153] Additionally, the amount of optically absorbed energy depends on the pump frequency relative to the plasmons of the system.[154] This idea can be exploited to pump neighboring graphene disks in such a way that one of them absorbs much more energy than the other, just by tuning the pump laser near the plasmon of one of the disks and away from the plasmons of the other disk. We thus need disks of either different diameters or different Fermi levels. We consider the latter possibility, which can be realized in practice through the variation in intrinsic doping produced by an asymmetric dielectric environment,

or also by creating different potential landscapes through an asymmetric doping geometry. The system under investigation is depicted in the inset of Fig. 4.4a: two 20 nm graphene disks, separated by 1 nm, initially placed at 300 K, and doped to Fermi energies 0.2 eV and 0.3 eV, respectively. We consider optical pumping at a photon energy of 0.17 eV with a fluence of 150 mJ/m^2. The pulse energy is closer to the lower doping disk (Fig. 4.4a), and thus, this is the one that reaches a higher temperature. For simplicity, we assume instantaneous pumping (*i.e.*, a δ-function temporal profile of the pulse), which rapidly elevates the electron temperatures to $T_1 \sim 1200$ K and $T_2 \sim 500$ K (Fig. 4.4b, left end). Ultrafast radiative heat transfer is again observed, leading to mutual equilibrium between the disks ($T_1 \approx T_2$) within ~ 500 fs, which is accompanied by nearly 60% of the electronic heat of disk 1 being transferred to disk 2. We remark that higher than 50% transferred energy fraction is made possible by the doping asymmetry, which directly affects the heat capacity (see Fig. 1.5 in Section 1.4.2).

4.3 Photothermal manipulation of plasmons in graphene

In the last section, we explore an interesting phenomenon in the regime of non-contact heat transfer. In this section, we step to heat conduction in the electron/phonon subsystems of graphene using a two-temperature model (see Section 1.4.2) under optical pumping. More precisely, we account in a self-consistent manner for the interplay between light absorption and heat conduction, and find that weak electron-phonon coupling in clean graphene results in high electron temperatures.

4.3.1 Plasmon enhanced photothermal effect in a graphene ribbon

Here, we also adopt the local random-phase approximation (local-RPA) to describe the temperature-dependent optical conductivity of graphene $\sigma(\omega)$, combined with a two-temperature model,[64] as presented in Section 1.4.2, to characterize the position-dependent electron and lattice temperatures (T_e and T_l) under CW illumination in the steady-state regime of heat dissipation. The model incorporates the 2D in-plane thermal electron and lattice conductivities (κ_e and κ_l, obtained from their bulk counterparts by multiplying by the graphene thickness $t = 0.33$ nm) to self-consistently calculate the spatial temperature distributions, which are imprinted on the optical conductivity σ through its dependence on T_e.[38,40,145,155] Electron-phonon coupling (*i.e.*, $H(T_e, T_l)$ in Eqs. 1.52 and 1.53) is accounted for by a power-density coupling $g(T_e - T_l)$ for clean graphene and $A\left(T_e^3 - T_l^3\right)$ for disordered graphene,[156–160] where g and A are material-quality-dependent constant coefficients. Additionally, we phenomenologically introduce thermal coupling from the graphene lattice to

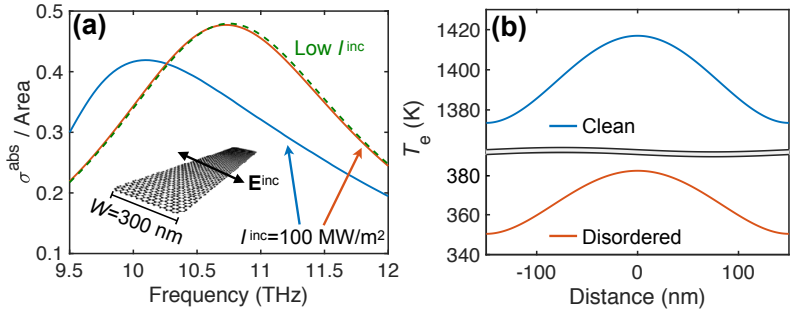

Figure 4.5: **Plasmon photothermal effect in a graphene ribbon.** (a) Normalized normal-incidence absorption cross-section spectra at the spectral peak for a nanoribbon (width $W = 300\,\mathrm{nm}$, $E_\mathrm{F} = 0.4\,\mathrm{eV}$, $g = 3.84 \times 10^4\,\mathrm{W/m^2K}$, embedded in $\epsilon_\mathrm{h} = 4.4$) made of either clean or disordered graphene (solid curves), based on a self-consistent description of heat dissipation for an incident light intensity $I^\mathrm{inc} = 100\,\mathrm{MW/m^2}$. (b) Variation of the electron temperature across the ribbon for clean and disordered graphene. We find the lattice temperature to be close to the assumed ambient value of 300 K. Clean graphene reaches higher electron temperature than disordered graphene because it has a much weaker electron-photon coupling.

the substrate (*i.e.*, $B(T_\mathrm{e}, T_\mathrm{l})$ in Eq. 1.53) through a term $G(T_\mathrm{l} - T_0)$, where G is a thermal boundary conductance and T_0 is the ambient temperature. In our simulations, we take $T_0 = 300\,\mathrm{K}$ and assume parameter values consistent with reported measurements: $g \sim 10^4\,\mathrm{W/m^2K}$, $A = 2.24\,\mathrm{W/m^2K^3}$, and $G = 5\,\mathrm{MW/m^2K}$;[161–163] $\kappa_\mathrm{l}/t = 100\,\mathrm{W/mK}$;[164,165] and $\kappa_\mathrm{e} = 0.1\kappa_\mathrm{l}$.[166] Specific values for the Fermi energy E_F and the E_F-dependent coefficient g are given in the figure captions. Regarding optical damping, we assume a conservative inelastic scattering time $\tau = 66\,\mathrm{fs}$ ($\hbar\tau^{-1} = 10\,\mathrm{meV}$) in both clean and disordered graphene in this section. We use a finite element method for the latter and iterate the electromagnetic and thermal solutions until self-consistency is achieved typically after ~ 10 iterations. We consider graphene either supported or embedded in an isotropic dielectric of permittivity $\epsilon_\mathrm{h} = 4.4$.

We first study a graphene ribbon (width $W = 300\,\mathrm{nm}$) under normal-incidence illumination with transversal polarization (inset to Fig. 4.5a). A prominent plasmon is observed in the absorption spectrum of Fig. 4.5a for low light intensity (dashed curve). The spectrum remains nearly unchanged at a high intensity ($I^\mathrm{inc} = 100\,\mathrm{MW/m^2}$) in disordered graphene (solid red curve), whereas the plasmon peak undergoes a $\sim 10\%$ redshift in clean graphene (solid blue curve). We attribute this different behavior to the much weaker electron-phonon coupling in clean graphene,[160] which leads to an

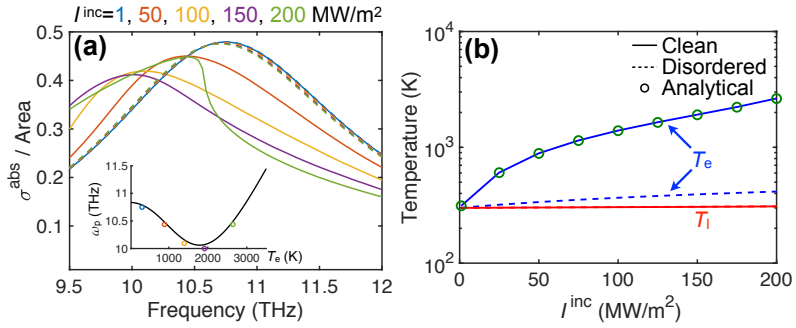

Figure 4.6: **Light-intensity dependence of the plasmon photothermal effect.** (a) Absorption spectra of the graphene nanoribbon considered in Fig. 4.5 for a wide selection of light intensities. The spectra are dominated by the lowest-order transverse plasmon, the frequency of which is shown in the inset as a function of electron temperature. (b) Space-averaged temperatures (lattice T_l and electrons T_e) as a function of light intensity at the absorption peak frequencies of (a). We present results for both clean (solid curves) and disordered (dashed curves) graphene.

elevated electron temperature $T_e \sim 1400\,\mathrm{K}$, in stark contrast to the mild increase in T_e for disorder graphene, as shown in Fig. 4.5b.

When varying the incident light intensity in the I^{inc} =1-100 $\mathrm{MW/m^2}$ range, we find a systematic redshift and broadening of the absorption peak in the clean graphene ribbon (Fig. 4.6). Further increase in intensity up to 200 $\mathrm{MW/m^2}$ produces a large distortion in the absorption spectrum, resulting from the non-monotonic temperature dependence of both the graphene conductivity and the resulting transverse ribbon plasmon energy. The latter admits the analytical expression[38] $\hbar\omega_p = (e/\sqrt{-\pi\eta_1\epsilon_h})\sqrt{\mu^D/W}$ (see Eq. 2.11), where $\eta_1 = -0.0687$ is an eigenvalue corresponding to the lowest-order dipolar transverse plasmon, while $\mu^D = \mu + 2k_B T_e \log\left(1 + e^{-\mu/k_B T_e}\right)$ and $\mu = E_F\left[\left(1+\xi^4\right)^{1/2} - \xi^2\right]^{1/2}$, with $\xi = (2\log^2 4)(k_B T_e/E_F)^2$, are the temperature-corrected Drude weight and chemical potential, respectively[40] (see Eqs. 1.15 and 1.16). This expression (solid curve in the inset to Fig. 4.6a) is in excellent agreement with the computed spectral peaks (symbols) when using the calculated spaced-averaged values of T_e as input. Note that the non-monotonic temperature dependence of the spectral peaks is solely inherited from the temperature dependence of the Drude weight (see explicit expression above), which undergoes a reduction (increase) with increasing temperature when $k_B T_e \ll \mu$ ($k_B T_e \gg \mu$).[40]

Remarkably, under these attainable conditions, the electrons reach a temperature above 2500 K in clean graphene, while the lattice remains near the ambient level

(Fig. 4.6b). We stress again that this is in stark contrast to disordered graphene, for which the spectra remain nearly unchanged within the considered intensity range and the electron temperature hardly exceeds 400 K (Fig. 4.6b) due to a more efficient electron-phonon coupling.

We obtain further insight into the photothermal response of clean graphene by adopting the reasonable assumption $T_l \approx T_0$, which effectively decouples the lattice from the electronic system, so that heat dissipation is fully described through

$$\nabla \cdot \kappa_e \nabla (T_e - T_0) - g(T_e - T_0) \approx -p^{abs}, \tag{4.3}$$

where p^{abs} is the power density of optical absorption. Further assuming a constant value of κ_e, this equation allows us to obtain a characteristic electronic-heat-diffusion distance $D_e = \sqrt{\kappa_e / g}$. Indeed, a measure of the degree of heat localization is provided by the electron temperature profile produced by a line heat source, $T_e(x) \propto e^{-|x|/D_e}$, as a function of distance x to it. Under the conditions of Figs. 4.5 and 4.6, we have $D_e \approx 293\,\text{nm} \sim W$, which explains why T_e is nearly uniform across the ribbon, unlike the cosine-like p^{abs} transversal profile associated with the dipolar plasmon under consideration. The uniformity of T_e now allows us to write the analytical estimate $T_e = T_0 + I^{inc}(\sigma^{abs}/\text{Area})/g$ for clean graphene, represented in Fig. 4.6b (symbols, with σ^{abs}/Area taken at the peak frequencies of Fig. 4.6a), in excellent agreement with full numerical simulations (solid blue curve).

4.3.2 Photothermal patterning of extended graphene

Plasmon confinement in graphene has so far been achieved through lateral patterning (*e.g.*, in ribbons[78,130]), inhomogeneous doping,[167] or nanostructured dielectric environments.[168] These approaches require the use of nanolithography, which is generally detrimental for the graphene quality. Motivated by the above study for graphene ribbons, we explore next a radically different method for producing and actively tuning plasmon confinement in extended, unpatterned graphene that does not require nanostructuring: spatially modulated optical heating can be applied by projecting an on-demand pump pattern, thus configuring an inhomogeneous graphene optical response capable of trapping plasmons and molding their spatial profiles with a resolution limited by far-field diffraction to roughly half the pump wavelength $\lambda_{pump}/2$.

We demonstrate the feasibility of this concept by considering an extended clean graphene sheet ($E_F = 0.3\,\text{eV}$ doping, supported on a substrate ϵ_h), on which a pump *light grating* is formed by interfering two coherent *s*-polarized CW plane waves ($\lambda_{pump} = 785\,\text{nm}$, intensity $I_{pump} = 5 - 160\,\text{GW/m}^2$ each, incidence angles $\pm\theta = \pm 5.6°$). The in-plane electric-field pump intensity is then $4I_{pump}\cos^2\left[2\pi \sin\theta (x/\lambda_{pump})\right]$, where we take the beam directions to lie on the plane formed by the surface normal and the

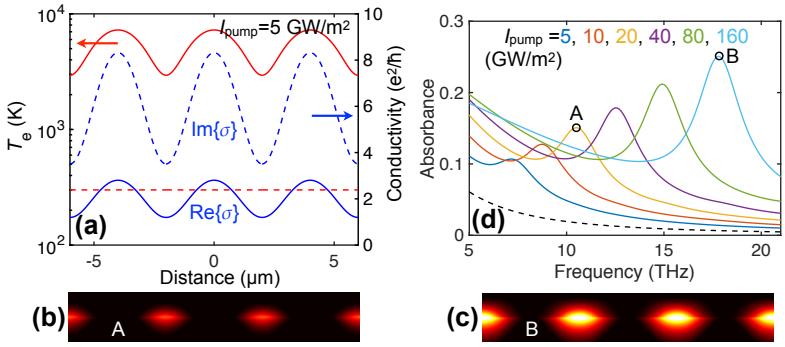

Figure 4.7: **Photothermal patterning of a homogeneous graphene sheet.** We consider an extended doped clean graphene sheet ($E_F = 0.3\,\text{eV}$, $g = 1.21 \times 10^4\,\text{W/m}^2\text{K}$, substrate $\epsilon_h = 4.4$) exposed to a light intensity grating of $4\,\mu$m period, formed by the interference of two CW 785 nm pump plane waves of equal intensity (I_{pump} each). (a) Spatial variation of the self-consistent electron temperature produced by the pump with $I_{pump} = 5\,\text{GW/m}^2$ (solid red curve, left scale) and resulting optical conductivity (blue curves, right scale) at a probing frequency of 7.2 THz. The ambient temperature level (300 K) is shown for reference (broken red line). (b,c) Near-field intensity plots in a plane transversal to the graphene at the peak plasmon frequencies shown in (d) for $I_{pump} = 20\,\text{GW/m}^2$ (A) and $160\,\text{GW/m}^2$ (B). (d) Absorption spectra probed in the THz region with (solid curves) and without (dashed curve) light grating pumping for various values of I_{pump}.

in-plane x axis. Incidentally, we obtain a graphene absorbance $(4\pi\mathrm{Re}\{\sigma\}/c)|t_s|^2 \sim 0.002-0.008$ from the local-RPA conductivity σ, with $t_s \approx 2/(1+\sqrt{\epsilon_h})$. This result deviates from the $T_e = 0$ behavior[103,104] $\approx 0.023\, t_s^2$: thermal smearing of graphene interband transitions causes a reduction in the absorption of visible light over the range of I_{pump} under consideration. The resulting self-consistent electron temperature T_e reaches high values ($\sim 7200\,\mathrm{K}$ for $5\,\mathrm{GW/m^2}$) and displays a periodic pattern with a max-to-min contrast ratio ~ 2.5 (Fig. 4.7a). This imparts a periodic pattern on the optical conductivity, effectively transforming the optical response of the extended graphene layer into that of a graphene ribbon array, which can be also regarded as a thermally imprinted grating. When examining the absorption spectra as a function of probe frequency in the THz region (Fig. 4.7d, for normal incidence and probe polarization across the ribbons), a prominent resonance peak is observed, shifting up in frequency as the pump intensity is increased. Interestingly, the resonant near-field probe intensity distribution, shown in Fig. 4.7, reveals plasmon confinement in the minima of T_e regions, where $\mathrm{Re}\{\sigma\}$ reaches a minimum (*i.e.*, low inelastic losses), while $\mathrm{Im}\{\sigma\}$ is also minimum and configures an effective plasmon potential well. The depth of such potential well can be estimated through $\max(\mathrm{Im}\{\sigma\})/\min(\mathrm{Im}\{\sigma\})$, a larger value of which indicates a more confining well. Also, the quality factor of the resonance $[\sim \mathrm{Im}\{\sigma\}/\mathrm{Re}\{\sigma\}]$ increases when raising the pump intensity, as observed in Fig. 4.7d.

4.4 Conclusions

In the first part of this chapter, our prediction of ultrafast radiative heat transfer in graphene provides a fundamentally unique scenario: radiative coupling is capable of evacuating electronic heat from a nanoisland to a surrounding structure fast enough to prevent substantial relaxation into the atomic lattice. This is accomplished with attainable geometrical and material parameters: tens of nanometers in lateral size D in structures that can be patterned through state-of-the-art lithography[134,169] and bottom-up synthesis;[170–172] tenths of electronvolts Fermi energy E_F, controllable through electrical gating;[105,106] and electron temperatures T of thousands of degrees reached by ultrafast optical pumping.[146,173]

Our choice of parameters leads to graphene plasmon energies that are commensurate with $k_B T$ (*i.e.*, they overlap the broad spectral peak of thermal emission). As a consequence, the characteristic time interval τ_{RHT} required to radiatively transfer a sizable fraction of the electronic heat energy is reduced to the femtosecond domain. A simple dimensional analysis reveals that the HTP is proportional to E_F/D, provided the ratios of disk diameters and temperatures, as well as d/D and the quantity E_F/DT^2, are kept constant. The optimum temperature at which maximum transfer takes place scales as $T \propto \sqrt{E_F/D}$. Additionally, we find the scaling $\tau_{RHT} \propto E_F D^3$ with Fermi

energy and lateral size, and therefore, low doping levels and small sizes enable faster cooling.

An interesting possibility consists in combining more than two structures. This could be used to accelerate the rate of heat evacuation and achieve greater control over the spatial flow of radiative heat transfer. Higher transfer rates could be also obtained through lateral shape optimization or by relying on other carbon allotropes such as carbon nanotubes. Additionally, similar fast transfers should be enabled by a wide range of existing atomic-scale materials capable of sustaining confined optical excitations[174] (*e.g.*, exciton polaritons in dichalcogenides). Besides the fundamental interest of this line of research, electronic cooling via radiative heat transfer constitutes a promising avenue to effectively suppress relaxation to the atomic lattice, thus preventing thermal damage in nanoscale devices. Also note that the ultrafast radiative heat transfer phenomenon here investigated can be actively switched on and off by gating the graphene structures.

In the second part of this chapter, we have shown that the characteristic weak electron-phonon coupling in clean graphene allows us to reach high electron temperatures well above the lattice temperature, which in turn stays near ambient levels under CW illumination conditions. This produces strong photothermal modulation in the graphene optical response, which we exploit to predict large plasmon shifts in ribbons. We further postulate this effect as an efficient way of dynamically imprinting a spatial modulation of the optical response in extended homogeneous graphene, whereby a spatially patterned optical pump is used to locally heat graphene electrons, thus tailoring an on-demand nanoscale response. We illustrate this concept by showing resonant absorption in a photothermally imprinted grating, whose plasmons can couple to far-field radiation, unlike those of homogenous graphene. Besides circumventing the requirement of nanostructuring, this approach can potentially enable fast plasmon modulation relying on the ability to shape the light pumping beams. Our findings are crucial for the design of nanoscale photothermal sources based on graphene.

5

Light detection with graphene

5.1 Introduction

As discussed in previous chapters, graphene has recently emerged as an excellent plasmonic material, which combines large field confinement and enhancement[175] with relatively low losses[46] and the ability to tune the plasmons electrically[41–45,74,75,77,78] or magnetically.[76] In particular, electrical doping using gates can change the Fermi energy of the carbon layer by as much as $E_F \sim 1\,\text{eV}$ from its undoped state,[106] thus opening a $2E_F$ optical gap and effectively sustaining well-behaved plasmons up to energies $\sim E_F$. A unique characteristic of plasmons in this material is that they are sustained by a comparatively small number of electrons.[38] We thus expect that the excitation of a plasmon in a graphene nanostructure will significantly modify the population of the electronic levels, to the extent that its electrical properties will be strongly affected. Plasmons quickly decay into hot electrons, leading to observable photocurrents,[154,176,177] and eventually thermalize to an elevated electron temperature in extended graphene.[151–153]

In this chapter, we first show that the excitation of a single plasmon in a graphene nanostructure produces profound modifications in its electrical properties, which we then use to detect the presence of the plasmon. Our quantum-mechanical calculations confirm the excellent performance of graphene quantum dots[178] for on-chip electrical detection of single plasmons. More precisely, we find a twofold increase in the electrical current passing across a nanographene junction when one of its plasmons is excited. Furthermore, we scale up the size of the nanostructure and demonstrate an efficient mid-infrared photodetector working at room temperature, together with our experimental collaborators.

5.2 Ballistic electrical detection of graphene plasmons

5.2.1 Theoretical model

Our proposed structure is based on the concept of molecular junctions,[179–183] as illustrated in Fig. 5.1a, where a graphene hexagon quantum dot (GHQD) is contacted to two semi-infinite graphene sheets that act as electrodes. The GHQD (2 nm side length) is connected to these electrodes through two carbon-carbon bonds on either side, thus configuring a nanojunction.

Here, we simulate the optical response of graphene by using the random-phase approximation to calculate the noninteracting susceptibility,[49] in which the electronic states j are obtained from a nearest-neighbors tight-binding model with a hopping energy of $t = 2.8\,\text{eV}$ (see Section 1.3 for more details). We consider realistic levels of doping and graphene quality, with an intrinsic electron lifetime $\tau = 66\,\text{fs}$ (*i.e.*,

$\hbar\tau^{-1} = 10\,\text{meV}$). In order to include the effect of the DC biased contacts, we supplement the tight-binding Hamiltonian H_{TB} with the an electrostatic potential set up by such bias, including the potential resulting from the static response of the GHQD. The electronic states of the system are then calculated following a series of self-consistent iterations until convergence in the Hartree term incorporating the DC potential is achieved.

The external perturbation from the incident light is introduced through a potential $\phi^{\text{ext}}(\mathbf{r}) = -\mathbf{r}\cdot\mathbf{E}^{\text{ext}}$, where $\mathbf{E}^{\text{ext}}$ is the light electric field. This allows us to calculate the absorption cross-section σ_{abs} obtained from Eq. 1.38.

After excitation and subsequent decay of plasmons in the GHQD, the system is thermalized within 10s fs. We compute the electron temperature as[38]

$$T_{\text{e}} = \left[\frac{F_{\text{in}}\sigma_{\text{abs}}(\hbar v_{\text{F}})^2}{2.3Ak_{\text{B}}^3}\right]^{\frac{1}{3}}, \tag{5.1}$$

where F_{in} is the incident light fluence, $v_{\text{F}} \approx 10^6\,\text{m/s}$ is the Fermi velocity, k_{B} is the Boltzmann constant, and A is the graphene area. Then, we can calculate the chemical potential by requiring that the Fermi-Dirac distribution $f_{T_{\text{e}}}(E_j)$ conserves the number of electrons and describes an excess of energy equal to the absorbed energy (absorption cross-section times light fluence, see below) relative to the ground state. A temperature-dependent Hartree term is also obtained, incorporating the electron distribution $f_{T_{\text{e}}}(E_j)$.

We evaluate current-voltage (I-V) curves using the well-known expression[179, 184–186]

$$I = \frac{2e}{h}\int_{-\infty}^{+\infty} dE\;\; T(E,V)\left[f_{T_{\text{e}}}(E-\mu_{\text{L}}) - f_{T_{\text{e}}}(E-\mu_{\text{R}})\right], \tag{5.2}$$

where $\mu_{\text{L}} = E_{\text{F}} - eV/2$ and $\mu_{\text{R}} = E_{\text{F}} + eV/2$ are the electrochemical potentials in the two contacts, which are assumed to remain in local equilibrium, E is the electron energy, $f_{T_{\text{e}}}(E) = [1+\exp(E/k_{\text{B}}T_{\text{e}})]^{-1}$ is the Fermi-Dirac distribution at an electron temperature T_{e} of electrodes, and $T(E,V)$ is the transmission function[132] (see Appendix E). We assume an initial temperature (before illumination) $T_{\text{e}} = 300\,\text{K}$ in this section.

We have calculated the density of state (DOS) at the edge of a doped semi-infinite graphene sheet by direct summation of tight-binding electron states in ribbons of increasing width. We find the result to be nearly indistinguishable from the DOS for infinite graphene, which in the range of electron energies E under consideration ($-t \leqslant E \leqslant t$) reduces to the analytical expression[33]

$$D(x) = \frac{8}{\pi^2}x^2\frac{1}{\sqrt{4(1+x)^2-(x^2-1)^2}}\Phi\left(\frac{\pi}{2}, 4\sqrt{\frac{x}{4(1+x)^2-(x^2-1)^2}}\right), \tag{5.3}$$

where $x = |E/t|$ and $\Phi(\pi/2, y)$ is the complete elliptic integral of the first kind.

The average number of plasmons excited in the nanojunction by an incident pulse of fluence F_{in} is given by

$$n_{\text{p}} = \frac{F_{\text{in}}\sigma_{\text{abs}}}{\hbar\omega_{\text{p}}}, \tag{5.4}$$

where $\hbar\omega_{\text{p}}$ is the plasmon energy and σ_{abs} is the absorption cross-section. We further define the plasmon-to-charge conversion efficiency as the ratio[187,188]

$$\eta = \frac{|i_{\text{on}} - i_0|}{e} \frac{\hbar\omega_{\text{p}}\Delta t_{\text{eff}}}{F_{\text{in}}\sigma_{\text{abs}}}, \tag{5.5}$$

which gives the additional number of electrons circulating through the junction as a result of plasmon excitations, normalized to the number of exciting plasmons (*i.e.*, each excited plasmon produces the circulation of η additional electrons through the junction during its lifetime). Here, i_{on} and i_0 are the currents under resonant illumination and in the absence of illumination, respectively, while Δt_{eff} is an effective time interval during which the electron gas remains at an elevated temperature after pulse irradiation. We take $\Delta t_{\text{eff}} = 200\,\text{fs}$ as a conservative estimate.[149,150]

5.2.2 Toward single plasmon detection

We assume the entire structure to be doped to a Fermi level of 0.8 eV and consider an external illumination with polarization perpendicular to the junction. For this polarization, the plasmons excited in the GHQD should have the bulk of their induced charge piled up near the sides of the hexagon that are far from the semi-infinite contacts. Therefore, these plasmons are indeed similar to those of the isolated hexagon (*i.e.*, without the contact). We thus neglect the contacts in the optical response and focus on the central part of the nanojunction in order to simplify our analysis. A pronounced plasmon resonance is observed at $\sim 1\,\text{eV}$ in the simulated absorption spectrum (Fig. 5.1b), which has a dipolar nature (see inset).

We now calculate the electrical *I-V* response of the nanojunction for different incident photon energies using the Landauer formalism,[184–186] formulated in Eq. 5.2. In particular, we show the current right after light pulse irradiation and subsequent thermalization of the electron gas at an elevated temperature T_{e}. The results are shown in Fig. 5.1c. When the external illumination ($30\,\text{mJ/m}^2$ fluence) is resonant with the dominant GHQD plasmon observed in Fig. 5.1b, a clear amplification of the current i_{on} is observed (red curve) compare with the current i_{off} for off-resonance illumination (blue curve) or the current i_0 in the absence of external light (dashed curve). The maximum variation predicted by this figure between on- and off-resonance conditions corresponds to a factor of 2 in the observed current.

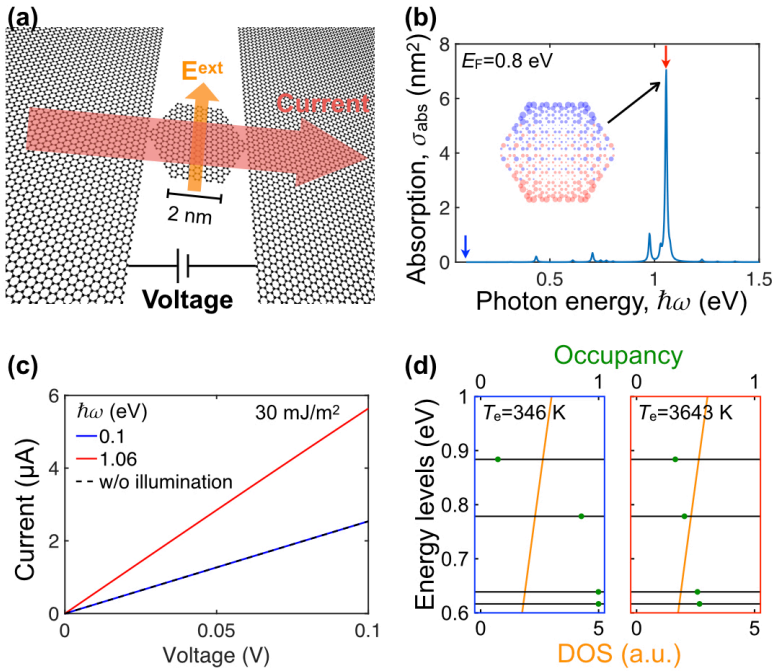

Figure 5.1: **Electrical detection of plasmons in a graphene hexagon quantum dot (GHQD) nanojunction.** (a) We show a sketch of the structure under consideration, consisting of a GHQD connected to two semi-infinite graphene sheets that operate as electrical contacts. Currents are measured under an applied direct current (DC) bias across the nanojunction, possibly in the presence of plasmons excited by external light that is polarized along the perpendicular direction. (b) Calculated absorption cross-section of a single GHQD doped to a Fermi energy $E_F = 0.8$ eV. A pronounced plasmon resonance peak is observed at ~ 1 eV photon energy, whose associated induced charge in shown as an inset. (c) Calculated current as a function of bias voltage in the presence of external illumination for two different photon energies, corresponding to on- and off-resonance conditions relative to the prominent plasmon shown in (b) (red and blue curves, respectively). The current in the absence of external illumination is shown as a dashed curve. (d) Electron energy levels (left scale, horizontal lines) of the GHQD in the presence of external illumination under on- and off-resonance conditions (right and left panels, respectively). We also show the density of states (DOS, orange curves, lower scale) of extended graphene, the electron temperature T_e right after irradiation (labels), and the level occupancy (upper scale, green dots). The latter is dramatically reduced near the Fermi level (0.8 eV) under resonant illumination (right panel).

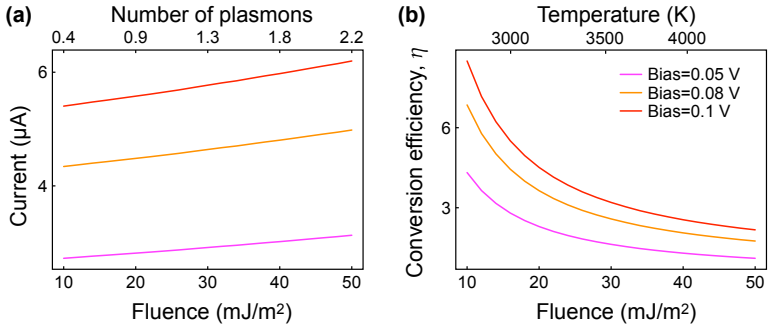

Figure 5.2: **Toward single plasmon detection.** (a) Calculated current as a function of incident light fluence (lower scale) for different DC bias voltages in the same structure as in Fig. 5.1a. We consider a resonant photon energy $\hbar\omega = 1.06\,\text{eV}$. (b) Plasmon-to-charge conversion efficiency as a function of incident light fluence. The fluence-dependent number of excited plasmons and the electron temperature right after laser pulse irradiation are shown as upper scales in (a) and (b), respectively.

As expected, the current scales linearly with the DC applied voltage (Fig. 5.1c). The slope of these curves is related to the number of available electronic levels contained in the central GHQD for energies lying in between the Fermi levels of the two gates, as shown in Fig. 5.1d. Actually, we can obtain further insight into the plasmon-enhanced conductivity of the nanojunction by examining the distribution of GHQD energy levels with and without excited plasmons (Fig. 5.1d). In the absence of external illumination or under off-resonance conditions (Fig. 5.1d, left panel), the island shows several unoccupied electronic states right above the Fermi level. When switching to on-resonance illumination, the occupancy of these energy levels is dramatically modified (Fig. 5.1d, right panel, green dots) as a result of energy absorption from the optical pulse. This effect is more pronounced for states that are closer to the unbiased Fermi energy, which therefore contribute more efficiently to modify the electrical conductivity of the GHQD, leading to amplification of the currents when plasmons are excited. Another element that controls the obtained current is the electronic density of states (DOS, given in Eq. 5.3) of the graphene contacts (Fig. 5.1d, lower scales), which evolves rather smoothly over the relevant range of electron energies.

The number of plasmons that are required to be excited in the GHQD in order to observe a detectable variation in the current across the junction is an important parameter that permits us to assess the performance of the device. We show in Fig. 5.2a the dependence of the current on light fluence under on-resonance illumination conditions ($\hbar\omega = 1.06\,\text{eV}$) for different DC bias voltages applied across the nanojunction. All curves display a similar linear increase of the current with light fluence, although

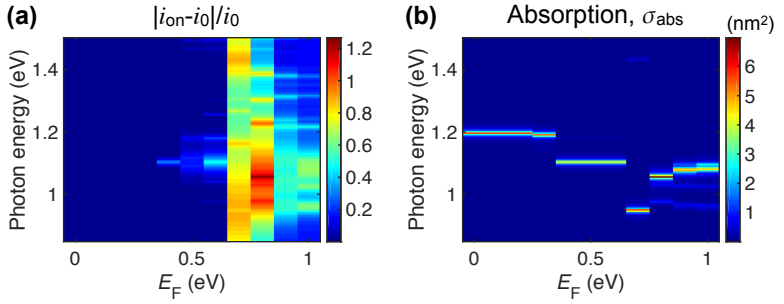

Figure 5.3: **Plasmometer based on a GHQD junction.** (a) Variation of the electric current through the device of Fig. 5.1a (color scale) as a function of both incident photon energy and Fermi energy for a fixed DC bias voltage of 0.1 V and a light fluence of 30 mJ/m^2. (b) Absorption cross-section of the GHQD under the same condition as in (a).

larger voltages produce more intense currents and reveal a nonlinear dependence of the elevated electron temperature. We also show the average number of plasmons sustained by the GHQD (upper scale), as estimated from the optical absorption cross-section, and the plasmon energy. These results indicate that the device is capable of detecting single-plasmons. Nevertheless, the current shows a monotonic increase with light fluence, which should directly permit correlating the readout of an ammeter with the number of plasmons excited by the optical pulse in the graphene nanoisland. We thus propose to exploit the graphene nanojunction as a plasmometer with a sensitivity down to the single-plasmon level.

An important figure of merit for our plasmometer is the so-called plasmon-to-charge conversion efficiency η,[187,188] defined in Eq. 5.5, which gives the number of additional electrons that circulate through the junction as a result of the excitation of one plasmon. As a conservative estimate of η, we assume that the electron stays at the initial elevated temperature during 200 fs, which is of the order of what is observed in pump-probe experiments.[149,150] Remarkably, the efficiency reaches values of 8 electrons per plasmon (Fig. 5.2b), which is around 18 times larger than previously obtained results for plasmons propagating along silver nanowires.[188] Additionally, a negative correlation between efficiency and light fluence is observed, consistent with previous experimental studies.[188]

5.2.3 Toward a tunable plasmometer

Via chemical doping or electrical gating, the spectral position of the plasmon resonance supported by our proposed device (Fig. 5.1a) can be varied over a wide spectral

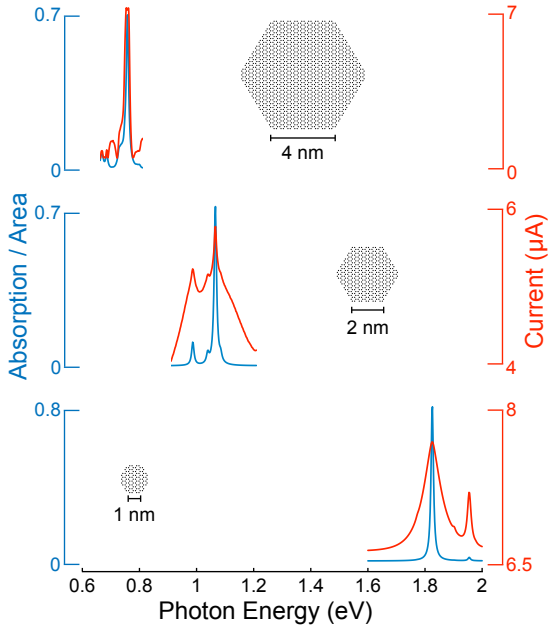

Figure 5.4: **Size dependence of the plasmometer performance.** We present the optical absorption cross-section (left scales) and the electric current through the plasmometer device (right scales) as a function of incident photon energy for GHQDs of different side lengths (4, 2, and 1 nm, from top to bottom).

range, as shown in Fig. 5.3b. It is reassuring to observe that the corresponding electrical signal (Fig. 5.3a) shows a similar dependence on both the doping level and the photon energy as the optical absorption of the GHQD (Fig. 5.3b), further supporting the ability of the nanojuction to serve as a plasmometer (*i.e.*, as a nanoscale spectrometer from the point of view of the external illumination). We note that the stronger spectral variations of electrical current are observed at higher Fermi energies due to the availability of a denser set of electronic states that are influenced by optical heating. Remarkably, the variation of the electric current follows rather closely the evolution of the occupancy of electron states in the vicinity of the Fermi level (similar to that shown in Fig. 5.1d), with strong features emerging near the plasmon resonances.

An alternative way of shifting the plasmon energy consists in changing the size of the GHQD. A series of nanoscale devices similar to the one considered above could then act simultaneously to detect different light wavelengths. As we show in Fig. 5.4,

when the size of the GHQD decreases, the main plasmon resonance moves to higher photon energies, thus covering the near-infrared spectral region. Importantly, the resonance features in the electrical spectra also shift to higher photon energies (Fig. 5.4, right scale) and actually coincide with the resonance peaks in the absorption cross-section (left scale). This further corroborates the excellent performance of the proposed nanojunction as a spectral plasmometer device.

5.3 Efficient detection of mid-infrared light at room temperature

Inspired by the theoretical predictions presented in the last section, we continue our design for the plasmometer, eventually leading to an efficient mid-infrared photodetector as we show in this section. Note that the experimental results presented here are from our collaborators.

5.3.1 Operating mechanism and device characterizations

Our designed structure is shown in Fig. 5.5a, the experimental images of which are displayed in Fig. 5.5f. It is composed of two metal electrodes and a photoactive channel, which consists of multiple graphene-disk plasmonic resonators (GDPRs) connected by graphene nanoribbons (GNRs). The graphene structure is on a 60 nm diamond-like carbon (DLC) thin film grown on a silicon substrate. GDPRs serve both as sources of thermalized carriers produced by plasmonic resonances therein and leads to GNRs. Due to the significant mismatch between the geometrical dimensions of GDPRs and GNRs, the electrical conductance of the device is dominated by that of GNRs, which possess attractive transport properties. First of all, lateral confinement produces a bandwidth of $\sim \Upsilon/W$ ($\Upsilon \sim 0.5\,\mathrm{eV}\cdot\mathrm{nm}$ with W the GNR width[189,190]); furthermore, the fabrication process generates a high degree of edge roughness in GNRs, which in turn introduces disordered localized potentials[189–192] to affect the carrier transport therein.

For low or moderate T_e, the carrier transport is dominant by the nearest-neighbor hopping (NNH)[190] with a characteristic thermal activation energy $k_B T_{NNH}$. On the other hand, for sufficiently high T_e, carrier thermal excitation (TCE) directly over the potential obstacles provides an additional transport channel[189,190,193] characterized by a higher activation energy $k_B T_{TCE}$. Both NNH and TCE processes are sensitive to T_e. Figures 5.5b-e illustrate the operating principle of our device on the basis of these concepts. The excitation and the subsequent decay of plasmons (eventually increasing the electron temperature) are identified as a thermal activation mechanism of the electrical conductivity in the device.

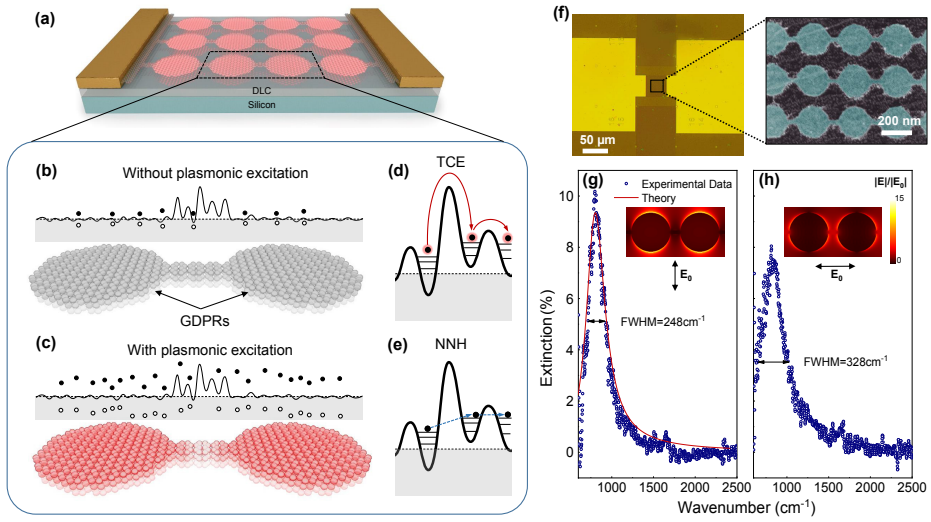

Figure 5.5: **Device design and operation principle.** (a) Schematic of the proposed device, composed of graphene-disk plasmonic resonators (GDPRs, red circles) connected by quasi-1D graphene nanoribbons (GNRs). (b) Cartoon illustrating the disorder potential (solid curve) around the chemical potential before photoexcitation. The grey shadowed area denotes the states occupied by electrons, whereas filled and open circles refer to electrons and holes associated with thermal smearing at room temperature. (c) After photoexcitation on resonance with the graphene plasmons, electron-hole pairs are produced, resulting in a higher charge-carrier temperature T_e. (d) Illustration of thermal-carrier excitation (TCE) transport, in which electrons with higher thermal energy can overcome the localized potential barriers. (e) Illustration of nearest-neighbor hopping (NNH) transport, in which thermalized electrons evanescently hop between neighboring localized states under the driving external electric field. We use electrons to illustrate the principles of carrier transport for conceptual simplicity. (f) Optical image of the device (left) and false-color scanning electron micrograph of the graphene region (right). (g, h) Infrared extinction spectra of the graphene area for incident light polarization perpendicular (g) and parallel (h) to the GNRs. Insets of (g) and (h) show simulated electric-field distributions ($|E| / |E_0|$) at the corresponding plasmon resonance. The solid-red curve in (g) is the calculated graphene absorption.

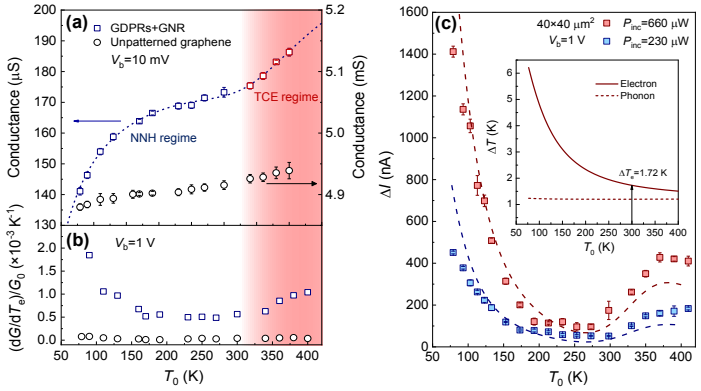

Figure 5.6: **Temperature dependence of carrier transport and photocurrent generation.** (a) Conductance (G) versus environment temperature (T_0) for our graphene-plasmon device (square symbols) compared with unpatterned graphene (circles). We use 3-layer graphene and a device of $40 \times 40\,\mu\text{m}^2$ area in both cases. Due to the small channel resistance, the conductance of unpatterned graphene devices is acquired with a bias voltage $V_\text{b} = 10\,\text{mV}$ using a four-point probe configuration that eliminates the effect of contact resistance. The blue-dashed curve is a theoretical fit from Eq. 5.6. (b) Measured $(\Delta G/\Delta T_\text{e})/G_0$ for both the graphene-plasmonic and unpatterned-graphene devices with $V_\text{b} = 1\,\text{V}$. (c) T_0 dependence of the photocurrent in the plasmonic device under $12.2\,\mu\text{m}$ excitation with incident power $P_\text{inc} = 230\,\mu\text{W}$ (blue) and $660\,\mu\text{W}$ (red). Inset: calculated electron (solid curve) and phonon (dashed curve) temperature increases (ΔT_e and ΔT_l) under $P_\text{inc} = 660\,\mu\text{W}$. The incident light is polarized parallel to the GNRs.

In the experiment, the doping level of the stacked graphene is $E_\text{F} \sim -0.45\,\text{eV}$. The diameter of the GDPR is 210 nm, and the length and width of the GNR are 60 nm and 20 nm, respectively. Measured infrared extinction spectra are presented for the incident light polarized either perpendicularly (Fig. 5.5g) or parallel (Fig. 5.5h) to the GNR. In the inserts of Figs. 5.5g-h, we provide simulated near-field distributions at plasmonic resonances. For both polarization directions, GDPRs support the first dipolar plasmonic modes (insets of Figs. 5.5g-h) that create an absorption peak at a wavenumber of $\sim 820\,\text{cm}^{-1}$, in an excellent agreement with the analytical model (solid red curve in Fig. 5.5g, see Section 2.5). When the light polarization is parallel to GNRs, the FWHM of the plasmonic absorption peak covers a wavelength range spanning from 10 to $16\,\mu\text{m}$.

Figure 5.6a (square symbols) shows the conductance G of the device shown in Fig. 5.5 as a function of the ambient temperature (77−400 K), measured at a low bias voltage

$V_b = 10\,\mathrm{mV}$ such that the Joule heating is negligible and the device operates near the thermal equilibrium ($T_e = T_l = T_0$). The device has a total size of $40 \times 40\,\mu\mathrm{m}^2$. We find that the electrical conductance shows two different behaviors in the measured temperature range: a NNH low-temperature behavior from 77 to 300 K; and a TCE behavior at high temperatures when electrons acquire enough thermal energies to be excited and cross the disordered potentials. We can model $G(T_e)$ as a sum of these two contributions as,

$$G(T_e) = B_{\mathrm{NNH}} e^{-T_{\mathrm{NNH}}/2T_e} N + B_{\mathrm{TCE}} e^{-T_{\mathrm{TCE}}/2T_e} (1-N), \tag{5.6}$$

with fitting parameters $B_{\mathrm{NNH}} = 186.79\,\mu\mathrm{S}$, $B_{\mathrm{TCE}} = 276.17\,\mu\mathrm{S}$, $T_{\mathrm{NNH}} = 42.8\,\mathrm{K}$, and $T_{\mathrm{TCE}} = 306.2\,\mathrm{K}$. In addition, we introduce another T_e dependent function $N = [\exp(10T_e/T^* - 10) + 1]^{-1}$, in which $T^* = 342\,\mathrm{K}$ acts as a characteristic temperature that separates the two regimes. The measured data are well reproduced by Eq. 5.6 (dashed curve in Fig. 5.6a) and the fitted activation temperatures are reasonably consistent with those of previous studies.[189–192] The thermal coefficient of conductance $(\Delta G/\Delta T_e)/G_0$, where G_0 is the channel conductance in the absence of external illumination, displayed in Fig. 5.6b indicates the device responsivity. It presents a factor of >20 increase over a wide temperature range with respect to the measurement done on an unstructured 3-layer graphene sheet.

To evaluate in more detail the infrared photoresponse of our device, it is essential to determine the increase in electron temperature ΔT_e due to Joule heating and light absorption. Here, we again adopt a two-temperature model to characterize the electron T_e and the lattice T_l temperatures in graphene. In the steady-state limit, we find the total absorbed power $P = S_a A\left(T_e^3 - T_l^3\right)$. The conservation of the heat flow imposes the condition $A\left(T_e^3 - T_l^3\right) = \kappa(T_l - T_0)$, where the cooling pathway due to carrier diffusion to the metal contacts is incorporated in the effective active area S_a. Here, A is the electron-lattice coupling coefficient, dominated by the disorder-assisted supercollision cooling,[157] while κ is the coefficient of heat dissipation to the substrate. The direct solution of these two equations allows us to write the electron temperature as (see Sections 1.4.2 and 4.3)

$$T_e = \left[\left(\frac{P}{S_a\kappa} + T_0\right)^3 + \frac{P}{S_a A}\right]^{1/3}. \tag{5.7}$$

From Eqs. 5.6 and 5.7, we obtain the calculated mid-infrared photoresponse shown in Fig. 5.6c (dashed curves), which agrees well with the measured photocurrents (symbols in Fig. 5.6c) at a fixed bias voltage of 1 V. Here, we take $A = 7.89\,\mathrm{Wm^{-2}K^{-3}}$ and $\kappa = 1\,\mathrm{MW/m^2K}$ by assuming that the thermal conductivity of DLC is around 0.15 W/mK.[194] The inset in Fig. 5.6c shows complete solutions of T_e and T_l, displaying a rise in electron temperature $\Delta T_e = T_e - T_0 \sim 1.72\,\mathrm{K}$ at $T_0 = 300\,\mathrm{K}$ for an

incident power $P_{\text{inc}} = 660\,\mu$W. Note that the in-plane thermal conductivity, limited by phonons, of the GNR ($\sim 80\,$W/mK)[195] is much larger than the thermal conductivity of the DLC, which leads to a negligible temperature gradient along the GNR, so we assume a uniform value of T_e in the graphene nanostructure for our analysis.

5.3.2 Device scaling

When scaling down the device area S_d, an increase in Joule heating is created from the increased electrical power per unit area in the device $V_b I_0/S_d$. Under the same measurement conditions as in Fig. 5.6 with $P_{\text{inc}} = 660\,\mu$W and $V_b = 1\,$V, we note that devices with a smaller footprint area enter into the TCE regime at a much lower ambient temperature ($\sim 340\,$K, $\sim 280\,$K, and $\sim 250\,$K for $40 \times 40\,\mu$m^2, $10 \times 10\,\mu$m^2, and $5 \times 5\,\mu$m^2 devices, respectively), as shown in Fig. 5.7a-c by shaded areas, which is well described by the theory (dashed curves in Fig. 5.7a-c).

In order to further understand the role of Joule heating, we also studied the relationship between the photocurrent and V_b. For the $10 \times 10\,\mu$m^2 device at $T_0 = 77\,$K, the responsivity shows two distinct regimes (the two slopes in the blue symbols in Fig. 5.7d, moving from NNH to TCE regime with the increase of V_b). In contrast, for the $5 \times 5\,\mu$m^2 device under the same conditions, a voltage of 1 V is sufficient to drive the device into the TCE regime without further changing the responsivity (red dashed curve in Fig. 5.7d). Note that the Joule heating plays an important role here not only for its ability to thermally bring the device operating in the TCE regime which offers greater responsivity, but also to increase the power dynamic range of the device. In Fig. 5.7e, ΔI is shown as a function of the total incident power P_{inc} and the actual incident power on the device, from which the external responsivity $\Delta I S/(P_{\text{inc}} S_d)$, with S the area of the beam spot, is extracted to be 16 mA/W at room temperature. It is obvious that the device works more linearly as a function of the incident light power when operating in the TCE regime ($T_0 = 300\,$K) with respect to the NNH regime ($T_0 = 77\,$K). Considering the exceptionally low electronic heat capacity of graphene (see Sections 1.4.2 and 4.2), we predict that the device remains operational at GHz light modulation frequencies.

5.4 Conclusions

In summary, in the first part of this chapter, we have shown through state-of-the-art quantum-mechanical simulations that a compact graphene nanojunction (several tens of nanometers in size) constitutes a ballistic device capable of yielding the number of plasmons excited in a central graphene island with a sensitivity down to the single plasmon level. The conductivity of the junction is shown to be severely modified by the presence of excited plasmons, thus permitting a direct readout of the number of

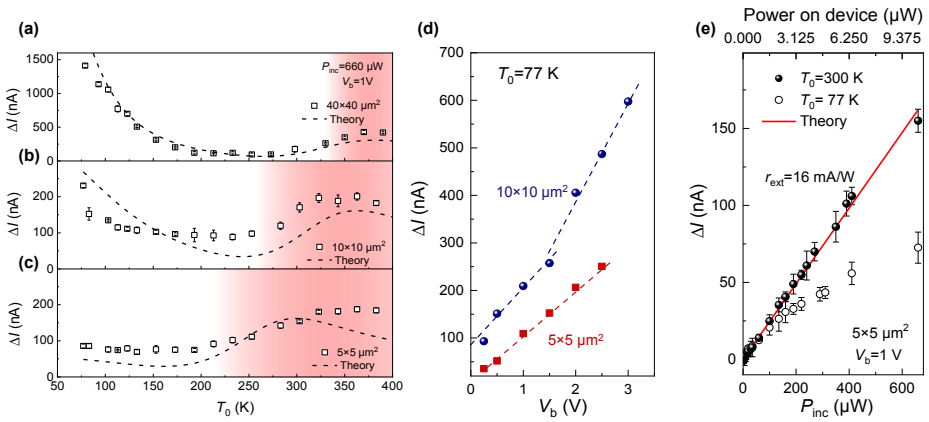

Figure 5.7: **Device scalability and effect of Joule electron heating on the responsivity.** (a-c) Dependence of the photocurrent ΔI on environment temperature for devices of (a) $40 \times 40\,\mu\text{m}^2$, (b) $10 \times 10\,\mu\text{m}^2$, and (c) $5 \times 5\,\mu\text{m}^2$ area using fixed incidence power $P_{\text{inc}} = 660\,\mu\text{W}$, bias voltage $V_{\text{b}} = 1\,\text{V}$, and light polarization (parallel to the GNRs). (d) Dependence of ΔI on V_{b} for the $10 \times 10\,\mu\text{m}^2$ (circles) and $5 \times 5\,\mu\text{m}^2$ (squares) devices at an environment temperature $T_0 = 77\,\text{K}$. Dashed lines are guides to the eye. (e) ΔI as a function of P_{inc} for the $5 \times 5\,\mu\text{m}^2$ device. The upper horizontal scale shows the power actually impinging on the device area. Filled (open) symbols represent data acquired at $T_0 = 300\,\text{K}$ (77 K). The red-solid curve is the theoretical result.

such excitations through a measurement of the electric current for a given bias voltage applied between the gates on either side of the junction. This strong dependence of a nanographene quantum dot conductivity on its optical excitation state is inherited from the peculiar band structure of this material, through essentially the same mechanism that endows it with a strong electro-optical tunability: small changes in the electronic structure are amplified through the participation of a large number of conduction electrons in the optical response,[38] but also in the electric transport properties.

In the second part of this chapter, after scaling up the junction in size, we access the mid-infrared spectral region and demonstrate, together with our experimental collaborators, an un-cooled and extremely sub-wavelength device that can efficiently detect mid-infrared light with a broad operational bandwidth (at GHz light modulation frequencies). Our design therefore holds great potential for on-chip nanophotonic devices comprising photodetectors, spectrometers, and sensors, as well as for nanoscale quantum devices that benefit from its ability to resolve single plasmons.

6

Plasmonic sensing with graphene

6.1 Introduction

Localized surface plasmon (LSPs) have attracted considerable attention in the nanophotonics community due to their pivotal role in optical sensing applications such as antibody-antigen,[196–198] gas,[199,200] and pH[201,202] sensors. These excitations also enable the detection and chemical identification of single molecules through their enhancement of molecule-specific Raman scattering intensities.[5–9,203] LSPs are routinely observed in noble metal nanostructures, appearing as pronounced spectral features in their optical absorption and scattering spectra. Plasmon-based sensing heavily relies on the ability of these collective modes to confine and strongly amplify the optical near-field. These properties are equally responsible for the large nonlinear optical response observed in metal nanoparticles,[21,204–208] which has inspired alternative mechanisms for nonlinear plasmonic sensing. For instance, the aggregation of gold nanoparticles caused by targeted heavy metal ions,[209] *Escherichia coli* bacteria,[210] or Alzheimer's disease biomarkers[211] can be detected through an increase in second-harmonic generation (SHG). Additionally, third-harmonic generation has been recently claimed to offer great sensitivity to the dielectric environment compared to the linear response.[212]

Doped graphene is widely recognized as a promising material platform for plasmonics, capable of supporting electrically tunable plasmons with higher quality factors and spatial confinement than those of metal nanoparticles.[41,45,73,79,213] Moreover, tunable graphene plasmons, so far observed at mid-infrared and THz frequencies, provide the strong near-electric-field confinement needed for sensing.[134,214–216] In particular, graphene plasmons have been demonstrated to reveal vibrational fingerprints of biomolecules.[134] Additionally, the anharmonic electron motion associated with the Dirac cones of this material[33,53] gives rise to an extraordinary nonlinear response in extended samples.[217,218] LSPs in graphene nanoislands have been predicted to produce unprecedentedly high harmonic generation and wave mixing,[23,219] indicating their strong capability for nonlinear optical sensing.

In this chapter, we show through atomistic quantum-mechanical simulations, provided in Section 1.3, that both the linear and nonlinear optical response of graphene nanoislands can be dramatically altered by the presence of a single neighboring molecule that carries either an elementary charge or a permanent dipole of only a few Debye. As a proof-of-principle demonstration, we focus on small graphene nanohexagons (GNHs), similar to those produced with high-quality through chemical synthesis.[220,221] Our calculations indicate that the presence of an analyte can significantly modify the distribution of conduction electrons in GNHs that are a few nanometers in lateral size,[222] leading to new plasmonic features in their linear optical response. This interaction may also break the nanoisland inversion symmetry, thus enabling plasmon-enhanced SHG.[223] Analyte-induced plasmon features in the absorption spectra and increased

SHG intensities occur even for initially undoped GNHs, suggesting that nanographenes can serve as a tunable and efficient platform for detecting charge- or dipole-carrying molecules.

6.2 Principle of operation

The small size of the GNHs under consideration demands an atomistic level of description to simulate their linear and nonlinear optical response.[23,224] Following the theoretical framework described in Section 1.3, we approximate their electronic structure using a nearest-neighbors tight-binding model.[33,53] The resulting one-electron wave functions are inserted into the random-phase-approximation susceptibility[49,50] to yield the response of the GNHs.[224] A straightforward generalization of this mean-field approach is followed to obtain the SHG response.[23] The interaction with the static charge or dipole of the analyte is included as an external potential, which adds up to the Hartree potential (neglecting exchange). The latter is found self-consistently following a customary iterative procedure that yields the ground state of the nanoisland in the presence of the analyte. We include inelastic processes in the response through a phenomenological relaxation lifetime τ, assuming a conservative value $\tau = 13\,\mathrm{fs}$ (*i.e.*, $\hbar\tau^{-1} = 50\,\mathrm{meV}$).

The charge-carrier distribution of a graphene nanostructure can be significantly altered by the presence of a neighboring charge or dipole,[222] even when the structure is electrically neutral (*i.e.*, undoped). In particular, a charge- or dipole-carrying molecule can produce this effect (Fig. 6.1a). The resulting modifications in the plasmonic response emerge as significant changes in the linear absorption spectrum triggered by the presence of these types of analytes (Fig. 6.1b), thus providing the basis for an optical sensor. We illustrate this effect in Fig. 6.1b, which shows the absorption spectra of a neutral GNH with and without a neighboring molecule carrying an elementary charge. In this example, the analyte induces a blue shift of the prominent absorption peak and creates new features at lower photon energies. Even more dramatic changes are produced in the nonlinear response, which we show in Fig. 6.1c by examining the SHG nonlinear polarizability of the GNH. For the bare nanoisland (blue curve), SHG is strictly forbidden due to inversion symmetry,[223] while in the presence of the analyte (red curve), this symmetry is broken and we observe an intense SHG response for fundamental frequencies near the plasmon resonances of Fig. 6.1b.

6.3 Linear sensing

A more detailed analysis is presented in Fig. 6.2, which shows absorption cross-section spectra of GNHs in the presence of a charge-carrying analyte, represented by an

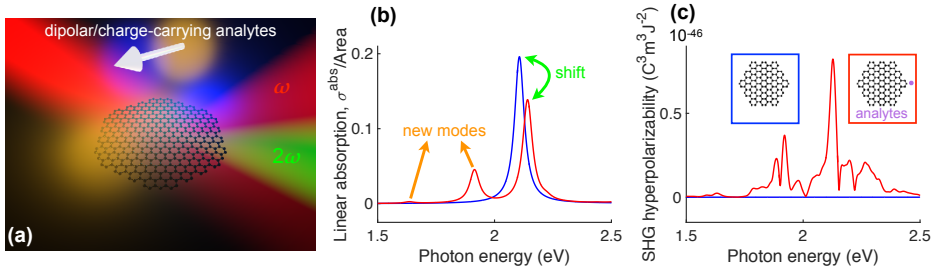

Figure 6.1: **Linear and nonlinear optical sensing with nanographene.** (a) Illustration of an armchair-edged graphene nanohexagon (GNH) interacting with a charge- or dipole-carrying analyte (the white arrow indicates a permanent dipole moment). The molecule induces asymmetry in the nanohexagon conduction electron distribution, which can be detected by measuring either the change in the optical absorption spectrum or the onset of a second-harmonic signal. (b,c) Linear absorption cross-section (b) and second-harmonic polarizability (c) of the GNH in the absence (blue curves) or presence (red curves) of a nearby charge-carrying molecule. The analyte produces new resonance features and spectral shifts in the linear response. Additionally, it enables a large second-harmonic response from the nanohexagon, otherwise prevented by symmetry in its absence.

elementary charge ($Q^{\text{ext}} = e$) placed at a distance d_x from the graphene edge. The external charge produces static changes in the valence electron density (Fig. 6.2, top insets), which lead to modifications in the optical response. Specifically, in an undoped GNH of side length $L = 1\,\text{nm}$, with the external charge located $d_x = 0.5\,\text{nm}$ away from one of the hexagon corners, the static conduction charge displays a highly asymmetric distribution as shown in Fig. 6.2a. This causes new plasmonic modes to appear at 1.6 and 1.9 eV, which display dipolar patterns in their associated induced-charge distributions (see insets). Additionally, the dominant peak of the unexposed nanoisland ($d_x \to \infty$), which also shows a dipolar pattern, undergoes a slight blue shift. Obviously, these effects are reduced in magnitude when the analyte is further away from the GNH ($d_x = 2\,\text{nm}$ curves). When moving to a larger nanoisland ($L = 2\,\text{nm}$, Fig. 6.2c), we observe equally substantial spectral shifts and emerging features caused by the analyte.

When the GNH is highly doped ($Q = -4e$, corresponding to a Fermi energy $\sim 1\,\text{eV}$ for $L = 1\,\text{nm}$, Fig. 6.2b), the charge-carrier distribution is initially centrosymmetric (see top inset), with charge accumulation at the hexagon edges due to Coulomb repulsion. The analyte then induces a small asymmetry, which is insignificant compared to the intrinsic doping. Consequently, only minor spectral changes are observed, even at a short GNH-molecule distance $d_x = 0.5\,\text{nm}$, which nearly disappear for $d_x = 2\,\text{nm}$.

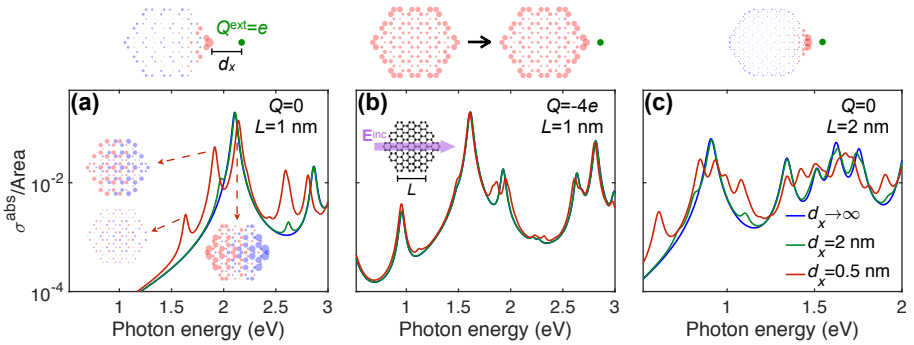

Figure 6.2: **Sensing of charge-carrying analytes through linear optical absorption by nanographenes.** We show the linear absorption cross-section of single GNHs exposed to an individual singly-charged analyte ($Q^{\text{ext}} = e$) placed in the graphene plane at different distances d_x from the carbon edge (see legend in (c)). Doped (b) and undoped (a,c) nanohexagons are considered with different side lengths L (see labels). Conduction charge distributions are plotted above each corresponding panel for $d_x = 0.5\,\text{nm}$. Optically induced charge distributions are shown in (a) for three dominant resonances (blue and red indicate charges of opposite signs). Spectra for unexposed graphene correspond to $d_x \to \infty$.

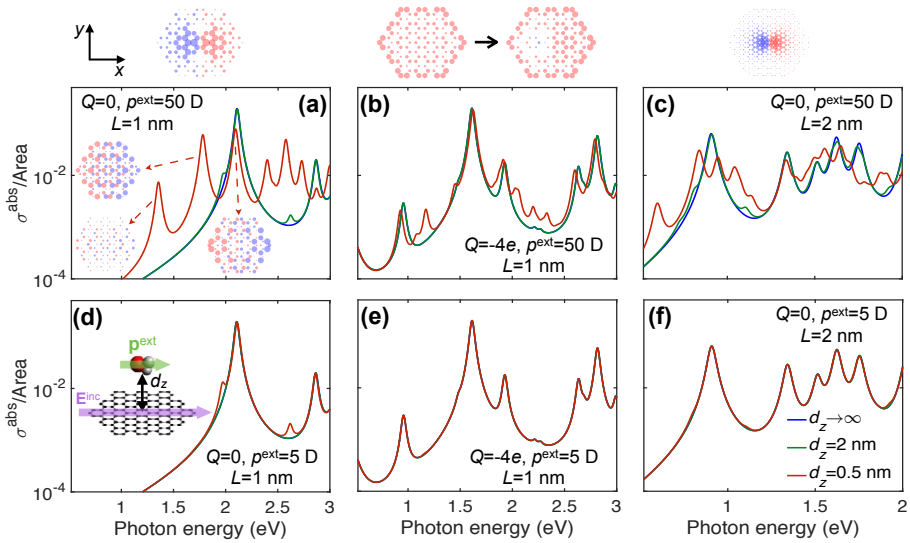

Figure 6.3: **Sensing of dipolar molecules through the linear optical absorption of nanographenes.** We show the linear absorption cross-section of individual GNHs exposed to a single analyte carrying a permanent dipole ($p^{\text{ext}} = 50\,\text{D}$ in (a-c); $p^{\text{ext}} = 5\,\text{D}$ in (d-f)) placed at different distances d_z above the hexagon center (see inset to (d)). Doped (b,e) and undoped (rest of the panels) nanohexagons are considered with different side lengths L, as indicated by labels. Conduction charge distributions are plotted above (a-c) for $d_z = 0.5\,\text{nm}$. Optically induced charge distributions are shown in (a) for three dominant resonances. Unexposed graphene is represented by $d_z \to \infty$.

High initial doping is thus detrimental for linear-absorption sensing. Nevertheless, we have considered here singly-charged analytes, while typical charge-carrying analytes, such as heavy metal ions, can hold many electrons, producing more intense modifications in the nanohexagon absorption, even when it is doped.

In a similar fashion, GNHs can serve as detectors for dipolar analytes, which we represent as point dipoles $\mathbf{p}^{\text{ext}}$. We note for reference that small molecules (*e.g.*, some toxic contaminants) have typical permanent dipoles of a few Debyes[225] (e.g., 1.83 D in hydrogen fluoride, 2.98 D in hydrogen cyanide, and 10.6 D in hydrogen cyanide trimer). For illustration, we first consider the effect of a larger dipole $p^{\text{ext}} = 50\,\text{D}$ (a characteristic value of ZnSe and CdSe nanocrystals[226,227]) placed at different distances d_z above the hexagon center (see inset to Fig. 6.3d); this is an academic exercise, as the size of a structure carrying such large dipoles exceeds the small

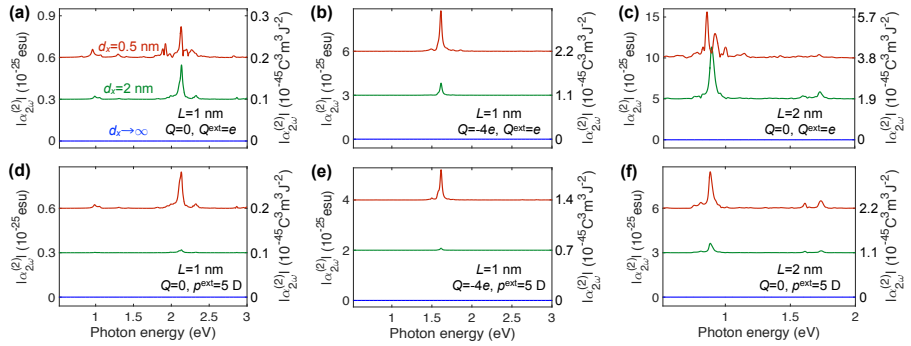

Figure 6.4: **Nonlinear sensing of charged and dipolar analytes.** We show second-harmonic polarizability spectra of single GNHs in the presence of an individual singly-charged (a-c) or dipole-carrying (d-f) molecule. Results for charged (dipolar) analytes are obtained using the same parameters as in Fig. 6.2a-c (Fig. 6.3d-f).

separation distances under consideration. We find the linear optical absorption Fig. 6.3a-c to be modified in a qualitatively similar manner as by the charged analyte (Fig. 6.2), with dipolar resonances appearing again in the spectra. However, when considering a smaller permanent dipole $p^{\text{ext}} = 5\,\text{D}$ (*i.e.*, like in the simple molecules noted above), the linear absorption is rather insensitive to the analyte, even for very small separation distances (Fig. 6.3d-f), so linear response is not useful for sensing such molecules.

6.4 Nonlinear sensing

In contrast, the GNH nonlinear response undergoes large modifications for both charge- and dipole-carrying analytes, as we show in Fig. 6.4, where we present second-harmonic polarizability spectra corresponding to the systems considered in Figs. 6.2 and 6.3. In the absence of the analyte ($d_x \to \infty$), no signal is generated due to inversion symmetry. However, the presence of an elementary charge (Fig. 6.4a-c) or a dipole of 5 D (Fig. 6.4d-f), which are typical values for small molecules, produces a substantial SHG response. Like in previous studies,[23] this response is enhanced by plasmons of the nanostructure, particularly by the new resonances that emerge due to the GNH-molecule interaction. In fact, the values of the SHG polarizability shown in Fig. 6.3 are comparable to those measured for $\sim 10-20\,\text{nm}$ noble-metal nanostructures,[228–231] which are among the best currently available nonlinear materials. We remark that in contrast to the insensitivity of the linear optical response to a dipole $p^{\text{ext}} = 5\,\text{D}$ (Fig. 6.3d-f), the dipolar analyte generates an intense SHG response

(Fig. 6.4d-f) comparable to that created by a charged analyte (Fig. 6.4a-c), although it quickly vanishes at distances of a few nanometers.

6.5 Conclusions

In summary, we have demonstrated through atomistic quantum-mechanical simulations that nanographenes can serve as optical sensors of charge- and dipole-carrying analytes with single-molecule sensitivity. We find substantial changes in the optical absorption spectra induced by the presence of the analytes. Additionally, a strong SHG signal is enabled even in centrosymmetric nanographenes, whose second-harmonic response disappears in the absence of the external perturbation produced by the analyte. The remarkably high sensitivity that we observe in these nanostructures is inherited from the intrinsically large electro-optic tunability of graphene, which offers an extra degree of control to optimize the sensing capability.

As a practical realization, nanographene structures could be passivated with thin insulating layers, which would protect them from undesired chemical interactions (*e.g.*, charge transfer) in the complex environment of the analyte. As an example, nanographenes could be deposited on a dielectric substrate, and then covered with a subnanometer passivating layer that enables large graphene-analyte electrostatic interactions as considered in this chapter. Colloidal dispersions of nanographenes constitute another option, for which electrical doping produced by charge transfer from the analytes or other surrounding molecules should be taken into consideration. While the averaging effect due to the random spatial distribution of the analytes relative to the GNHs is very detrimental for linear sensing, this is not the case for nonlinear sensing. It is worth mentioning that the ability to detect charge- or dipole-carrying analytes, such as hydrogen cyanide or heavy metal ions, which are extremely toxic substances, is crucial for the protection of human health and the natural environment. The method explored here constitutes an attractive avenue in this direction. It should be noted that an advantage of SHG sensing lies in its robustness against undesired electrical doping and variations in size and morphology of the nanographenes, provided they are centrosymmetric. We remark that the present results rely on very conservative values of the inelastic damping, and therefore, higher-quality graphene nanostructures should contribute to enhance and sharpen the optical linear and nonlinear signals. Overall, the scheme proposed here constitutes a radical departure from existing optical sensing approaches and holds great potential for pushing the limits of detectability well beyond what is currently achievable.

Conclusion and outlook

In summary, in this thesis we exploit the extraordinary electrical, thermal, and optical properties of graphene to explore multiple novel designs of graphene-based nanosystems with different types of functionalities.

The main results of this thesis are as follows:

- **Universal analytical modeling of plasmonic nanoparticles.** In Chapter 2 we develop a simple analytical method to accurately calculate the optical response of plasmonic nanoparticles, in which retardation effects are taken into account through a perturbation manner. The plasmonic extinction spectra are described through a small set of real numbers that only depend on the shape of each nanoparticle.

  The analytical model is computationally efficient and can be readily applied to any plasmonic nanoparticle shape once the aforementioned parameters are provided. As a potential application for sensing, this method serves as an efficient tool to estimate the capability of monitoring changes in the dielectric environment through observed variations in the plasmonic response for a given nanoparticle morphology.

- **Light modulation with graphene.** In Chapter 3, we show that monolayer graphene, coupled to other optical resonators, can be used to produce unity-order changes in the transmission, reflection, and absorption of light in the vis-NIR domain through varying its doping level.

  The mechanisms considered here for light modulation using graphene are highly integratable. A device, based on these mechanisms, of only a few square microns in size, can operate under a relatively low doping load. Therefore, these systems are expected to be able to modulate visible-NIR (vis-NIR) light at a relatively high speed with minimal power consumption. Our findings open a new path for

the development of compact electro-optical components such as tunable vis-NIR light filters, switches, and sensors, which are appealing for micro integration and mass production.

- **Nanoscale thermal management with graphene.** In Chapter 4 we predict a fundamentally unique scenario: via non-contact heat transfer, the electronic thermal energy in one hotter object can efficiently transfer to the electrons in another colder object before it decays into phonons.

  We also show that high electron temperatures well above the lattice temperature can be obtained in clean graphene due to its characteristic weak electron-phonon coupling, which produces sizable plasmon frequency shifts in graphene ribbons because of the strong photothermal modulation. We further exploit this effect as an efficient way to spatially modulate the surface conductivity of an extended graphene sheet through a spatially patterned optical pump to locally heat graphene electrons, thus dynamically controlling its resulting optical response.

  Our findings are crucial for the design of nanoscale photothermal sources based on the use of graphene, with potential application in photothermal therapies and efficient non-contact cooling in nanosystems, such as nanoelectromechanical systems.

- **Light detection with graphene.** In Chapter 5 we show that a compact ballistic device based on a graphene nanojunction is capable of electrically detecting plasmons excited in its central graphene island with a sensitivity down to the single plasmon level. The conductivity of the junction is shown to be severely modified by the presence of graphene plasmons through optical heating.

  After scaling up the junction in size, we access the mid-infrared spectral region and demonstrate an extremely sub-wavelength device that can efficiently detect mid-infrared light and operate at room temperature. Our design therefore holds great potential for on-chip nanophotonic devices comprising photodetectors, spectrometers, and sensors, as well as for integrated quantum devices in view of its ability to resolve single plasmons.

- **Plasmonic sensing with graphene.** Finally, in Chapter 6 we demonstrate through atomistic quantum-mechanical simulations that nanographenes can serve as efficient optical sensors capable of detecting charge- and dipole-carrying analytes with single-molecule sensitivity.

  We find substantial changes in the linear optical absorption spectra induced by the presence of the analytes. Additionally, due to the external perturbation produced by the analyte, a strong second-harmonic signal arises even in centrosymmetric nanographenes. Our proposed scheme constitutes a completely

novel optical sensing approach and holds great potential for advancing the detectability of highly-integrated optical sensors.

Future nanophotonic devices shall go "fast" and "small". Since the 5G (fifth generation) era is coming, fast optical devices, such as light modulators, switches, and detectors, are highly desirable to meet the standard bandwidth of this new era. Additionally, wafer-scale integration of optical circuits/components is of great importance not only due to its ability to enhance the operation speed, but also to minimize the energy consumption of optical devices. Therefore, the combination of "fast" and "small" would trigger plenty of emerging and fascinating possibilities, ranging from on-chip optical sensors for monitoring swift bioreactions to smart optoelectronic navigators for the automatic drive control, nano-sized light sources for highly-integrated optical circuitry and subwavelength bio-imaging, as well as efficient passive radiative coolers for global energy conservation. In this regard, we hope our proposals presented in this thesis can serve as a helpful guidance for future nanophotonic devices.

APPENDICES

A

Analytical modeling of plasmonic nanoparticles

A.1 Electrostatic limit

Following the theoretical framework described in Section 1.2.1, in the electrostatic limit (*i.e.*, $c \to \infty$, when the incident light wavelength is much larger than the characteristic length of the nanostructure), Eq. 1.22 becomes

$$\mathscr{M}^{(0)}(\mathbf{r},\mathbf{r}') = \sqrt{f(\mathbf{r})f(\mathbf{r}')}\,\nabla\otimes\nabla\frac{1}{|\mathbf{r}-\mathbf{r}'|},$$

where $\mathscr{M}^{(0)}$ is a real symmetric operator that consequently admits an orthogonal set of real eigenmodes $\vec{\mathscr{E}}_j = \sqrt{f}\,\mathbf{E}_j$ and eigenvalues μ_j satisfying

$$\vec{\mathscr{E}}_j(\mathbf{r}) = \frac{1}{\mu_j}\int d^3\mathbf{r}'\,\mathscr{M}^{(0)}(\mathbf{r},\mathbf{r}')\cdot\vec{\mathscr{E}}_j(\mathbf{r}'), \tag{A.1}$$

$$\int d^3\mathbf{r}\,\vec{\mathscr{E}}_j(\mathbf{r})\cdot\vec{\mathscr{E}}_{j'}(\mathbf{r}) = L^3\delta_{jj'}, \tag{A.2}$$

$$\sum_j \vec{\mathscr{E}}_j(\mathbf{r})\otimes\vec{\mathscr{E}}_j(\mathbf{r}') = L^3\delta(\mathbf{r}-\mathbf{r}')\mathscr{I}_3. \tag{A.3}$$

The last expression (completeness relation) must be understood in the subspace of electrostatic fields (*i.e.*, irrotational and divergenceless vector distributions). These relations allow us to expand the solution of Eq. 1.21 in terms of electrostatic eigenmodes as

$$\mathbf{E}(\mathbf{r},\omega) = \sum_j \left[1 - \frac{\epsilon_\mathrm{m}/\epsilon_\mathrm{h} - 1}{\epsilon_j - 1}\right]^{-1} C_j^{\mathrm{ext}}(\omega)\mathbf{E}_j(\mathbf{r}) \tag{A.4}$$

with expansion coefficients

$$C_j^{\mathrm{ext}}(\omega) = \frac{1}{L^3}\int d^3\mathbf{r}\,f(\mathbf{r})\,\mathbf{E}_j(\mathbf{r})\cdot\mathbf{E}^{\mathrm{ext}}(\mathbf{r},\omega).$$

In Eq. A.4 we define the mode permittivity ϵ_j through the relation $\mu_j = 4\pi(\epsilon_j - 1)^{-1}$.

A.2 Perturbative solution including retardation

A direct extension of Eqs. A.1-A.4 permits us to express the general solution of Maxwell's equations in terms of k_h-dependent complex eigenmodes $\tilde{\vec{\mathscr{E}}}_j = \sqrt{f}\,\tilde{\mathbf{E}}_j$ and

eigenvalues $\tilde{\mu}_j$ of the symmetric operator $\mathscr{M}$, which satisfy

$$\tilde{\bar{\mathscr{E}}}_j(\mathbf{r}) = \frac{1}{\tilde{\mu}_j}\int d^3\mathbf{r}'\,\mathscr{M}(\mathbf{r},\mathbf{r}')\cdot\tilde{\bar{\mathscr{E}}}_j(\mathbf{r}'), \tag{A.5}$$

$$\int d^3\mathbf{r}\,\tilde{\bar{\mathscr{E}}}_j(\mathbf{r})\cdot\tilde{\bar{\mathscr{E}}}_{j'}(\mathbf{r}) = L^3\delta_{jj'},$$

$$\sum_j \tilde{\bar{\mathscr{E}}}_j(\mathbf{r})\otimes\tilde{\bar{\mathscr{E}}}_j(\mathbf{r}') = L^3\delta(\mathbf{r}-\mathbf{r}')\bar{\mathscr{I}}_3, \tag{A.6}$$

where the last expression (completeness) is valid in the subspace of divergenceless vector fields (*i.e.*, solutions satisfying the Coulomb law $\nabla\cdot\mathbf{E}$ inside the nanoparticle). The solution for the field now becomes

$$\mathbf{E}(\mathbf{r},\omega) = \sum_j \frac{\tilde{C}_j^{\mathrm{ext}}(\omega)}{1-(\epsilon_\mathrm{m}/\epsilon_\mathrm{h}-1)\tilde{\mu}_j/4\pi}\tilde{\mathbf{E}}_j(\mathbf{r}), \tag{A.7}$$

where

$$\tilde{C}_j^{\mathrm{ext}}(\omega) = \frac{1}{L^3}\int d^3\mathbf{r}\,f(\mathbf{r})\tilde{\mathbf{E}}_j(\mathbf{r})\cdot\mathbf{E}^{\mathrm{ext}}(\mathbf{r},\omega). \tag{A.8}$$

We intend to express the retarded eigenmodes and eigenvalues in terms of the electrostatic modes. For this purpose, we take $s = k_\mathrm{h}L/2\pi = \sqrt{\epsilon_\mathrm{h}}L/\lambda$ as a size parameter and write the perturbation expansion

$$\mathscr{M}(\mathbf{r},\mathbf{r}') = \mathscr{M}^{(0)}(\mathbf{r},\mathbf{r}') + \sum_{n=2}^{\infty}\mathscr{M}^{(n)}(\mathbf{r},\mathbf{r}'),$$

where we find the $n=1$ term to be zero, while the $n\geq 2$ terms are given by

$$\mathscr{M}^{(n)}(\mathbf{r},\mathbf{r}') = (i2\pi s)^n\sqrt{f(\mathbf{r})f(\mathbf{r}')}\,\frac{|\mathbf{r}-\mathbf{r}'|^{n-5}}{n(n-2)!}\left[(n-3)(\mathbf{r}-\mathbf{r}')\otimes(\mathbf{r}-\mathbf{r}') + (1-n)|\mathbf{r}-\mathbf{r}'|^2\bar{\mathscr{I}}_3\right].$$

One can use the expansion $\tilde{\mu}_j = \tilde{\mu}_j^{(0)} + \tilde{\mu}_j^{(1)} + \tilde{\mu}_j^{(2)} + \tilde{\mu}_j^{(3)} + \cdots$ for the eigenvalues and a similar one for the eigenmodes. After lengthy but straightforward algebra, we can express the eigenvalues ($n\geq 2$, note that $\tilde{\mu}_j^{(1)} = 0$ and $\tilde{\bar{\mathscr{E}}}_j^{(1)} = 0$) as

$$\tilde{\mu}_j = \mu_j + 4\pi A_j(s) = 4\pi\left[(\epsilon_j-1)^{-1} + A_j(s)\right] \tag{A.9}$$

with

$$A_j(s) = \sum_{n=2}^{\infty} a_{jn}s^n \tag{A.10}$$

and

$$a_{jn} = \frac{(2\pi \mathrm{i})^n}{4\pi n(n-2)!L^{n+3}} \int d^3\mathbf{r}\, f(\mathbf{r}) \int d^3\mathbf{r}'\, f(\mathbf{r}') \tag{A.11}$$
$$\times \left\{(n-3)|\mathbf{r}-\mathbf{r}'|^{n-5}\left[(\mathbf{r}-\mathbf{r}')\cdot\mathbf{E}_j(\mathbf{r})\right]\left[(\mathbf{r}-\mathbf{r}')\cdot\mathbf{E}_j(\mathbf{r}')\right] + (1-n)|\mathbf{r}-\mathbf{r}'|^{n-3}\mathbf{E}_j(\mathbf{r})\cdot\mathbf{E}_j(\mathbf{r}')\right\}.$$

In this expression, the retardation corrections of the eigenvalue j are entirely expressed in terms of the electrostatic mode with the same index j.

A.3 Light plane-wave scattering

We consider an incident plane wave propagating along z and polarized along x, which is taken to be a symmetry direction of the plasmonic nanoparticle. We can find, in the far-field limit (*i.e.*, $k_\mathrm{h} r \gg 1$ and $r \gg r'$), the induced dipole moment $\mathbf{p} = p_x \hat{\mathbf{x}}$ with

$$p_x = \frac{\epsilon_\mathrm{h} E_0}{4\pi L^3} \sum_j \frac{\left(\int d^3\mathbf{r}\, f(\mathbf{r})\, \tilde{E}_{jx}(\mathbf{r}) e^{\mathrm{i}k_\mathrm{h} z}\right)\left(\int d^3\mathbf{r}\, f(\mathbf{r})\, \tilde{E}_{jx}(\mathbf{r}) e^{-\mathrm{i}k_\mathrm{h} z}\right)}{1/(\epsilon_\mathrm{m}/\epsilon_\mathrm{h}-1) - 1/(\epsilon_j - 1) - A_j(s)}, \tag{A.12}$$

where we consider far-field emission along z as well. The numerator in this expression receives retardation corrections both from the mode fields $\tilde{E}_{jx}$ and from the phase factors $e^{\pm \mathrm{i}k_\mathrm{h} z}$. In practice, we can define the mode volume V_j as

$$V_j = \frac{1}{L^3}\left(\int d^3\mathbf{r}\, f(\mathbf{r})\, \tilde{E}_{jx}(\mathbf{r}) e^{\mathrm{i}k_\mathrm{h} z}\right)\left(\int d^3\mathbf{r}\, f(\mathbf{r})\, \tilde{E}_{jx}(\mathbf{r}) e^{-\mathrm{i}k_\mathrm{h} z}\right). \tag{A.13}$$

and immediately find the mode volume in the electrostatic limit as

$$V_j^0 = \frac{1}{L^3}\left|\int d^3\mathbf{r}\, f(\mathbf{r})\, E_{jx}(\mathbf{r})\right|^2. \tag{A.14}$$

This allows us to express the dipole $p_x = \alpha E_0$ in terms of the polarizability

$$\alpha(\omega) = \frac{\epsilon_\mathrm{h}}{4\pi} \sum_j \frac{V_j}{1/(\epsilon_\mathrm{m}/\epsilon_\mathrm{h}-1) - 1/(\epsilon_j - 1) - A_j(s)}. \tag{A.15}$$

Importantly, in virtue of the closure relation given by Eqs. A.3 and A.6, both the mode volumes defined in either retarded or electrostatic regime satisfy the sum rule $\sum_j V_j = V$ and $\sum_j V_j^0 = V$, where V is the total volume of the particle. Additionally, the a_{j3} coefficient (see Eq. A.11) can be expressed in terms of the corresponding mode volume.

After knowing the polarizability given in Eq. A.15, we can finally calculate the extinction, the scattering, and the absorption cross-sections following Eq. 1.13.

A.4 Two-dimensional limit: plasmon wave functions

In the two-dimensional limit, we intend to find the electric field **E** produced by a planar graphene structure in response to an impinging optical field $\mathbf{E}^{\text{ext}}$, expressing it in frequency domain ω as the solution of the self-consistent equation

$$\mathbf{E}(\mathbf{R},\omega) = \mathbf{E}^{\text{ext}}(\mathbf{R},\omega) + \frac{i\sigma(\omega)}{\omega\epsilon(\omega)}\nabla_{\mathbf{R}}\int \frac{d^2\mathbf{R}'}{|\mathbf{R}-\mathbf{R}'|}\nabla_{\mathbf{R}'}\cdot f\left(\mathbf{R}'\right)\mathbf{E}\left(\mathbf{R}',\omega\right). \tag{A.16}$$

Here, $\epsilon(\omega)$ is the average permittivity of the materials on either side of the graphene plane, while $f(\mathbf{R})$ is again the filling function that is 1 when the in-plane 2D position vector **R** lies within the graphene structure and 0 elsewhere (a vanishing positive number in practice). It should be noted that we are formulating the self-consistent electric field **E** in the graphene plane and the surface conductivity $\sigma(\omega)$ can be computed using either Drude or local-RPA models. Defining the normalized 2D in-plane vectors $\vec{\theta} \equiv \mathbf{R}/D$ and $\vec{\mathscr{E}}\left(\vec{\theta}\right) \equiv D\sqrt{f\left(\vec{\theta}\right)}\mathbf{E}\left(\vec{\theta},\omega\right)$, where D is a characteristic length of the geometry under consideration (*e.g.*, the side length of the graphene island), Eq. A.16 can be recast as

$$\vec{\mathscr{E}}\left(\vec{\theta}\right) = \vec{\mathscr{E}}^{\text{ext}}\left(\vec{\theta}\right) + \eta(\omega)\int d^2\vec{\theta}'\,\mathbf{M}(\vec{\theta},\vec{\theta}')\cdot\vec{\mathscr{E}}(\vec{\theta}'), \tag{A.17}$$

where $\eta(\omega) = i\sigma/(\omega D\epsilon)$ and

$$\mathbf{M}(\vec{\theta},\vec{\theta}') = \sqrt{f\left(\vec{\theta}\right)f\left(\vec{\theta}'\right)}\nabla_{\vec{\theta}}\otimes\nabla_{\vec{\theta}}\frac{1}{|\vec{\theta}-\vec{\theta}'|}$$

is a real and symmetric operator. In consequence, **M** admits a set of real eigenmodes $\vec{\mathscr{E}}_j\left(\vec{\theta}\right)$ and eigenvalues $1/\eta_j$ defined through

$$\vec{\mathscr{E}}_j(\vec{\theta}) = \eta_j\int d^2\vec{\theta}'\,\mathbf{M}(\vec{\theta},\vec{\theta}')\cdot\vec{\mathscr{E}}_j(\vec{\theta}'), \tag{A.18}$$

such that the eigenmodes satisfy the orthogonality condition

$$\int d^2\vec{\theta}\;\vec{\mathscr{E}}_j(\vec{\theta})\cdot\vec{\mathscr{E}}_{j'}(\vec{\theta}) = \delta_{jj'} \tag{A.19}$$

and the closure relation

$$\sum_j \vec{\mathscr{E}}_j(\vec{\theta})\otimes\vec{\mathscr{E}}_j(\vec{\theta}') = \delta(\vec{\theta}-\vec{\theta}')\mathscr{I}_2,$$

where $\mathscr{I}_2$ denotes the 2×2 identity matrix in the sub-space of quasistatic electric-field solutions. Using the above eigenmodes, we write the solution to Eq. A.17 as

$$\vec{\mathscr{E}}(\vec{\theta},\omega)=\sum_j \frac{C_j}{1-\eta(\omega)/\eta_j}\vec{\mathscr{E}}_j(\vec{\theta}),$$

where the expansion coefficients are given by

$$C_j=\int d^2\vec{\theta}\;\vec{\mathscr{E}}_j(\vec{\theta})\cdot\vec{\mathscr{E}}^{\text{ext}}(\vec{\theta},\omega). \tag{A.20}$$

From the closure relation, we have $\vec{\mathscr{E}}^{\text{ext}}(\vec{\theta},\omega)=\sum_j C_j(\omega)\,\vec{\mathscr{E}}_j(\vec{\theta})$, which allows us to express the induced field as

$$\vec{\mathscr{E}}^{\text{ind}}(\vec{\theta},\omega)=\sum_j \frac{C_j}{\eta_j/\eta(\omega)-1}\vec{\mathscr{E}}_j(\vec{\theta}).$$

We now define the plasmon wave function (PWF)

$$\rho_j(\vec{\theta})\equiv\nabla_{\vec{\theta}}\cdot\sqrt{f(\vec{\theta})}\vec{\mathscr{E}}_j(\vec{\theta}), \tag{A.21}$$

which corresponds to the induced charge distribution of the plasmon eigenmode j. Using the continuity equation along with Eq. A.16, we can write the induced charge density ρ^{ind} as

$$\rho^{\text{ind}}(\vec{\theta},\omega)=\frac{\epsilon}{D}\sum_j \frac{C_j}{1/\eta_j-1/\eta(\omega)}\rho_j(\vec{\theta}). \tag{A.22}$$

Now, for a uniform electric field $\mathbf{E}^{\text{ext}}$ associated with a light plane wave that acts on the graphene structure (we remind that D is small compared with the light wavelength so we can neglect the propagation phase in the incident field), we find, upon an integration of Eq. A.20 by parts, $C_j=-\vec{\zeta}_j\cdot\mathbf{E}^{\text{ext}}$, where

$$\vec{\zeta}_j=\int d^2\vec{\theta}\rho_j(\vec{\theta})\vec{\theta} \tag{A.23}$$

is a parameter that plays the role of the mode dipole moment. From the induced charge density, we calculate the induced dipole moment as

$$\mathbf{p}^{\text{ind}}(\omega)=D^3\int d^2\vec{\theta}\;\rho^{\text{ind}}(\vec{\theta},\omega)\;\vec{\theta},$$

while comparing the above expression with the definition of the polarizability $\mathbf{p}^{\text{ind}}(\omega) = \alpha(\omega)\cdot\mathbf{E}^{\text{ext}}$ and using Eq. A.22, we obtain the 2×2 in-plane polarizability tensor $\alpha(\omega)$,

$$\alpha(\omega) = \epsilon D^3 \sum_j \frac{\vec{\zeta}_j \otimes \vec{\zeta}_j}{1/\eta(\omega) - 1/\eta_j}. \tag{A.24}$$

Finally, we can calculate the extinction, the scattering, and the absorption cross-sections following Eq. 1.13 as in the previous section.

In this thesis, we also consider the decay rate Γ of a unit dipole $\mathbf{p}^{\text{ext}}$ oscillating at frequency ω and located at the position $\mathbf{r}$ in an inhomogeneous space (*e.g.*, in the presence of a graphene nanostructure), which is given by[232]

$$\Gamma = \Gamma_0 + \frac{2}{\hbar}\text{Im}\left\{\left(\mathbf{p}^{\text{ext}}\right)^*\cdot\mathbf{E}^{\text{ind}}\right\}, \tag{A.25}$$

where $\Gamma_0 = 4\omega^3\left|\mathbf{p}^{\text{ext}}\right|^2/3c^3\hbar$ is the dipole decay rate in free space. We evaluate this expression in the presence of a graphene island by integrating the induced charge (Eq. A.22) weighted by the Coulomb interaction to yield the induced electric field

$$\mathbf{E}^{\text{ind}}(\mathbf{r},\omega) = -\nabla_{\mathbf{r}}\int d^2\mathbf{R}'\frac{\rho^{\text{ind}}(\mathbf{R}'/D,\omega)}{|\mathbf{r}-\mathbf{R}'|}$$

evaluated at an arbitrary position $\mathbf{r}$ from the PWF defined on the graphene island.

B

The fluctuation-dissipation theorem

We provide a brief derivation of the fluctuation-dissipation theorem (FDT)[69,70] for fluctuations of the charge density in the frequency domain $\rho^{\mathrm{fl}}(\mathbf{r},\omega)$. We start by considering a system characterized by its charge density $\rho(\mathbf{r},t)$ and described through the Hamiltonian $H = H_0 + H_1$, where H_0 is the unperturbed term, while

$$H_1 = \int d^3\mathbf{r}\,\rho(\mathbf{r},t)\phi(\mathbf{r},t)$$

accounts for the time-dependent interaction between ρ and an external electric potential $\phi(\mathbf{r},t)$. Using first-order perturbation theory under the assumption that H_1 vanishes in the $t \to -\infty$ limit, we can write the eigenstates of the perturbed system as

$$|\psi_m(t)\rangle \approx |m\rangle - \frac{i}{\hbar}\int_{-\infty}^{t} dt'\, H_1(t')\,|m\rangle\,,$$

where $|m\rangle$ is the eigenstate of H_0 with energy E_m (i.e., $H_0\,|m\rangle = E_m\,|m\rangle$). Summing the contributions from all perturbed states $|\psi_m(t)\rangle$, we obtain the expectation value of the charge density induced by H_1 as

$$\begin{aligned}
\langle\rho^{\mathrm{ind}}(\mathbf{r},t)\rangle &= \langle\rho(\mathbf{r},t)\rangle - \langle\rho(\mathbf{r},-\infty)\rangle \\
&= -\frac{i}{\hbar}\int_{-\infty}^{t} dt' \int d^3\mathbf{r} \sum_m \frac{\mathrm{e}^{-E_m/k_BT}}{Z}\,\langle m|\big[\rho(\mathbf{r},t),\rho(\mathbf{r}',t')\big]|m\rangle\,\phi(\mathbf{r}',t') \\
&= -\frac{i}{\hbar}\int_{-\infty}^{t} dt' \int d^3\mathbf{r}\,\chi(\mathbf{r},\mathbf{r}',t')\phi(\mathbf{r}',t'),
\end{aligned}$$

where $Z = \sum_m \mathrm{e}^{-E_m/k_BT}$ is the partition function at temperature T, while $\chi(\mathbf{r},\mathbf{r}',t')$ is the electric susceptibility of the system. The latter can be expressed in the frequency domain by taking the Fourier transform of the above expressions:

$$\chi(\mathbf{r},\mathbf{r}',\omega) = \int dt\;\chi(\mathbf{r},\mathbf{r}',t)\mathrm{e}^{i\omega t} = \frac{1}{Z}\sum_{m,n}\langle m|\,\rho(\mathbf{r})\,|n\rangle\,\langle n|\,\rho(\mathbf{r}')\,|m\rangle\,\frac{\mathrm{e}^{-E_m/k_BT}-\mathrm{e}^{-E_n/k_BT}}{\hbar\omega+E_m-E_n+i0^+}, \tag{B.1}$$

where we have used $\rho(\mathbf{r},t) = \mathrm{e}^{iH_0t/\hbar}\rho(\mathbf{r})\mathrm{e}^{-iH_0t/\hbar}$ as well as the closure relation $\sum_n |n\rangle\langle n| = \mathscr{I}$.

At this point, we follow a similar procedure for calculating the self correlations of the fluctuating charge density $\rho^{\mathrm{fl}}(\mathbf{r},\omega)$. We find

$$\begin{aligned}
\langle\rho^{\mathrm{fl}}(\mathbf{r},\omega)\rho^{\mathrm{fl}}(\mathbf{r}',\omega')\rangle &= \int dt dt'\,\mathrm{e}^{i\omega t}\mathrm{e}^{i\omega' t'}\,\langle\rho^{\mathrm{fl}}(\mathbf{r},t)\rho^{\mathrm{fl}}(\mathbf{r}',t')\rangle \\
&= \frac{1}{Z}\int dt dt'\,\mathrm{e}^{i\omega t}\mathrm{e}^{i\omega' t'}\sum_{m,n}\mathrm{e}^{-E_m/k_BT}\mathrm{e}^{i(E_m-E_n)(t-t')/\hbar}\,\langle m|\,\rho(\mathbf{r})\,|n\rangle\,\langle n|\,\rho(\mathbf{r}')\,|m\rangle \\
&= 2\pi\delta(\omega+\omega')S(\omega),
\end{aligned}$$

where

$$S(\omega) = \frac{2\pi\hbar}{Z} \sum_{m,n} \mathrm{e}^{-E_m/k_B T} \langle m| \rho(\mathbf{r}) |n\rangle \langle n| \rho(\mathbf{r}') |m\rangle \, \delta(\hbar\omega + E_m - E_n).$$

Comparing this expression with Eq. B.1, we obtain $S(\omega) = -2\hbar\,[n(\omega)+1]\,\mathrm{Im}\{\chi(\mathbf{r},\mathbf{r}',\omega)\}$, where $n(\omega) = [\mathrm{e}^{\hbar\omega/k_B T} - 1]^{-1}$ is the Bose-Einstein distribution function. We conclude that

$$\langle \rho^{\mathrm{fl}}(\mathbf{r},\omega)\rho^{\mathrm{fl}}(\mathbf{r}',\omega')\rangle = -4\pi\hbar\delta(\omega+\omega')\,[n(\omega)+1]\,\mathrm{Im}\{\chi(\mathbf{r}',\mathbf{r},\omega)\}.$$

Additionally, interchanging $\rho^{\mathrm{fl}}(\mathbf{r},\omega)$ and $\rho^{\mathrm{fl}}(\mathbf{r}',\omega')$, we have

$$\langle \rho^{\mathrm{fl}}(\mathbf{r},\omega)\rho^{\mathrm{fl}}(\mathbf{r}',\omega')\rangle = -4\pi\hbar\delta(\omega+\omega')\,n(\omega)\,\mathrm{Im}\{\chi(\mathbf{r}',\mathbf{r},\omega)\}.$$

Finally, noting that $\chi(\mathbf{r},\mathbf{r}',\omega) = \chi(\mathbf{r}',\mathbf{r},\omega)$, the expectation value of the physically meaningful symmetrized correlation becomes

$$\begin{aligned}\langle \rho^{\mathrm{fl}}(\mathbf{r}',\omega')\rho^{\mathrm{fl}}(\mathbf{r},\omega)\rangle_{\mathrm{sym}} &= \frac{1}{2}\big[\langle \rho^{\mathrm{fl}}(\mathbf{r},\omega)\rho^{\mathrm{fl}}(\mathbf{r}',\omega')\rangle + \langle \rho^{\mathrm{fl}}(\mathbf{r}',\omega')\rho^{\mathrm{fl}}(\mathbf{r},\omega)\rangle\big] \\ &= -4\pi\hbar\delta(\omega+\omega')\,[n(\omega)+\frac{1}{2}]\,\mathrm{Im}\{\chi(\mathbf{r}',\mathbf{r},\omega)\}.\end{aligned}$$

This is the FDT used in Eq. 1.59 in Section 1.4.3, where we drop the 'sym' subscript for clarity.

C

Model parameters for various additional particle morphologies

	ϵ_1	V_1/V	a_{12}	a_{14}
ellipsoid	-0.871 $-1.35R^{1.54}$	0.994	$5.52/(1-\epsilon_1)$	$-9.75/R^{2.53}$
bicone	-0.687 $-2.54R^{1.5}$	0.648 $-0.441/R^{0.687}$	$1.34/(1-\epsilon_1)$	$1.04/(\epsilon_1-1)$
disk	-0.479 $-1.36R^{0.872}$	0.944	$7.05/(1-\epsilon_1)$	$-10.9/R^{0.98}$
ring	1.39 $-1.31R^{1.73}$	0.514 $+2.07/R^{2.67}$	$7.24/(1-\epsilon_1)$	$19.1/(\epsilon_1-1)$
bipyramid	1.43 $-4.52R^{1.12}$	1.96 $-1.73/R^{0.207}$	$2.89/(1-\epsilon_1)$	$1.79/(\epsilon_1-1)$
squared rod	-2.28 $-1.47R^{1.49}$	0.904 $-0.411/R^{2.26}$	-0.573 $+3.31/R^{0.747}$	0.213 $-13.1/R^{1.97}$
cylinder	-1.59 $-1.96R^{1.4}$	0.883 $-0.149/R^{3.97}$	-1.05 $+3.02/R^{0.494}$	0.0796 $-9.08/R^{2.08}$

Table C.1: Fitting functions for the parameters considered in Fig. C.1.

Following the description in Section 2.2, here we present the resonant permittivities ϵ_j found by fitting the position and strength of the peak associated with mode j in the absorption spectrum of the particle, the mode volume V_j from Eq. 2.2, and a_{j2} and a_{j4} from Eq. 2.5 in Fig. C.1 for seven morphologies (in addition to the ones shown in Fig. 2.1), as a function of aspect ratio R (see upper insets). We also provide analytical R-dependent fits in Table C.1.

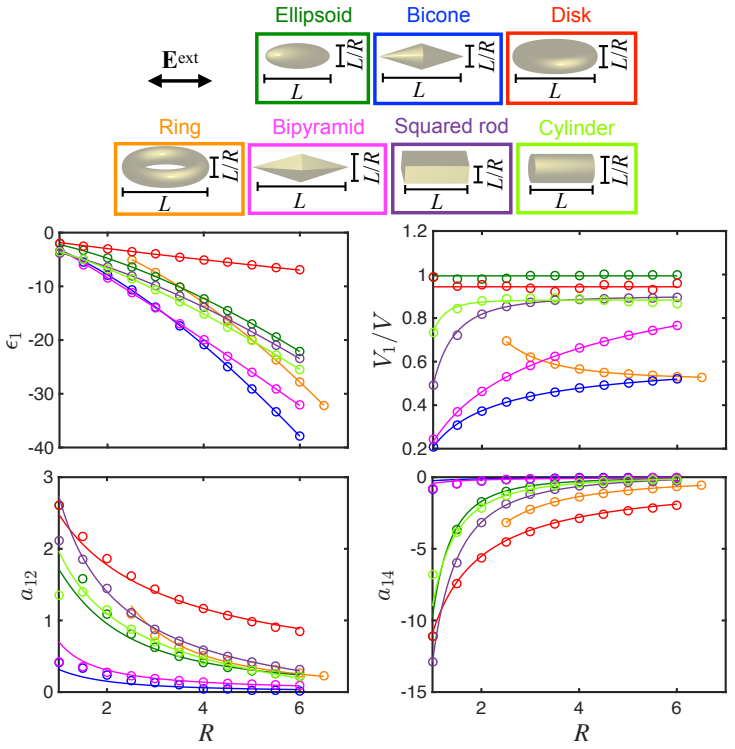

Figure C.1: **Model parameters for various additional particle morphologies.** We show the resonant in-vacuum permittivity ϵ_1, the mode volume V_1, and two of the expansion coefficients a_{jn} in Eq. 2.4, as a function of aspect ratio R, for the lowest-order dipole mode ($j = 1$) of five selected morphologies (see upper insets). Symbols: ϵ_1 values extracted by fitting the corresponding absorption spectra (computed in the electrostatic limit), V_1 values calculated from Eq. 2.2, and a_{12} and a_{14} values obtained from Eq. 2.5. Solid curves: analytical fitting functions given in Table C.1. Symbol and curve colors correspond to the different shapes of the upper insets.

D

Plasmon wave functions for graphene disks

D.1 Description of graphene islands through plasmon wave functions (PWFs)

Here, we apply the plasmon wave function (PWF) formalism to two parallel graphene islands placed in a homogeneous medium of permittivity ϵ and separated by a vertical distance $d = |z_\ell - z_{\ell'}|$ along their normal direction z. It is then convenient to use an eigenmode expansion for the response of each island ℓ.[99,100] This allows us to define a complete set of PWFs $\rho_{\ell j}$ and real eigenvalues $\eta_{\ell j}$, where j is a mode index. More precisely, the susceptibility of the ℓ island, taking to be in the $z = z_\ell$ plane, admits the rigorous exact expansion[99]

$$\chi_\ell(\mathbf{r},\mathbf{r}',\omega) = \frac{\epsilon}{D_\ell^3}\sum_j \frac{\rho_{\ell j}(\vec{\theta})\rho_{\ell j}(\vec{\theta}')}{1/\eta_{\ell j} - 1/\eta^{(\ell)}(\omega)}\,\delta(z-z_\ell)\delta(z'-z_\ell), \tag{D.1}$$

where j runs over eigenmodes, we use the notation $\mathbf{r} = (D_\ell\vec{\theta}, z)$, $\vec{\theta}$ is an in-plane coordinate vector normalized to a characteristic length of the structure D_ℓ (we use the diameter for disks), and

$$\eta^{(\ell)}(\omega) = \frac{\mathrm{i}\sigma_\ell(\omega)}{\epsilon\,\omega D_\ell} \tag{D.2}$$

incorporates the response of the graphene through its local conductivity $\sigma_\ell(\omega)$. It should be noted that the latter depends on ℓ via the level of doping and the temperature (see below). The PWFs and their eigenvalues satisfy the orthogonality relation[99]

$$\int d^2\vec{\theta}\int d^2\vec{\theta}'\,\frac{\rho_{\ell j}(\vec{\theta})\rho_{\ell j'}(\vec{\theta}')}{|\vec{\theta}-\vec{\theta}'|} = -\frac{\delta_{jj'}}{\eta_{\ell j}}. \tag{D.3}$$

For islands with the same geometrical shape (*e.g.*, disks), the PWFs and eigenvalues are independent of size D_ℓ, even if $D_1 \neq D_2$.

We can readily use Eq. D.1 to evaluate the heat transfer rate according to Eq. 1.61. With some straightforward redefinitions, these equations remain the same, but now the coefficients of the matrices that they contain are labeled by eigenmode indices j instead of spatial coordinates $\mathbf{r}$. More precisely, χ_ℓ becomes a diagonal matrix of coefficients

$$\chi_{\ell,jj'} = \delta_{jj'}\,\frac{\epsilon}{D_\ell^3}\frac{1}{1/\eta_{\ell j} - 1/\eta^{(\ell)}},$$

while the matrix elements of the Coulomb interaction reduce to

$$v_{jj'} = \frac{D_\ell^2 D_{\ell'}^2}{\epsilon}\int d^2\vec{\theta}\int d^2\vec{\theta}'\,\frac{\rho_{\ell j}(\vec{\theta})\rho_{\ell' j'}(\vec{\theta}')}{\sqrt{|D_\ell\vec{\theta} - D_{\ell'}\vec{\theta}'|^2 + d^2}} \tag{D.4}$$

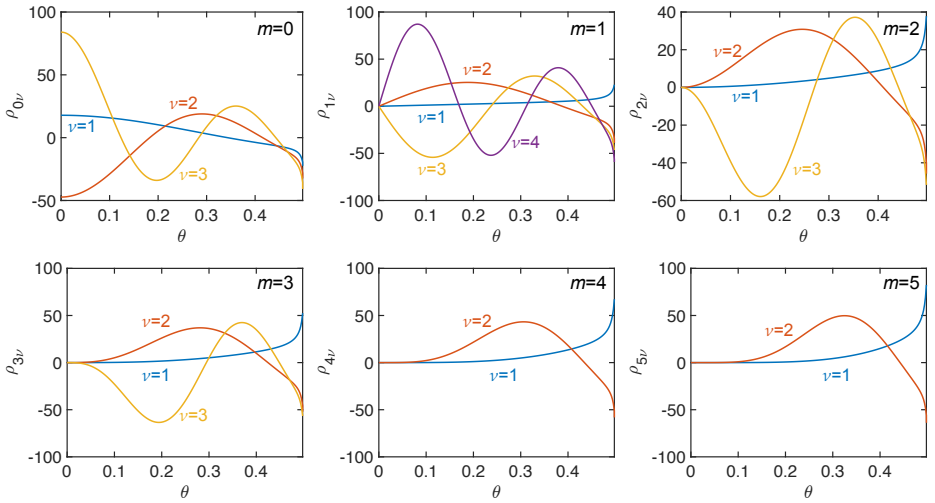

Figure D.1: **Radial components of the disk PWFs.** We show $\rho_{m\nu}(\theta)$ as defined in Eqs. D.6 for several low values of m and ν (see also Table D.1).

when the operators to the left and right of v are referred to islands ℓ and ℓ', respectively. Incidentally, in this work we focus on disk dimers that share the same axis of symmetry; an eventual lateral displacement **b** between the islands is however easy to implement by adding it to $D_\ell\vec{\theta} - D_{\ell'}\vec{\theta}'$ in the above expression.

In this PWF formalism, inserting Eq. D.1 into Eq. 1.63, we find that the polarizability of a graphene island along a given in-plane symmetry direction x is given by

$$\alpha_\ell(\omega) = \epsilon D_\ell^3 \sum_j \frac{\zeta_j^2}{1/\eta^{(\ell)} - 1/\eta_j}, \tag{D.5}$$

where $\zeta_j = \int \theta_x \, d^2\vec{\theta}\rho_j(\vec{\theta})$ is a normalized plasmon dipole moment.

D.2 PWFs for disks

In the disk geometry, the azimuthal number m provides a natural way of classifying the PWFs. More precisely, we can label them using a double index $(m\,\nu)$ and separate the radial and azimuthal dependences as

$$\rho^{\mathrm{c}}_{m\nu}(\vec{\theta}) = \rho_{m\nu}(\theta)\cos(m\varphi_{\vec{\theta}}), \quad (m \geq 0), \tag{D.6a}$$

$$\rho^{s}_{m\nu}(\vec{\theta}) = \rho_{m\nu}(\theta)\sin(m\varphi_{\vec{\theta}}), \quad (m \geq 1). \tag{D.6b}$$

We insist that these PWFs are the same for both disks in a dimer, as they are independent of disk size, and therefore, we drop the disk index ℓ for them. We also note that the PWFs are doubly degenerate for $m > 0$ (*i.e.*, they share the same eigenvalue $\eta_{m\nu}$ and radial component $\rho_{m\nu}(\theta)$ for both sine and cosine azimuthal dependences). We obtain the radial component $\rho_{m\nu}(\theta)$ by solving the Maxwell equations numerically using the boundary-element method[94] (BEM) for a self-standing disk of small thickness $t \sim D/300$ compared with its diameter D. The disk is described by a dielectric function $\epsilon = 1 + 4\pi i\sigma/\omega t$, where σ is the Drude graphene conductivity (the actual model used for σ is irrelevant, as the PWFs depend only on geometry and not on the specifics of the material). In the limit of small damping, the plasmons emerge as sharp, spectrally-isolated features in the local density of optical states (LDOS).[213] We average the LDOS over a set of off-center locations in order to access different m's efficiently. The radial components of the PWFs are then retrieved from the induced charge density, while the eigenvalues are derived from the resonance condition $\eta_{m\nu} = \mathrm{Re}\{i\sigma/\omega D\}$ at the corresponding LDOS peak maximum.

By construction, $\rho^{c}_{m\nu}$ and $\rho^{s}_{m\nu}$ (see Eqs. D.6) are mutually orthogonal according to Eq. D.3. Additionally, PWFs with different m's are automatically orthogonal. For the remaining pairs of wave functions that share both the value of m and the azimuthal dependence (either sine or cosine), Eq. D.3 reduces to

$$-4\pi\sqrt{\eta_{m\nu}\eta_{m\nu'}}\int_0^{1/2}\theta\, d\theta\, \rho_{m\nu}(\theta)\int_0^{1/2}\theta' d\theta'\, \rho_{m\nu'}(\theta') \times \int_0^{\pi} d\varphi\, \frac{\cos(m\varphi) - (1/2)\delta_{m,0}}{\sqrt{\theta^2 + \theta'^2 - 2\theta\theta'\cos\varphi}} = \delta_{\nu\nu'}. \tag{D.7}$$

Our calculated radial PWFs, already normalized according to Eq. D.7, are shown in Fig. D.1 for the lowest values of $(m\nu)$, while their associated eigenvalues are given in Table D.1. The orthogonality for $\nu \neq \nu'$ is rather satisfactory, as illustrated in Table

ν \ m	0	1	2	3	4	5
1	0.0234	0.0720	0.0402	0.0283	0.0220	0.0181
2	0.0123	0.0165	0.0130	0.0109	0.0094	0.0083
3	0.0084	0.0101	0.0086	0.0076		
4		0.0073				

Table D.1: We list the values of $-\eta_{m\nu}$ corresponding to the disk PWFs $\rho_{m\nu}$ considered in Fig. D.1 (see Eqs. D.6).

ν \ ν'	$m=0$		$m=1$			$m=2$	
	1	2	1	2	3	1	2
2	0.008	1	0.055	1		0.058	1
3	0.006	0.010	0.114	0.031	1	0.113	0.028
4			0.078	0.019	0.026		

ν \ ν'	$m=3$		$m=4$	$m=5$
	1	2	1	1
2	0.061	1	0.063	0.064
3	0.114	0.026		
4				

Table D.2: Each entry in these tables is obtained by first numerically integrating the left-hand side of Eq. D.7 and then take the absolute value. The values of m, ν, and ν' cover the ranges considered in Fig. D.1 and Table D.1. All diagonal entries ($\nu = \nu'$) are 1 by construction. We only show $\nu \geq \nu'$ values because the results are invariant under exchange of these two indices.

D.2, which shows the values obtained by numerically evaluating the left-hand side of Eq. D.7.

Upon insertion of the disk PWFs in Eq. D.4, we find that $v_{jj'}$ is diagonal by blocks (two blocks per m, corresponding to the two different azimuthal symmetries of Eqs. D.6 and each of them contributing the same to the HTP). As $\chi_{\ell,jj'}$ is diagonal, this allows us to write P_2 as a sum over m's, essentially reflecting the fact that only modes of the same symmetry undergo mutual Coulomb interaction. The integrand of Eq. 1.61 then becomes an analytical function, except for the integral over radial wave functions in $v_{jj'}$. We finally write Eq. 4.1 for the HTP, where the explicit dependence of the involved matrices on m is indicated.

Only $m = 1$ PWFs exhibit nonzero dipole moments ζ_ν contributing to the polarizability α_ℓ in Eq. D.5. More precisely, we obtain $\zeta_\nu^2 = 0.709$, 0.023, 0.012, and 0.006 for $\nu = 1-4$, respectively, whose sum is only 5% below the exact full sum for a disk, $\sum_\nu \zeta_\nu^2 = \pi/4$[38] (this discrepancy can be attributed in part to the contribution of $\nu > 4$ modes, as well as numerical uncertainties in dealing with thin disks). We use these coefficients and Eq. D.5 to obtain the absorption cross-section as $(4\pi\omega/c)\mathrm{Im}\{\alpha_\ell\} - (8\pi\omega^4/3c^4)|\alpha_\ell|^2$, where the second term ($\propto |\alpha_\ell|^2$) is negligible for the small diameters of the disks under consideration ($\ll$ light wavelength).

E

Transmission function in the Landauer formalism

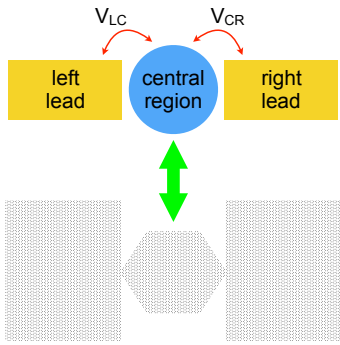

Figure E.1: Schematics of the graphene hexagon quantum dot (GHQD) junction, consisting of a finite central region coupled to two semi-infinite leads via the potentials V_{LC} and V_{CR}.

Following the structure displayed in Fig. 5.1, it is natural to divide the system into three parts as shown in Fig. E.1. We denote the Hamiltonian of the isolated central region as $\hat{H}_{\mathrm{C}}$ and the Hamiltonians of the left and right semi-infinite graphene sheets (*i.e.*, the leads) as $\hat{H}_{\mathrm{L}}$ and $\hat{H}_{\mathrm{R}}$, respectively. The couplings between the central region and the leads are described by potentials $\hat{V}_{\mathrm{LC}}$ and $\hat{V}_{\mathrm{CR}}$, respectively, as indicated in Fig. E.1. With these definitions, the total Hamiltonian

$$\hat{H}_{\mathrm{S}} = \hat{H}_{\mathrm{C}} + \hat{H}_{\mathrm{L}} + \hat{H}_{\mathrm{R}} + \hat{V}_{\mathrm{LC}} + \hat{V}_{\mathrm{CR}} + \hat{V}_{\mathrm{LC}}^{\dagger} + \hat{V}_{\mathrm{CR}}^{\dagger}. \tag{E.1}$$

permits us to write the Schrödinger equation in matrix form as[185,186]

$$\begin{bmatrix} \hat{H}_{\mathrm{L}} & \hat{V}_{\mathrm{LC}} & 0 \\ \hat{V}_{\mathrm{LC}}^{\dagger} & \hat{H}_{\mathrm{C}} & \hat{V}_{\mathrm{CR}}^{\dagger} \\ 0 & \hat{V}_{\mathrm{CR}} & \hat{H}_{\mathrm{R}} \end{bmatrix} \begin{bmatrix} |\phi_{\mathrm{L}}\rangle \\ |\phi_{\mathrm{C}}\rangle \\ |\phi_{\mathrm{R}}\rangle \end{bmatrix} = E \begin{bmatrix} |\phi_{\mathrm{L}}\rangle \\ |\phi_{\mathrm{C}}\rangle \\ |\phi_{\mathrm{R}}\rangle \end{bmatrix}, \tag{E.2}$$

where $|\phi_{\mathrm{L}}\rangle$, $|\phi_{\mathrm{C}}\rangle$, and $|\phi_{\mathrm{R}}\rangle$ are the single-particle wave functions associated with the Hamiltonians of each of the three regions. Equation E.2 readily leads to

$$\left(E\hat{I} - \hat{H}_{\mathrm{L}}\right)|\phi_{\mathrm{L}}\rangle = \hat{V}_{\mathrm{LC}}\,|\phi_{\mathrm{C}}\rangle\,, \tag{E.3}$$

$$\hat{V}_{\mathrm{LC}}^{\dagger}\,|\phi_{\mathrm{L}}\rangle + \hat{H}_{\mathrm{C}}\,|\phi_{\mathrm{C}}\rangle + \hat{V}_{\mathrm{CR}}^{\dagger}\,|\phi_{\mathrm{R}}\rangle = E\,|\phi_{\mathrm{C}}\rangle\,, \tag{E.4}$$

and

$$\left(E\hat{I} - \hat{H}_{\mathrm{R}}\right)|\phi_{\mathrm{R}}\rangle = \hat{V}_{\mathrm{CR}}\,|\phi_{\mathrm{R}}\rangle\,, \tag{E.5}$$

We can recast Eq. E.3 into

$$|\phi_{\mathrm{L}}\rangle = \hat{G}_{\mathrm{L}}^{\pm}\hat{V}_{\mathrm{LC}}\,|\phi_{\mathrm{C}}\rangle\,, \tag{E.6}$$

where $\hat{G}_{\rm L}^{\pm} = \left(E \pm i\epsilon - \hat{H}_{\rm L}\right)^{-1}$ are the retarded (+) and advanced (−) Green functions of the left lead, and $\epsilon \to 0^+$ is a positive infinitesimal. Similarly, from Eq. E.5,

$$|\phi_{\rm R}\rangle = \hat{G}_{\rm R}^{\pm}\hat{V}_{\rm CR}\,|\phi_{\rm C}\rangle\,. \tag{E.7}$$

For simplicity, we assume the Green functions to be diagonal and given by $\hat{G}_{L,R}^{\pm} = -i\pi\,\hat{I}$ times the density of states of the leads,[179] given in Eq. 5.3. We now substitute Eqs. E.3 and E.7 into Eq. E.4 to obtain

$$\left[E\hat{I} - \hat{H}_{\rm C} - \hat{V}_{\rm LC}^{\dagger}\hat{G}_{\rm L}^{\pm}\hat{V}_{\rm LC} - \hat{V}_{\rm CR}^{\dagger}\hat{G}_{\rm R}^{\pm}\hat{V}_{\rm CR}\right]|\phi_{\rm C}\rangle = 0. \tag{E.8}$$

It is then convenient to define self-energy operators

$$\hat{\Sigma}_{\rm L}^{\pm} = \hat{V}_{\rm LC}^{\dagger}\hat{G}_{\rm L}^{\pm}\hat{V}_{\rm LC} \tag{E.9}$$

and

$$\hat{\Sigma}_{\rm R}^{\pm} = \hat{V}_{\rm CR}^{\dagger}\hat{G}_{\rm R}^{\pm}\hat{V}_{\rm CR}, \tag{E.10}$$

in terms of which the retarded (+) and advanced (−) Green functions of the central region in the presence of the leads (*i.e.*, the Green functions of Eq. E.8) reduce to

$$\hat{G}^{\pm} = \left(E\hat{I} - \hat{H}_{\rm C} - \hat{\Sigma}_{\rm L}^{\pm} - \hat{\Sigma}_{\rm R}^{\pm}\right)^{-1}. \tag{E.11}$$

Finally, the transmission function (from left to right) can be formulated as[185,186]

$$T(E,V) = {\rm Tr}\left(\hat{\Gamma}_{\rm L}\hat{G}^{+}\hat{\Gamma}_{\rm R}\hat{G}^{-}\right) \tag{E.12}$$

with $\hat{\Gamma}_{\rm L,R} = i\left(\hat{\Sigma}_{\rm L,R}^{+} - \hat{\Sigma}_{\rm L,R}^{-}\right)$.

In order to calculate the transmission function, we write the GHQD Hamiltonian as

$$\hat{H}_{\rm C} = \hat{H}_{\rm TB} + \hat{H}_{\rm Hartree} + \hat{V}_{\rm bias}, \tag{E.13}$$

where $\hat{H}_{\rm TB}$ is the nearest-neighbors tight-binding Hamiltonian for graphene,[33,53] $\hat{H}_{\rm Hartree}$ is the self-consistent Hartree interaction among conduction electrons (see below), and the $\hat{V}_{\rm bias}$ term represents the potential produced by the bias, which for simplicity we assume to vary linearly across the gap separating the two gates.

Note that we project the operators using the carbon-site (discrete-space) representation. Specifically, we express the Hartree term as

$$\hat{H}_{\rm Hartree} = 2\sum_{jl'} v_{ll'} f_{T_{\rm e}}(E_j)\,|\,a_{jl'}\,|^2\,. \tag{E.14}$$

in terms of the one-electron wave function coefficients a_{jl} in the carbon-site representation[23,224] (see Section 1.3.1), the Coulomb interaction between carbon sites

$\nu_{ll'}$, and the Fermi-Dirac distribution $f_{T_e}(E_j) = \left\{1 + \exp\left[\left(E_j - \mu\right)/k_B T_e\right]\right\}^{-1}$, which gives the occupancy of each state j as a function of its energy E_j. The leading factor of 2 in Eq. E.14 stems from spin degeneracy. The Fermi-Dirac distribution depends on the electron temperature T_e in the GHQD, given in Eq. 5.1, and the T_e-dependent chemical potential μ, which is determined from the condition that the total number of electrons is conserved.

List of publications and conference contributions

The research performed in this thesis period has led to the following publications and conference contributions:

Articles on which this thesis is based

1. **Efficient electrical detection of mid-infrared graphene plasmons at room temperature**.
   Q. Guo*, R. Yu*, C. Li, S. Yuan, B. Deng, F. J. García de Abajo, and F. Xia.
   Nature Materials **17**, 986-992 (2018).
   * Equal contribution
2. **Photothermal Engineering of Graphene Plasmons**.
   R. Yu, Q. Guo, F. Xia, and F. J. García de Abajo.
   Physical Review Letters **121**, 057404 (2018).
3. **Analytical Modeling of Graphene Plasmons**.
   R. Yu, J. D. Cox, J. R. M. Saavedra, and F. J. García de Abajo.
   ACS Photonics **4**, 3106-3114 (2017).
4. **Universal analytical modeling of plasmonic nanoparticles**.
   R. Yu, L. M. Liz-Marzán, and F. J. García de Abajo.
   Chemical Society Reviews **46**, 6710-6724 (2017).
5. **Ultrafast radiative heat transfer**.
   R. Yu, A. Manjavacas, and F. J. García de Abajo.
   Nature Communications **8**, 2 (2017).
6. **Nonlinear Plasmonic Sensing with Nanographene**.
   R. Yu, J. D. Cox, and F. J. García de Abajo.
   Physical Review Letters **117**, 123904 (2016).
7. **Active modulation of visible light with graphene-loaded ultrathin metal plasmonic antennas**.
   R. Yu, V. Pruneri, and F. J. García de Abajo.
   Scientific Reports **6**, 32144 (2016).
8. **Electrical Detection of Single Graphene Plasmons**.
   R. Yu, and F. J. García de Abajo.
   ACS Nano **10**, 8045-8053 (2016).
9. **Structural Coloring of Glass Using Dewetted Nanoparticles and Ultrathin Films of Metals**.
   R. Yu, P. Mazumder, N. F. Borrelli, A. Carrilero, D. S. Ghosh, R. A. Maniyara, D.

Baker, F. J. García de Abajo, and V. Pruneri.
ACS Photonics **3**, 1194-1201 (2016). Selected for the cover.

10. **Resonant Visible Light Modulation with Graphene**.
R. Yu, V. Pruneri, and F. J. García de Abajo.
ACS Photonics **2**, 550-558 (2015).

Other articles related to this thesis

1. **Broadband Graphene Mid-Infrared Bolometer at Room Temperature**.
S. Yuan*, R. Yu*, C. Ma, B. Deng, Q. Guo, A. Levi, D. Naveh, F. J. García de Abajo, and F. Xia.
In preparation.
* Equal contribution

2. **Thermal Manipulation of Plasmons in Atomically Thin Films**.
E. J. C. Dias*, R. Yu*, and F. J. García de Abajo.
In preparation.
* Equal contribution

3. **Two-dimensional electron energy-loss spectroscopy**.
G. Mouloudakis*, R. Yu*, and F. J. García de Abajo.
In preparation.
* Equal contribution

4. **Tracking ultrafast hot-electron diffusion in space and time by ultrafast thermo-modulation microscopy**.
A. Block, M. Liebel, R. Yu, M. Spector, Y. Sivan, F. J. García de Abajo, and N. F. van Hulst.
Science Advances **5**, eaav8965 (2019).

5. **Tunable plasmons in ultrathin metal films**.
R. A. Maniyara, D. Rodrigo, R. Yu, J. Canet-Ferrer, D. S. Ghosh, R. Yongsunthon, D. Baker, A. Rezikyan, F. J. García de Abajo, and V. Pruneri.
Nature Photonics **13**, 328-333 (2019).

6. **Continuous-Wave Multiphoton Photoemission from Plasmonic Nanostars**.
M. Sivis, N. Pazos-Perez, R. Yu, R. A. Álvarez-Puebla, F. J. García de Abajo, and C. Ropers.
Communications Physics **1**, 13 (2018).

7. **Enhancement of Nonlinear Optical Phenomena by Localized Resonances**.
A. R. Echarri, J. D. Cox, R. Yu, F. J. García de Abajo.
ACS Photonics **5**, 1521-1527 (2018).

8. **Plasmonic Nano-Oven by Concatenation of Multishell Photothermal Enhancement**.
   L. Meng, R. Yu, M. Qiu, and F. J. García de Abajo.
   ACS Nano **11**, 7915-7924 (2017).

9. **Analytical description of the nonlinear plasmonic response in nanographene**.
   J. D. Cox, R. Yu, and F. J. García de Abajo.
   Physical Review B **96**, 045442 (2017).

10. **Hybrid plasmonic nanoresonators as efficient solar heat shields**.
    A. Sousa-Castillo, Ó. Ameneiro, M. Comesaña-Hermo, R. Yu, M. Pérez-Lorenzo, F. Rivadulla, F. J. García de Abajo, and M. A. Correa-Duarte.
    Nano Energy **37**, 118-125 (2017).

11. **Manipulating the interaction between localized and delocalized surface plasmon-polaritons in graphene**.
    R. Yu, R. Alaee, F. Lederer, and C. Rockstuhl.
    Physical Review B **90**, 085409 (2014).

Oral and invited contributions to international conferences

- *Ultrafast Radiative Heat Transfer*.
  R. Yu, A. Manjavacas, and F. Javier García de Abajo.
  NFO 15, Troyes, France. August 2018. Oral contribution.

- *Analytical Modeling of Graphene Plasmons*.
  R. Yu, J. D. Cox, J. R. M. Saavedra, and F. Javier García de Abajo.
  SPIE Optics+Photonics, San Diego, United States. August 2018. Oral contribution.

- *Ultrafast and Quantum Phenomena with Graphene Plasmons*.
  R. Yu, and F. Javier García de Abajo.
  METANANO 2017, Vladivostok, Russia. September 2017. **Invited contribution.**

- *Ultrafast Radiative Heat Transfer*.
  R. Yu, A. Manjavacas, and F. Javier García de Abajo.
  MEDINANO9, Amalfi, Italy. September 2017. **Invited contribution.**

- *Nonlinear Plasmonic Sensing with Nanographene*.
  R. Yu, J. D. Cox, and F. Javier García de Abajo.
  SPIE Optics+Photonics, San Diego, United States. August 2017. Oral contribution.

- *Ultrafast Radiative Heat Transfer*.
  R. Yu, A. Manjavacas, and F. J. García de Abajo.

SPIE Optics+Photonics, San Diego, United States. August 2017. Oral contribution.

- *Ultrafast Radiative Heat Transfer*.
  R. Yu, A. Manjavacas, and F. Javier García de Abajo.
  Photonics Global Student Conference, Singapore, Singapore. August 2017. **Country representative of Spain.**

- *Graphene Plasmons: Toward Single-Molecule and Single-Plasmon Detection*.
  R. Yu, and F. Javier García de Abajo.
  CLEO Europe, Munich, Germany. June 2017. Oral contribution.

- *Active Modulation of Visible Light with Graphene-Loaded Ultrathin Metal Plasmonic Antennas*.
  R. Yu, V. Pruneri, and F. Javier García de Abajo.
  CLEO Europe, Munich, Germany. June 2017. Oral contribution.

- *Nonlinear Plasmonic Sensing with Nanographene*.
  R. Yu, J. D. Cox, and F. Javier García de Abajo.
  CLEO Europe, Munich, Germany. June 2017. Oral contribution.

- *Quantum Physics with Graphene Plasmons*.
  R. Yu, and F. J. García de Abajo.
  SPP8, Taipei, Taiwan. May 2017. Oral contribution.

- *Graphene Plasmons: Toward Single-Molecule and Single-Plasmon Detection*.
  R. Yu, and F. J. García de Abajo.
  SPP8, Taipei, Taiwan. May 2017. Oral contribution.

- *Active Modulation of Visible Light with Graphene-Loaded Ultrathin Metal Plasmonic Antennas*.
  R. Yu, V. Pruneri, and F. J. García de Abajo.
  Metamaterials 2016, Crete, Greece. September 2016. Oral contribution.

- *Resonant Visible Light Modulation with Graphene*.
  R. Yu, V. Pruneri, and F. J. García de Abajo.
  Metamaterials 2016, Crete, Greece. September 2016. Oral contribution.

- *Active Modulation of Visible Light with Graphene-Loaded Ultrathin Metal Plasmonic Antennas*.
  R. Yu, V. Pruneri, and F. J. García de Abajo.
  SPIE Optics+Photonics, San Diego, United States. August 2016. Oral contribution.

- *Resonant Visible Light Modulation with Graphene*.
  R. Yu, V. Pruneri, and F. J. García de Abajo.

SPIE Optics+Photonics, San Diego, United States. August 2016. Oral contribution.

- *Graphene Plasmons: Toward Single-Molecule and Single-Plasmon Detection*.
  R. Yu, and F. J. García de Abajo.
  PIERS 2016, Shanghai, China. August 2016. Oral contribution.
- *Active Modulation of Visible Light with Graphene-Loaded Ultrathin Metal Plasmonic Antennas*.
  R. Yu, V. Pruneri, and F. J. García de Abajo.
  PIERS 2016, Shanghai, China. August 2016. Oral contribution.
- *Resonant Visible Light Modulation with Graphene*.
  R. Yu, V. Pruneri, and F. J. García de Abajo.
  PIERS 2016, Shanghai, China. August 2016. Oral contribution.
- *Graphene Plasmons: Toward Single-Molecule and Single-Plasmon Detection*.
  R. Yu, and F. Javier García de Abajo.
  META 16, Torremolinos, Spain. July 2016. **Invited contribution.**
- *Resonant Visible Light Modulation with Graphene*.
  R. Yu, V. Pruneri, and F. Javier García de Abajo.
  AOM 2015, Hangzhou, China. October 2015. Oral contribution.

Additionally, the research performed throughout this period has resulted in 16 poster contributions to conferences, defended by the author.

Bibliography

[1] I. Freestone, N. Meeks, M. Sax, and C. Higgitt, *The lycurgus cup - a roman nanotechnology*, Gold Bulletin **40**, 270–277 (2007). (see p. 8)

[2] Mark I. Stockman, *Nanofocusing of optical energy in tapered plasmonic waveguides*, Phys. Rev. Lett. **93**, 137404 (2004). (see p. 8)

[3] J. B. Pendry, *Negative refraction makes a perfect lens*, Phys. Rev. Lett. **85**, 3966–3969 (2000). (see p. 8)

[4] K. R. Li, M. I. Stockman, and D. J. Bergman, *Self-similar chain of metal nanospheres as an efficient nanolens*, Phys. Rev. Lett. **91**, 227402 (2003). (see p. 8)

[5] K. Kneipp, Y. Wang, H. Kneipp, L. T. Perelman, I. Itzkan, R. R. Dasari, and M. S. Feld, *Single molecule detection using surface-enhanced Raman scattering (SERS)*, Phys. Rev. Lett. **78**, 1667–1670 (1997). (see pp. 8, 33, and 107)

[6] S. Nie and S. R. Emory, *Probing single molecules and single nanoparticles by surface-enhanced raman scattering*, Science **275**, 1102–1106 (1997). (see pp. 8, 33, and 107)

[7] H. Xu, E. J. Bjerneld, M. Käll, and L. Börjesson, *Spectroscopy of single hemoglobin molecules by surface enhanced raman scattering*, Phys. Rev. Lett. **83**, 4357–4360 (1999). (see pp. 8, 33, and 107)

[8] M. Moskovits, *Surface-enhanced raman spectroscopy: a brief retrospective*, J. Raman Spectrosc. **36**, 485–496 (2005). (see pp. 8, 33, and 107)

[9] L. Rodríguez-Lorenzo, R. A. Álvarez-Puebla, I. Pastoriza-Santos, S. Mazzucco, O. Stéphan, M. Kociak, L. M. Liz-Marzán, and F. J. García de Abajo, *Zeptomol detection through controlled ultrasensitive surface-enhanced Raman scattering*, J. Am. Chem. Soc. **131**, 4616–4618 (2009). (see pp. 8 and 107)

[10] K. R. Catchpole and A. Polman, *Plasmonic solar cells*, Opt. Express **16**, 21793–21800 (2008). (see p. 8)

[11] H. A. Atwater and A. Polman, *Plasmonics for improved photovoltaic devices*, Nat. Mater. **9**, 205–213 (2010). (see p. 8)

[12] M. W. Knight, H. Sobhani, P. Nordlander, and N. J. Halas, *Photodetection with active optical antennas*, Science **332**, 702–704 (2011). (see p. 8)

[13] Yuan Liu, Rui Cheng, Lei Liao, Hailong Zhou, Jingwei Bai, Gang Liu, Lixin Liu, Yu Huang, and Xiangfeng Duan, *Plasmon resonance enhanced multicolour photodetection by graphene*, Nat. Commun. **2**, 579 (2011). (see p. 8)

[14] H. Chalabi, D. Schoen, and M. L. Brongersma, *Hot-electron photodetection with a plasmonic nanostripe antenna*, Nano Lett. **14**, 1374–1380 (2014). (see p. 8)

[15] Z. W. Seh, S. Liu, M. Low, S.-Y. Zhang, Z. Liu, A. Mlayah, and M.-Y. Han, *Janus au-tio$_2$ photocatalysts with strong localization of plasmonic near-fields for efficient visible-light hydrogen generation*, Adv. Mater. **24**(17), 2310–2314 (2012). (see pp. 8 and 33)

[16] J. Gu, Y.-W. Zhang, and F. Tao, *Shape control of bimetallic nanocatalysts through well-designed colloidal chemistry approaches*, Chem. Soc. Rev. **41**, 8050 (2012). (see pp. 8 and 33)

[17] S. Mukherjee, F. Libisch, N. Large, O. Neumann, L. V. Brown, J. Cheng, J. B. Lassiter, E. A. Carter, P. Nordlander, and N. J. Halas, *Hot electrons do the impossible: Plasmon-induced dissociation of h_2 on au*, Nano Lett. **13**, 240–247 (2013). (see pp. 8 and 33)

[18] S. Mubeen, J. Lee, N. Singh, S. Kramer, G. D. Stucky, and M. Moskovits, *An autonomous photosynthetic device in which all charge carriers derive from surface plasmons*, Nat. Nanotech. **8**, 247–251 (2013). (see pp. 8 and 33)

[19] C. Clavero, *Plasmon-induced hot-electron generation at nanoparticle/metal-oxide interfaces for photovoltaic and photocatalytic devices*, Nat. Photon. **8**, 95–103 (2014). (see pp. 8, 33, and 74)

[20] S. Mukherjee, L. Zhou, A. M. Goodman, N. Large, C. Ayala-Orozco, Y. Zhang, P. Nordlander, and N. J. Halas, *Hot-electron-induced dissociation of h_2 on gold nanoparticles supported on sio$_2$*, J. Am. Chem. Soc. **136**, 64–67 (2014). (see pp. 8 and 33)

[21] M. Danckwerts and L. Novotny, *Optical frequency mixing at coupled gold nanoparticles*, Phys. Rev. Lett. **98**, 026104 (2007). (see pp. 8, 33, and 107)

[22] S. Palomba and L. Novotny, *Nonlinear excitation of surface plasmon polaritons by four-wave mixing*, Phys. Rev. Lett. **101**(5), 056802 (2008). (see pp. 8 and 33)

[23] Joel D. Cox and F. J. García de Abajo, *Electrically tunable nonlinear plasmonics in graphene nanoislands*, Nat. Commun. **5**, 5725 (2014). (see pp. 8, 24, 107, 108, 112, and 144)

[24] Ximei Qian, Xiang-Hong Peng, Dominic O. Ansari, Qiqin Yin-Goen, Georgia Z. Chen, Dong M. Shin, Lily Yang, Andrew N. Young, May D. Wang, and Shuming Nie, *In vivo tumor targeting and spectroscopic detection with surface-enhanced raman nanoparticle tags*, Nat. Biotech. **26**, 83–90 (2008). (see pp. 8 and 33)

[25] LR Hirsch, RJ Stafford, JA Bankson, SR Sershen, B Rivera, RE Price, JD Hazle, NJ Halas, and JL West, *Nanoshell-mediated near-infrared thermal therapy of tumors under magnetic resonance guidance*, Proc. Natl. Academ. Sci. **100**, 13549–13554 (2003). (see pp. 8 and 33)

[26] J. D. Jackson, *Classical Electrodynamics*, Wiley, New York (1975). (see pp. 9 and 10)

[27] N. W. Ashcroft and N. D. Mermin, *Solid State Physics*, Harcourt College Publishers, New York (1976). (see p. 11)

[28] P. B. Johnson and R. W. Christy, *Optical constants of the noble metals*, Phys. Rev. B **6**, 4370–4379 (1972). (see pp. 11, 33, 38, 40, 45, 65, 67, and 79)

[29] R. Yu, L. M. Liz-Marzán, and F. J. García de Abajo, *Universal analytical modeling of plasmonic nanoparticles*, Chem. Soc. Rev. **46**, 6710–6724 (2017). (see pp. 12, 15, and 34)

[30] Gregory V Hartland, *Optical studies of dynamics in noble metal nanostructures*, Chem. Rev. **111**, 3858–3887 (2011). (see p. 16)

[31] K. S. Novoselov, A. K. Geim, S. V. Morozov, D. Jiang, Y. Zhang, S. V. Dubonos, I. V. Grigorieva, and A. A. Firsov, *Electric field effect in atomically thin carbon films*, Science **306**, 666–669 (2004). (see p. 16)

[32] A. K. Geim and K. S. Novoselov, *The rise of graphene*, Nat. Mater. **6**, 183–191 (2007). (see p. 16)

[33] A. H. Castro Neto, F. Guinea, N. M. R. Peres, K. S. Novoselov, and A. K. Geim, *The electronic properties of graphene*, Rev. Mod. Phys. **81**, 109–162 (2009). (see pp. 16, 22, 56, 58, 92, 107, 108, and 144)

[34] Hongtao Liu, Yunqi Liu, and Daoben Zhua, *Chemical doping of graphene*, J. Mater. Chem. **21**, 3335–3345 (2011). (see p. 16)

[35] B. Wunsch, T. Stauber, F. Sols, and F. Guinea, *Dynamical polarization of graphene at finite doping*, New J. Phys. **8**, 318 (2006). (see pp. 17, 22, 33, 60, and 62)

[36] E. H. Hwang and S. Das Sarma, *Dielectric function, screening, and plasmons in two-dimensional graphene*, Phys. Rev. B **75**, 205418 (2007). (see pp. 17, 33, 60, and 62)

[37] L. A. Falkovsky and A. A. Varlamov, *Space-time dispersion of graphene conductivity*, Eur. Phys. J. B **56**, 281 (2007). (see p. 17)

[38] F. J. García de Abajo, *Graphene plasmonics: Challenges and opportunities*, ACS Photon. **1**, 135–152 (2014). (see pp. 17, 34, 46, 48, 60, 66, 67, 74, 75, 77, 82, 84, 91, 92, 104, and 140)

[39] G. X. Ni, L. Wang, M. D. Goldflam, M. Wagner, Z. Fei, A. S. McLeod, M. K. Liu, F. Keilmann, B. Özyilmaz, A. H. Castro Neto, J. Hone, M. M. Fogler, and D. N. Basov, *Ultrafast optical switching of infrared plasmon polaritons in high-mobility graphene*, Nat. Photon. **10**, 244–248 (2016). (see pp. 17 and 74)

[40] R. Yu, A. Manjavacas, and F. J. García de Abajo, *Ultrafast radiative heat transfer*, Nat. Commun. **8**, 2 (2017). (see pp. 17, 28, 74, 82, and 84)

[41] L. Ju, B. Geng, J. Horng, C. Girit, M. Martin, Z. Hao, H. A. Bechtel, X. Liang, A. Zettl, Y. R. Shen, and F. Wang, *Graphene plasmonics for tunable terahertz metamaterials*, Nat. Nanotech. **6**, 630–634 (2011). (see pp. 18, 33, 74, 91, and 107)

[42] H. Yan, X. Li, B. Chandra, G. Tulevski, Y. Wu, M. Freitag, W. Zhu, P. Avouris, and F. Xia, *Tunable infrared plasmonic devices using graphene/insulator stacks*, Nat. Nanotech. **7**, 330–334 (2012). (see pp. 18, 33, 74, and 91)

[43] Hugen Yan, Tony Low, Wenjuan Zhu, Yanqing Wu, Marcus Freitag, Xuesong Li, Francisco Guinea, Phaedon Avouris, and Fengnian Xia, *Damping pathways of mid-infrared plasmons in graphene nanostructures*, Nat. Photon. **7**, 394–399 (2013). (see pp. 18, 33, and 91)

[44] Z. Fei, A. S. Rodin, G. O. Andreev, W. Bao, A. S. McLeod, M. Wagner, L. M. Zhang, Z. Zhao, M. Thiemens, G. Dominguez, M. M. Fogler, A. H. Castro Neto, C. N. Lau, F. Keilmann, and D. N. Basov, *Gate-tuning of graphene plasmons revealed by infrared nano-imaging*, Nature **487**, 82–85 (2012). (see pp. 18, 33, and 91)

[45] J. Chen, M. Badioli, P. Alonso-González, S. Thongrattanasiri, F. Huth, J. Osmond, M. Spasenović, A. Centeno, A. Pesquera, P. Godignon, A. Zurutuza Elorza, N. Camara, F. J. García de Abajo, R. Hillenbrand, and F. H. L. Koppens, *Optical nano-imaging of gate-tunable graphene plasmons*, Nature **487**, 77–81 (2012). (see pp. 18, 33, 91, and 107)

[46] Achim Woessner, Mark B. Lundeberg, Yuanda Gao, Alessandro Principi, Pablo Alonso-González, Matteo Carrega, Kenji Watanabe, Takashi Taniguchi, Gio-

vanni Vignale, Marco Polini, James Hone, Rainer Hillenbrand, and Frank H.L. Koppens, *Highly confined low-loss plasmons in graphene-boron nitride heterostructures*, Nat. Mater. **14**, 421–425 (2015). (see pp. 18, 33, and 91)

[47] G.X. Ni, A.S. McLeod, Z. Sun, L. Wang, L. Xiong, K.W. Post, S.S. Sunku, B.-Y. Jiang, J. Hone, C.R. Dean, M.M. Fogler, and D.N. Basov, *Fundamental limits to graphene plasmonics*, Nature **557**, 530 (2018). (see p. 18)

[48] J. D. Jackson, *Classical Electrodynamics*, Wiley, New York (1999). (see pp. 19, 38, and 61)

[49] D. Pines and P. Nozières, *The Theory of Quantum Liquids*, W. A. Benjamin, Inc., New York (1966). (see pp. 20, 21, 91, and 108)

[50] L. Hedin and S. Lundqvist, Effects of electron-electron and electron-phonon interactions on the one-electron states of solids, In David Turnbull Frederick Seitz and Henry Ehrenreich, editors, *Solid State Physics* volume 23 of *Solid State Physics* pages 1 – 181. Academic Press (1970). (see pp. 20, 21, and 108)

[51] D. Pines, *Elementary Excitations in Solids*, W. A. Benjamin, Inc., New York (1963). (see pp. 20 and 21)

[52] A. Messiah, *Quantum Mechanics*, North-Holland, New York (1966). (see p. 22)

[53] P. R. Wallace, *The band theory of graphite*, Phys. Rev. **71**, 622–634 (1947). (see pp. 22, 56, 58, 107, 108, and 144)

[54] Y. Tao, J.M. Boss, B.A. Moores, and C.L. Degen, *Single-crystal diamond nanomechanical resonators with quality factors exceeding one million*, Nature Communications **5**, 3638 (2014). (see p. 26)

[55] A. M. Gobin, M. H. Lee, N. J. Halas, W. D. James, R. A. Drezek, and J. L. West, *Near-infrared resonant nanoshells for combined optical imaging and photothermal cancer therapy*, Nano Lett. **7**, 1929–1934 (2007). (see pp. 26 and 74)

[56] H. M. Pollock and A. Hammiche, *Micro-thermal analysis: techniques and applications*, J. Phys. D: Appl. Phys. **34**, R23–R53 (2001). (see pp. 26 and 74)

[57] L. Wang and B. Li, *Thermal memory: A storage of phononic information*, Phys. Rev. Lett. **101**, 267203 (2008). (see pp. 26 and 74)

[58] A. G. Skirtach, C. Dejugnat, D. Braun, A. S. Susha, A. L. Rogach, W. J. Parak, H. Möhwald, and G. B. Sukhorukov, *The role of metal nanoparticles in remote release of encapsulated materials*, Nano Lett. **5**, 1371–1377 (2005). (see p. 26)

[59] G. Baffou, R. Quidant, and F. J. García de Abajo, *Nanoscale control of optical heating in complex plasmonic systems*, ACS Nano **4**, 709–716 (2010). (see pp. 26 and 74)

[60] S. Mukherjee, F. Libisch, N. Large, O. Neumann, L. V. Brown, J. Cheng, J. B. Lassiter, E. A. Carter, P. Nordlander, and N. J. Halas, *Hot electrons do the impossible: Plasmon-induced dissociation of h_2 on au*, Nano Lett. **13**(1), 240–247 (2013). (see p. 27)

[61] Matt W. Graham, Su-Fei Shi, Zenghui Wang, Daniel C. Ralph, Jiwoong Park, and Paul L. McEuen, *Transient absorption and photocurrent microscopy show that hot electron supercollisions describe the rate-limiting relaxation step in graphene*, Nano Lett. **13**, 5497–5502 (2013). (see p. 27)

[62] Jeong Young Park, Sun Mi Kim, Hyosun Lee, and Ievgen I Nedrygailov, *Hot-electron-mediated surface chemistry: toward electronic control of catalytic activity*, Acc. Chem. Res. **48**, 2475–2483 (2015). (see p. 27)

[63] J. R. M. Saavedra, A. Asenjo-Garcia, and F. J. García de Abajo, *Hot-electron dynamics and thermalization in small metallic nanoparticles*, ACS Photon. **3**, 1637–1646 (2016). (see p. 27)

[64] P Grua, JP Morreeuw, H Bercegol, G Jonusauskas, and F Vallée, *Electron kinetics and emission for metal nanoparticles exposed to intense laser pulses*, Phys. Rev. B **68**, 035424 (2003). (see pp. 27 and 82)

[65] C. M. Hargreaves, *Anomalous radiative transfer between closely-spaced bodies*, Phys. Lett. **30A**, 491–492 (1969). (see pp. 28 and 74)

[66] G. A. Domoto, R. F. Boehm, and C. L. Tien, *Experimental investigation of radiative transfer between metallic surfaces at cryogenic temperatures*, J. Heat Transfer **92**, 412–416 (1970). (see pp. 28 and 74)

[67] D. Polder and M. Van Hove, *Theory of radiative heat transfer between closely spaced bodies*, Phys. Rev. B **4**, 3303–3314 (1971). (see pp. 28 and 74)

[68] A. Manjavacas and F. J. García de Abajo, *Radiative heat transfer between neighboring particles*, Phys. Rev. B **86**, 075466 (2012). (see p. 29)

[69] H. Nyquist, *Thermal agitation of electric charge in conductors*, Phys. Rev. **32**, 110–113 (1928). (see pp. 30 and 129)

[70] H. B. Callen and T. A. Welton, *Irreversibility and generalized noise*, Phys. Rev. **83**, 34–40 (1951). (see pp. 30 and 129)

[71] S. M. Rytov, *Theory of Electric Fluctuations and Thermal Radiation*, Air Force Cambridge Research Center, Bedford, MA (1959). (see pp. 30 and 76)

[72] A. Manjavacas and F. J. García de Abajo, *Vacuum friction in rotating particles*, Phys. Rev. Lett. **105**, 113601 (2010). (see pp. 30 and 76)

[73] M. Jablan, H. Buljan, and M. Soljačić, *Plasmonics in graphene at infrared frequencies*, Phys. Rev. B **80**, 245435 (2009). (see pp. 33 and 107)

[74] Z. Fei, G. O. Andreev, W. Bao, L. M. Zhang, A. S. McLeod, C. Wang, M. K. Stewart, Z. Zhao, G. Dominguez, M. Thiemens, M. M. Fogler, M. J. Tauber, A. H. Castro-Neto, C. N. Lau, F. Keilmann, and D. N. Basov, *Infrared nanoscopy of dirac plasmons at the graphene–sio$_2$ interface*, Nano Lett. **11**, 4701–4705 (2011). (see pp. 33 and 91)

[75] S. Y. Shin, N. D. Kim, J. G. Kim, K. S. Kim, D. Y. Noh, Kwang S. Kim, and J. W. Chung, *Control of the π plasmon in a single layer graphene by charge doping*, Appl. Phys. Lett. **99**, 082110 (2011). (see pp. 33 and 91)

[76] H. Yan, Z. Li, X. Li, W. Zhu, P. Avouris, and F. Xia, *Infrared spectroscopy of tunable dirac terahertz magneto-plasmons in graphene*, Nano Lett. **12**, 3766–3771 (2012). (see pp. 33 and 91)

[77] Zheyu Fang, Sukosin Thongrattanasiri, Andrea Schlather, Zheng Liu, Lulu Ma, Yumin Wang, Pulickel M. Ajayan, Peter Nordlander, Naomi J. Halas, and F. J. García de Abajo, *Gated tunability and hybridization of localized plasmons in nanostructured graphene*, ACS Nano **7**, 2388–2395 (2013). (see pp. 33, 67, and 91)

[78] V. W. Brar, M. S. Jang, M. Sherrott, J. J. Lopez, and H. A. Atwater, *Highly confined tunable mid-infrared plasmonics in graphene nanoresonators*, Nano Lett. **13**, 2541–2547 (2013). (see pp. 33, 74, 85, and 91)

[79] Renwen Yu, Rasoul Alaee, Falk Lederer, and Carsten Rockstuhl, *Manipulating the interaction between localized and delocalized surface plasmon-polaritons in graphene*, Phys. Rev. B **90**, 085409 (2014). (see pp. 33 and 107)

[80] R. Yu, P. Mazumder, N. F. Borrelli, A. Carrilero, D. S. Ghosh, R. A. Maniyara, D. Baker, F. J. García de Abajo, and V. Pruneri, *Structural coloring of glass using dewetted nanoparticles and ultrathin films of metals*, ACS Photon. **3**, 1194–1201 (2016). (see pp. 33 and 46)

[81] R. Yu, V. Pruneri, and F. J. García de Abajo, *Active modulation of visible light with graphene-loaded ultrathin metal plasmonic antennas*, Sci. Rep. **6**, 32144 (2016). (see p. 33)

[82] J. D. Cox, R. Yu, and F. J. García de Abajo, *Analytical description of the nonlinear plasmonic response in nanographene*, Phys. Rev. B **96**, 045442 (2017). (see p. 33)

[83] A Rodríguez Echarri, Joel D Cox, Renwen Yu, and F Javier García de Abajo, *Enhancement of nonlinear optical phenomena by localized resonances*, ACS Photonics **5**, 1521–1527 (2018). (see p. 33)

[84] Murat Sivis, Nicolas Pazos-Perez, Renwen Yu, Ramon Alvarez-Puebla, F Javier García de Abajo, and Claus Ropers, *Continuous-wave multiphoton photoemission from plasmonic nanostars*, Communications Physics **1**, 13 (2018). (see p. 33)

[85] U. Kreibig and M. Vollmer, *Optical Properties of Metal Clusters*, Springer-Verlag, Berlin (1995). (see p. 34)

[86] F. J. García de Abajo, *Nonlocal effects in the plasmons of strongly interacting nanoparticles, dimers, and waveguides*, J. Phys. Chem. C **112**, 17983–17987 (2008). (see p. 34)

[87] Wenqi Zhu, Ruben Esteban, Andrei G. Borisov, Jeremy J. Baumberg, Peter Nordlander, Henri J. Lezec, Javier Aizpurua, and Kenneth B. Crozier, *Quantum mechanical effects in plasmonic structures with subnanometre gaps*, Nat. Commun. **7**, 11495 (2016). (see p. 34)

[88] R. Fuchs, *Theory of the optical properties of small cubes*, Phys. Lett. A **48**, 353–354 (1974). (see p. 34)

[89] D. J. Bergman, *Dielectric constant of a two-component granular composite: A practical scheme for calculating the pole spectrum*, Phys. Rev. B **19**, 2359–2368 (1979). (see p. 34)

[90] F. Ouyang and M. Isaacson, *Surface plasmon excitation of objects with arbitrary shape and dielectric constant*, Philos. Mag. B **60**, 481–492 (1989). (see p. 34)

[91] F. Ouyang and M. Isaacson, *Accurate modeling of particle-substrate coupling of surface plasmon excitation in eels*, Ultramicroscopy **31**, 345–349 (1989). (see p. 34)

[92] T. J. Davis and D. E. Gómez, *Colloquium: An algebraic model of localized surface plasmons and their interactions*, Rev. Mod. Phys. **89**, 011003 (2017). (see p. 34)

[93] R. Gans, *The shape of ultra microscopic gold particles*, Ann. Phys. (Leipzig) **37**, 881–900 (1912). (see p. 35)

[94] F. J. García de Abajo and A. Howie, *Retarded field calculation of electron energy loss in inhomogeneous dielectrics*, Phys. Rev. B **65**, 115418 (2002). (see pp. 37, 39, 40, and 139)

[95] S. E. Lohse and C. J. Murphy, *The quest for shape control: A history of gold nanorod synthesis*, Chem. Mater. **25**, 1250–1261 (2013). (see p. 40)

[96] H. C. van de Hulst, *Light Scattering by Small Particles*, Dover, New York (1981). (see p. 44)

[97] Igor Zorić, Michael Zäch, Bengt Kasemo, and Christoph Langhammer, *Gold, platinum, and aluminum nanodisk plasmons: material independence, subradiance, and damping mechanisms*, ACS Nano **5**, 2535–2546 (2011). (see pp. 44 and 45)

[98] E. D. Palik, *Handbook of Optical Constants of Solids*, Academic Press, San Diego (1985). (see p. 45)

[99] F. J. García de Abajo, *Multiple excitation of confined graphene plasmons by single free electrons*, ACS Nano **7**, 11409–11419 (2013). (see pp. 46, 77, and 137)

[100] I. Silveiro, J. M. Plaza Ortega, and F. J. García de Abajo, *Plasmon wave function of graphene nanoribbons*, New J. Phys. **17**, 083013 (2015). (see pp. 47, 77, and 137)

[101] Shuang Zhang, Dentcho A Genov, Yuan Wang, Ming Liu, and Xiang Zhang, *Plasmon-induced transparency in metamaterials*, Phys. Rev. Lett. **101**, 047401 (2008). (see p. 52)

[102] Lei Wang, Wei Cai, Weiwei Luo, Zenghong Ma, Chenglin Du, Xinzheng Zhang, and Jingjun Xu, *Mid-infrared plasmon induced transparency in heterogeneous graphene ribbon pairs*, Opt. Express **22**, 32450–32456 (2014). (see p. 52)

[103] R. R. Nair, P. Blake, A. N. Grigorenko, K. S. Novoselov, T. J. Booth, T. Stauber, N. M. R. Peres, and A. K. Geim, *Fine structure constant defines visual transparency of graphene*, Science **320**, 1308 (2008). (see pp. 56, 58, and 87)

[104] K. F. Mak, M. Y. Sfeir, Y. Wu, C. H. Lui, J. A. Misewich, and T. F. Heinz, *Measurement of the optical conductivity of graphene*, Phys. Rev. Lett. **101**, 196405 (2008). (see pp. 56, 58, and 87)

[105] Z. Q. Li, E. A. Henriksen, Z. Jian, Z. Hao, M. C. Martin, P. Kim, H. L. Stormer, and D. N. Basov, *Dirac charge dynamics in graphene by infrared spectroscopy*, Nat. Phys. **4**, 532–535 (2008). (see pp. 56 and 87)

[106] C. F. Chen, C. H. Park, B. W. Boudouris, J. Horng, B. Geng, C. Girit, A. Zettl, M. F. Crommie, R. A. Segalman, S. G. Louie, and F. Wang, *Controlling inelastic light scattering quantum pathways in graphene*, Nature **471**, 617–620 (2011). (see pp. 56, 87, and 91)

[107] Ming Liu, Xiaobo Yin, Erick Ulin-Avila, Baisong Geng, Thomas Zentgraf, Long Ju, Feng Wang, and Xiang Zhang, *A graphene-based broadband optical modulator*, Nature **474**, 64–67 (2011). (see p. 56)

[108] Xuetao Gan, Kin Fai Mak, Yuanda Gao, Yumeng You, Fariba Hatami, James Hone, Tony F. Heinz, and Dirk Englund, *Strong enhancement of light–matter interaction in graphene coupled to a photonic crystal nanocavity*, Nano Lett. **12**, 5626–5631 (2012). (see p. 56)

[109] Arka Majumdar, Jonghwan Kim, Jelena Vuckovic, and Feng Wang, *Electrical control of silicon photonic crystal cavity by graphene*, Nano Lett. **13**, 515–518 (2013). (see p. 56)

[110] L. L. Chang, L. Esaki, and R. Tsu, *Resonant tunneling in semiconductor double barriers*, Appl. Phys. Lett. **24**, 593–595 (1974). (see p. 58)

[111] R. Sainidou, J. Renger, T. V. Teperik, M. U. González, R. Quidant, and F. J. García de Abajo, *Extraordinary all-dielectric light enhancement over large volumes*, Nano Lett. **10**, 4450–4455 (2010). (see p. 58)

[112] C. R. Dean, A. F. Young, I. Meric, C. Lee, L. Wang, S. Sorgenfrei, K. Watanabe, T. Taniguchi, P. Kim, K. L. Shepard, and J. Hone, *Boron nitride substrates for high-quality graphene electronics*, Nat. Nanotech. **5**, 722–726 (2010). (see p. 59)

[113] N. Stefanou, V. Yannopapas, and A. Modinos, *Multem 2: A new version of the program for transmission and band-structure calculations of photonic crystals*, Comput. Phys. Commun. **132**, 189–196 (2000). (see pp. 61 and 62)

[114] Shanhui Fan, *Sharp asymmetric line shapes in side-coupled waveguide-cavity systems*, Appl. Phys. Lett. **80**, 908–910 (2002). (see p. 62)

[115] Lord Rayleigh, *Note on the remarkable case of diffraction spectra described by Prof. Wood*, Philos. Mag. **14**, 60–65 (1907). (see p. 64)

[116] F. J. García de Abajo, *Colloquium: Light scattering by particle and hole arrays*, Rev. Mod. Phys. **79**, 1267–1290 (2007). (see p. 64)

[117] R. Yu, V. Pruneri, and F. J. García de Abajo, *Resonant visible light modulation with graphene*, ACS Photon. **2**, 550–558 (2015). (see p. 64)

[118] S. Thongrattanasiri, F. H. L. Koppens, and F. J. García de Abajo, *Complete optical absorption in periodically patterned graphene*, Phys. Rev. Lett. **108**, 047401 (2012). (see pp. 69 and 74)

[119] Takuya Inoue, Menaka De Zoysa, Takashi Asano, and Susumu Noda, *Realization of dynamic thermal emission control*, Nat. Mater. **13**, 928–931 (2014). (see p. 71)

[120] Shu-Chen Wen, Chih-Wei Chang, Chia-Ming Lin, Hua an Liu, Vincent K.S. Hsiao, Jianhui Yu, and Zhe Chen, *Light-induced switching of a chalcogenide-coated side-polished fiber device*, Opt. Commun. **334**, 110–114 (2015). (see p. 71)

[121] L. Meng, R. Yu, M. Qiu, and F. J. García de Abajo, *Plasmonic nano-oven by concatenation of multishell photothermal enhancement*, ACS Nano **11**, 7915–7924 (2017). (see p. 74)

[122] Ana Sousa-Castillo, Óscar Ameneiro-Prieto, Miguel Comesaña-Hermo, Renwen Yu, José M Vila-Fungueiriño, Moisés Pérez-Lorenzo, Francisco Rivadulla, F Javier García de Abajo, and Miguel A Correa-Duarte, *Hybrid plasmonic nanoresonators as efficient solar heat shields*, Nano Energy **37**, 118–125 (2017). (see p. 74)

[123] Renwen Yu, Qiushi Guo, Fengnian Xia, and F Javier García de Abajo, *Photothermal engineering of graphene plasmons*, Physical Review Letters **121**, 057404 (2018). (see p. 74)

[124] P. K. Jain, I. H. El-Sayed, and M. A. El-Sayed, *Au nanoparticles target cancer*, Nano Today **2**, 18–29 (2007). (see p. 74)

[125] W. Zhao and J. M. Karp, *Tumour targeting: Nanoantennas heat up*, Nat. Mater. **8**, 453–454 (2009). (see p. 74)

[126] M. A. Barral and A. M. Llois, *Photothermal imaging of nanometer-sized metal particles among scatterers*, Science **297**, 1160–1163 (2002). (see p. 74)

[127] S. Berciaud, D. Lasne, G. A. Blab, L. Cognet, and B. Lounis, *Photothermal heterodyne imaging of individual metallic nanoparticles: Theory versus experiment*, Phys. Rev. B **73**, 045424 (2006). (see p. 74)

[128] Qiushi Guo, Renwen Yu, Cheng Li, Shaofan Yuan, Bingchen Deng, F Javier García de Abajo, and Fengnian Xia, *Efficient electrical detection of mid-infrared graphene plasmons at room temperature*, Nature Materials **17**, 986–992 (2018). (see p. 74)

[129] Rasoul Alaee, Mohamed Farhat, Carsten Rockstuhl, and Falk Lederer, *A perfect absorber made of a graphene micro-ribbon metamaterial*, Opt. Express **20**, 28017–28024 (2012). (see p. 74)

[130] Min Seok Jang, Victor W. Brar, Michelle C. Sherrott, Josue J. Lopez, Laura Kim, Seyoon Kim, Mansoo Choi, and Harry A. Atwater, *Tunable large resonant absorption in a midinfrared graphene salisbury screen*, Phys. Rev. B **90**, 165409 (2014). (see pp. 74 and 85)

[131] Marcus Freitag, Tony Low, Wenjuan Zhu, Hugen Yan, Fengnian Xia, and Phaedon Avouris, *Photocurrent in graphene harnessed by tunable intrinsic plasmons*, Nat. Commun. **4**, 1951 (2013). (see p. 74)

[132] R. Yu and F. J. García de Abajo, *Electrical detection of single graphene plasmons*, ACS Nano **10**, 8045–8053 (2016). (see pp. 74 and 92)

[133] Mark B. Lundeberg, Yuanda Gao, Achim Woessner, Cheng Tan, Pablo Alonso-González, Kenji Watanabe, Takashi Taniguchi, James Hone, Rainer Hillenbrand, and Frank H. L. Koppens, *Thermoelectric detection and imaging of propagating graphene plasmons*, Nat. Mater. **16**, 204–207 (2016). (see p. 74)

[134] D. Rodrigo, O. Limaj, D. Janner, D. Etezadi, F. J. García de Abajo, V. Pruneri, and H. Altug, *Mid-infrared plasmonic biosensing with graphene*, Science **349**, 165–168 (2015). (see pp. 74, 87, and 107)

[135] R. Yu, J. D. Cox, and F. J. García de Abajo, *Nonlinear plasmonic sensing with nanographene*, Phys. Rev. Lett. **117**, 123904 (2016). (see p. 74)

[136] Hai Hu, Xiaoxia Yang, Feng Zhai, Debo Hu, Ruina Liu, Kaihui Liu, Zhipei Sun, and Qing Dai, *Far-field nanoscale infrared spectroscopy of vibrational fingerprints of molecules with graphene plasmons*, Nat. Commun. **7**, 12334 (2016). (see p. 74)

[137] Rama Venkatasubramanian, Edward Siivola, Thomas Colpitts, and Brooks O'quinn, *Thin-film thermoelectric devices with high room-temperature figures of merit*, Nature **413**, 597–602 (2001). (see p. 74)

[138] Bozhi Tian, Xiaolin Zheng, Thomas J Kempa, Ying Fang, Nanfang Yu, Guihua Yu, Jinlin Huang, and Charles M Lieber, *Coaxial silicon nanowires as solar cells and nanoelectronic power sources*, Nature **449**, 885–889 (2007). (see p. 74)

[139] Raphael St-Gelais, Biswajeet Guha, Linxiao Zhu, Shanhui Fan, and Michal Lipson, *Demonstration of strong near-field radiative heat transfer between integrated nanostructures*, Nano Lett. **14**, 6971–6975 (2014). (see p. 74)

[140] Peng Wang, Shaik M Zakeeruddin, Jacques E Moser, Mohammad K Nazeeruddin, Takashi Sekiguchi, and Michael Grätzel, *A stable quasi-solid-state dye-sensitized solar cell with an amphiphilic ruthenium sensitizer and polymer gel electrolyte*, Nat. Mater. **2**, 402–407 (2003). (see p. 74)

[141] David R. Lide, *Handbook of Chemistry and Physics*, CRC Press, Boca Raton, FL (2005). (see p. 74)

[142] Biswajeet Guha, Clayton Ryan Otey, Carl B. Poitras, Shanhui Fan, , and Michal Lipson, *Near-field radiative cooling of nanostructures*, Nano Lett. **12**, 4546–4550 (2012). (see p. 74)

[143] F. Reif, *Fundamentals of Statistical and Thermal Physics*, McGraw-Hill, New York (1965). (see p. 74)

[144] V. P. Gusynin, S. G. Sharapov, and J. P. Carbotte, *Unusual microwave response of dirac quasiparticles in graphene*, Phys. Rev. Lett. **96**, 256802 (2006). (see p. 77)

[145] V. P. Gusynin, S. G. Sharapov, and J. P. Carbotte, *On the universal ac optical background in graphene*, New J. Phys. **11**, 095013 (2009). (see pp. 77 and 82)

[146] Isabella Gierz, Jesse C Petersen, Matteo Mitrano, Cephise Cacho, I C Edmond Turcu, Emma Springate, Alexander Stöhr, Axel Köhler, Ulrich Starke, and Andrea Cavalleri, *Snapshots of non-equilibrium dirac carrier distributions in graphene*, Nat. Mater **12**, 1119–1124 (2013). (see pp. 77 and 87)

[147] Zhibin Lin, Leonid V. Zhigilei, and Vittorio Celli, *Electron-phonon coupling and electron heat capacity of metals under conditions of strong electron-phonon nonequilibrium*, Phys. Rev. B **77**, 075133 (2008). (see p. 78)

[148] A. I. Volokitin and B. N. J. Persson, *Near-field radiative heat transfer and noncontact friction*, Rev. Mod. Phys. **79**, 1291–1329 (2007). (see p. 79)

[149] Jahan M Dawlaty, Shriram Shivaraman, Mvs Chandrashekhar, Farhan Rana, and Michael G Spencer, *Measurement of ultrafast carrier dynamics in epitaxial graphene*, Appl. Phys. Lett. **92**, 042116 (2008). (see pp. 80, 93, and 96)

[150] S. Winnerl, M. Orlita, P. Plochocka, P. Kossacki, M. Potemski, T. Winzer, E. Malic, A. Knorr, M. Sprinkle, C. Berger, W. A. de Heer, H. Schneider, and M. Helm, *Carrier relaxation in epitaxial graphene photoexcited near the dirac point*, Phys. Rev. Lett. **107**, 237401 (2011). (see pp. 80, 93, and 96)

[151] N. M. Gabor, J. C. W. Song, Q. Ma, N. L. Nair, T. Taychatanapat, K. Watanabe, T. Taniguchi, L. S. Levitov, and P. Jarrillo-Herrero, *Hot carrier-assisted intrinsic photoresponse in graphene*, Science **334**, 648–652 (2011). (see pp. 81 and 91)

[152] K. J. Tielrooij, S. A. Jensen J. C. W. Song and, A. Centeno, A. Pesquera, A. Zurutuza Elorza, M. Bonn, L. S. Levitov, and F. H. L. Koppens, *Photoexcitation cascade and multiple hot-carrier generation in graphene*, Nat. Phys. **9**, 248–252 (2013). (see pp. 81 and 91)

[153] Z. Mics, K. J. Tielrooij, K. Parvez, S. A. Jensen, I. Ivanov, X. Feng, K. Müllen, M. Bonn, and D. Turchinovich, *Thermodynamic picture of ultrafast charge transport in graphene*, Nat. Commun. **6**, 7655 (2015). (see pp. 81 and 91)

[154] T. J. Echtermeyer, L. Britnell, P. K. Jasnos, A. Lombardo, R. V. Gorbachev, A. N. Grigorenko, A. K. Geim, A. C. Ferrari, and K. S. Novoselov, *Strong plasmonic enhancement of photovoltage in graphene*, Nat. Commun. **2**, 458 (2011). (see pp. 81 and 91)

[155] R. Yu, J. D. Cox, J. R. M. Saavedra, and F. J. García de Abajo, *Analytical modeling of graphene plasmons*, ACS Photon. **4**, 3106–3114 (2017). (see p. 82)

[156] JK Viljas and TT Heikkilä, *Electron-phonon heat transfer in monolayer and bilayer graphene*, Phys. Rev. B **81**, 245404 (2010). (see p. 82)

[157] Justin CW Song, Michael Y Reizer, and Leonid S Levitov, *Disorder-assisted electron-phonon scattering and cooling pathways in graphene*, Phys. Rev. Lett. **109**, 106602 (2012). (see pp. 82 and 101)

[158] AC Betz, Sung Ho Jhang, Emiliano Pallecchi, Robson Ferreira, Gwendal Fève, Jean-Marc Berroir, and Bernard Plaçais, *Supercollision cooling in undoped graphene*, Nat. Phys. **9**, 109–112 (2013). (see p. 82)

[159] Matt W Graham, Su-Fei Shi, Daniel C Ralph, Jiwoong Park, and Paul L McEuen, *Photocurrent measurements of supercollision cooling in graphene*, Nat. Phys. **9**, 103–108 (2013). (see p. 82)

[160] Christopher B McKitterick, Daniel E Prober, and Michael J Rooks, *Electron-phonon cooling in large monolayer graphene devices*, Phys. Rev. B **93**, 075410 (2016). (see pp. 82 and 83)

[161] Tony Low, Vasili Perebeinos, Raseong Kim, Marcus Freitag, and Phaedon Avouris, *Cooling of photoexcited carriers in graphene by internal and substrate phonons*, Phys. Rev. B **86**, 045413 (2012). (see p. 83)

[162] Marcus Freitag, Tony Low, and Phaedon Avouris, *Increased responsivity of suspended graphene photodetectors*, Nano Lett. **13**, 1644–1648 (2013). (see p. 83)

[163] Klaas-Jan Tielrooij, Niels CH Hesp, Alessandro Principi, Mark B Lundeberg, Eva AA Pogna, Luca Banszerus, Zoltán Mics, Mathieu Massicotte, Peter Schmidt, Diana Davydovskaya, et al., *Out-of-plane heat transfer in van der waals stacks through electron–hyperbolic phonon coupling*, Nat. Nanotech. **13**, 1 (2017). (see p. 83)

[164] S Yiğen, V Tayari, JO Island, JM Porter, and AR Champagne, *Electronic thermal conductivity measurements in intrinsic graphene*, Phys. Rev. B **87**, 241411 (2013). (see p. 83)

[165] Jesse Crossno, Jing K Shi, Ke Wang, Xiaomeng Liu, Achim Harzheim, Andrew Lucas, Subir Sachdev, Philip Kim, Takashi Taniguchi, Kenji Watanabe, et al., *Observation of the dirac fluid and the breakdown of the wiedemann-franz law in graphene*, Science **351**, 1058–1061 (2016). (see p. 83)

[166] Tae Yun Kim, Cheol-Hwan Park, and Nicola Marzari, *The electronic thermal conductivity of graphene*, Nano Lett. **16**, 2439–2443 (2016). (see p. 83)

[167] M Ben Rhouma, M Oueslati, and Brahim Guizal, *Surface plasmons on a doped graphene sheet with periodically modulated conductivity*, Superlattices and Microstructures **96**, 212–219 (2016). (see p. 85)

[168] Weilu Gao, Gang Shi, Zehua Jin, Jie Shu, Qi Zhang, Robert Vajtai, Pulickel M Ajayan, Junichiro Kono, and Qianfan Xu, *Excitation and active control of prop-*

agating surface plasmon polaritons in graphene, Nano Letters **13**, 3698–3702 (2013). (see p. 85)

[169] Huan Hu, Shouvik Banerjee, David Estrada, Rashid Bashir, and William P. King, *Tip-based nanofabrication of arbitrary shapes of graphene nanoribbons for device applications*, RSC Adv. **5**, 37006–37012 (2015). (see p. 87)

[170] Jinming Cai, Pascal Ruffieux, Rached Jaafar, Marco Bieri, Thomas Braun, Stephan Blankenburg, Matthias Muoth, Ari P. Seitsonen, Moussa Saleh, Xinliang Feng, Klaus Müllen, and Roman Fasel, *Atomically precise bottom-up fabrication of graphene nanoribbons*, Nature **466**, 470–473 (2010). (see p. 87)

[171] J. Hicks, A. Tejeda, A. Taleb-Ibrahimi, M. S. Nevius, F. Wang, K. Shepperd, J. Palmer, F. Bertran, P. Le Fàvre, J. Kunc, W. A. de Heer, C. Berger, and E. H. Conrad, *A wide-bandgap metal-semiconductor-metal nanostructure made entirely from graphene*, Nat. Phys. **9**, 49–54 (2013). (see p. 87)

[172] Ruquan Ye, Changsheng Xiang, Jian Lin, Zhiwei Peng, Kewei Huang, Zheng Yan, Nathan P. Cook, Errol L.G. Samuel, Chih-Chau Hwang, Gedeng Ruan, Gabriel Ceriotti, Abdul-Rahman O. Raji, Angel A. Martí, and James M. Tour, *Coal as an abundant source of graphene quantum dots*, Nat. Commun. **4**, 2943 (2013). (see p. 87)

[173] D. Brida, A. Tomadin, C. Manzoni, Y. J. Kim, A. Lombardo, S. Milana, R. R. Nair, K. S. Novoselov, A. C. Ferrari, G. Cerullo, and M. Polini, *Ultrafast collinear scattering and carrier multiplication in graphene*, Nat. Commun. **4**, 1987 (2013). (see p. 87)

[174] D. N. Basov, M. M. Fogler, and F. J. García de Abajo, *Polaritons in van der waals materials*, Science **354**, aag1992 (2016). (see p. 88)

[175] S. Thongrattanasiri and F. J. García de Abajo, *Optical field enhancement by strong plasmon interaction in graphene nanostructures*, Phys. Rev. Lett. **110**, 187401 (2013). (see p. 91)

[176] F. N. Xia, T. Mueller, Y. M. Lin, A. Valdes-Garcia, and P. Avouris, *Ultrafast graphene photodetector*, Nat. Nanotech. **4**, 839–843 (2009). (see p. 91)

[177] Klaas-Jan Tielrooij, Lukasz Piatkowski, Mathieu Massicotte, Achim Woessner, Qiong Ma, Yongjin Lee, Kevin Scott Myhro, Chun Ning Lau, Pablo Jarillo-Herrero, Niek F van Hulst, and F. H. L. Koppens, *Generation of photovoltage in graphene on a femtosecond timescale through efficient carrier heating*, Nat. Nanotech. **10**, 437–443 (2015). (see p. 91)

[178] Mitchell Bacon, Siobhan J Bradley, and Thomas Nann, *Graphene quantum dots*, Part. Part. Syst. Charact. **31**(4), 415–428 (2014). (see p. 91)

[179] Weidong Tian, Supriyo Datta, Seunghun Hong, R Reifenberger, Jason I Henderson, and Clifford P Kubiak, *Conductance spectra of molecular wires*, J. Chem. Phys. **109**(7), 2874–2882 (1998). (see pp. 91, 92, and 144)

[180] Jeremy Taylor, Hong Guo, and Jian Wang, *Ab initio modeling of quantum transport properties of molecular electronic devices*, Phys. Rev. B **63**(24), 245407 (2001). (see p. 91)

[181] Michael Galperin and Abraham Nitzan, *Optical properties of current carrying molecular wires*, J. Chem. Phys. **124**(23), 234709 (2006). (see p. 91)

[182] Mads Brandbyge, José-Luis Mozos, Pablo Ordejón, Jeremy Taylor, and Kurt Stokbro, *Density-functional method for nonequilibrium electron transport*, Phys. Rev. B **65**(16), 165401 (2002). (see p. 91)

[183] Abraham Nitzan and Mark A Ratner, *Electron transport in molecular wire junctions*, Science **300**(5624), 1384–1389 (2003). (see p. 91)

[184] Rolf Landauer, *Spatial variation of currents and fields due to localized scatterers in metallic conduction*, IBM Journal of Research and Development **1**(3), 223–231 (1957). (see pp. 92 and 93)

[185] Supriyo Datta, *Electronic transport in mesoscopic systems*, Cambridge university press, London (1997). (see pp. 92, 93, 143, and 144)

[186] Massimiliano Di Ventra, *Electrical transport in nanoscale systems* volume 14, Cambridge University Press Cambridge, (2008). (see pp. 92, 93, 143, and 144)

[187] Abram L Falk, Frank HL Koppens, L Yu Chun, Kibum Kang, Nathalie de Leon Snapp, Alexey V Akimov, Moon-Ho Jo, Mikhail D Lukin, and Hongkun Park, *Near-field electrical detection of optical plasmons and single-plasmon sources*, Nature Physics **5**(7), 475–479 (2009). (see pp. 93 and 96)

[188] Kenneth M Goodfellow, Chitraleema Chakraborty, Ryan Beams, Lukas Novotny, and A Nick Vamivakas, *Direct on-chip optical plasmon detection with an atomically thin semiconductor*, Nano Lett. **15**, 5477–5481 (2015). (see pp. 93 and 96)

[189] Melinda Y Han, Barbaros Özyilmaz, Yuanbo Zhang, and Philip Kim, *Energy band-gap engineering of graphene nanoribbons*, Physical Review Letters **98**, 206805 (2007). (see pp. 98 and 101)

[190] Melinda Y Han, Juliana C Brant, and Philip Kim, *Electron transport in disordered graphene nanoribbons*, Physical Review Letters **104**, 056801 (2010). (see pp. 98 and 101)

[191] Patrick Gallagher, Kathryn Todd, and David Goldhaber-Gordon, *Disorder-induced gap behavior in graphene nanoribbons*, Physical Review B **81**, 115409 (2010). (see pp. 98 and 101)

[192] C Stampfer, J Güttinger, S Hellmüller, F Molitor, K Ensslin, and T Ihn, *Energy gaps in etched graphene nanoribbons*, Physical review letters **102**, 056403 (2009). (see pp. 98 and 101)

[193] Zhihong Chen, Yu-Ming Lin, Michael J Rooks, and Phaedon Avouris, *Graphene nano-ribbon electronics*, Physica E: Low-dimensional Systems and Nanostructures **40**, 228–232 (2007). (see p. 98)

[194] Manu Shamsa, WL Liu, AA Balandin, C Casiraghi, WI Milne, and AC Ferrari, *Thermal conductivity of diamond-like carbon films*, Applied Physics Letters **89**, 161921 (2006). (see p. 101)

[195] Eric Pop, Vikas Varshney, and Ajit K Roy, *Thermal properties of graphene: Fundamentals and applications*, MRS Bulletin **37**, 1273–1281 (2012). (see p. 102)

[196] Kathryn M Mayer, Seunghyun Lee, Hongwei Liao, Betty C Rostro, Amaris Fuentes, Peter T Scully, Colleen L Nehl, and Jason H Hafner, *A label-free immunoassay based upon localized surface plasmon resonance of gold nanorods*, ACS Nano **2**, 687–692 (2008). (see p. 107)

[197] Seunghyun Lee, Kathryn M Mayer, and Jason H Hafner, *Improved localized surface plasmon resonance immunoassay with gold bipyramid substrates*, Anal. Chem. **81**, 4450–4455 (2009). (see p. 107)

[198] Kathryn M Mayer, Feng Hao, Seunghyun Lee, Peter Nordlander, and Jason H Hafner, *A single molecule immunoassay by localized surface plasmon resonance*, Nanotech. **21**, 255503 (2010). (see p. 107)

[199] Chia-Sheng Cheng, Yu-Quan Chen, and Chia-Jung Lu, *Organic vapour sensing using localized surface plasmon resonance spectrum of metallic nanoparticles self assemble monolayer*, Talanta **73**, 358–365 (2007). (see p. 107)

[200] Kuan-Jen Chen and Chia-Jung Lu, *A vapor sensor array using multiple localized surface plasmon resonance bands in a single uv–vis spectrum*, Talanta **81**, 1670–1675 (2010). (see p. 107)

[201] Markus Nuopponen and Heikki Tenhu, *Gold nanoparticles protected with ph and temperature-sensitive diblock copolymers*, Langmuir **23**, 5352–5357 (2007). (see p. 107)

[202] Nathan H Mack, Jay Wm Wackerly, Viktor Malyarchuk, John A Rogers, Jeffrey S Moore, and Ralph G Nuzzo, *Optical transduction of chemical forces*, Nano Lett. **7**, 733–737 (2007). (see p. 107)

[203] Jeffrey N. Anker, W. Paige Hall, Olga Lyandres, Nilam C. Shah, Jing Zhao, and Richard P. Van Duyne, *Biosensing with plasmonic nanosensors*, Nat. Mater. **7**(6), 442–453 (2008). (see p. 107)

[204] Markus Lippitz, Meindert A van Dijk, and Michel Orrit, *Third-harmonic generation from single gold nanoparticles*, Nano Lett. **5**, 799–802 (2005). (see p. 107)

[205] Osip Schwartz and Dan Oron, *Background-free third harmonic imaging of gold nanorods*, Nano Lett. **9**, 4093–4097 (2009). (see p. 107)

[206] Jérémy Butet, Julien Duboisset, Guillaume Bachelier, Isabelle Russier-Antoine, Emmanuel Benichou, Christian Jonin, and Pierre-François Brevet, *Optical second harmonic generation of single metallic nanoparticles embedded in a homogeneous medium*, Nano Lett. **10**, 1717–1721 (2010). (see p. 107)

[207] J Butet, G Bachelier, I Russier-Antoine, Ch Jonin, E Benichou, and P-F Brevet, *Interference between selected dipoles and octupoles in the optical second-harmonic generation from spherical gold nanoparticles*, Phys. Rev. Lett. **105**, 077401 (2010). (see p. 107)

[208] Hayk Harutyunyan, Giorgio Volpe, Romain Quidant, and Lukas Novotny, *Enhancing the nonlinear optical response using multifrequency gold-nanowire antennas*, Phys. Rev. Lett. **108**, 217403 (2012). (see p. 107)

[209] Youngjin Kim, Robert C Johnson, and Joseph T Hupp, *Gold nanoparticle-based sensing of spectroscopically silent heavy metal ions*, Nano Lett. **1**, 165–167 (2001). (see p. 107)

[210] Anant K Singh, Dulal Senapati, Shuguang Wang, Jelani Griffin, Adria Neely, Perry Candice, Khaleah M Naylor, Birsen Varisli, Jhansi Rani Kalluri, and Paresh Chandra Ray, *Gold nanorod based selective identification of escherichia coli bacteria using two-photon rayleigh scattering spectroscopy*, ACS Nano **3**, 1906–1912 (2009). (see p. 107)

[211] Adria Neely, Candice Perry, Birsen Varisli, Anant K Singh, Tahir Arbneshi, Dulal Senapati, Jhansi Rani Kalluri, and Paresh Chandra Ray, *Ultrasensitive and highly selective detection of alzheimer's disease biomarker using two-photon rayleigh scattering properties of gold nanoparticle*, ACS Nano **3**, 2834–2840 (2009). (see p. 107)

[212] Martin Mesch, Bernd Metzger, Mario Hentschel, and Harald Giessen, *Nonlinear plasmonic sensing*, Nano Lett. **16**, 3155–3159 (2016). (see p. 107)

[213] F. H. L. Koppens, D. E. Chang, and F. J. García de Abajo, *Graphene plasmonics: A platform for strong light-matter interactions*, Nano Lett. **11**, 3370–3377 (2011). (see pp. 107 and 139)

[214] L. Wu, H. S. Chu, W. S. Koh, and E. P. Li, *Highly sensitive graphene biosensors based on surface plasmon resonance*, Opt. Express **18**, 14395–14400 (2010). (see p. 107)

[215] Y. Li, H. Yan, D. B. Farmer, X. Meng, W. Zhu, R. M. Osgood, T. F. Heinz, and P. Avouris, *Graphene plasmon enhanced vibrational sensing of surface-adsorbed layers*, Nano Lett. **14**, 1573–1577 (2014). (see p. 107)

[216] A. Marini, I. Silveiro, and F. J. García de Abajo, *Molecular sensing with tunable graphene plasmons*, ACS Photon. **2**, 876–882 (2015). (see p. 107)

[217] S. A. Mikhailov, *Non-linear electromagnetic response of graphene*, Europhys. Lett. **79**, 27002 (2007). (see p. 107)

[218] E. Hendry, P. J. Hale, J. Moger, A. K. Savchenko, and S. A. Mikhailov, *Coherent nonlinear optical response of graphene*, Phys. Rev. Lett. **105**, 097401 (2010). (see p. 107)

[219] J. D. Cox, I. Silveiro, and F. J. García de Abajo, *Quantum effects in the nonlinear response of graphene plasmons*, ACS Nano **10**, 1995–2003 (2016). (see p. 107)

[220] Xin Yan, Xiao Cui, and Liang shi Li, *Synthesis of large, stable colloidal graphene quantum dots with tunable size*, J. Am. Chem. Soc. **132**, 5944–5945 (2010). (see p. 107)

[221] Klaus Müllen, *Evolution of graphene molecules: Structural and functional complexity as driving forces behind nanoscience*, ACS Nano **8**, 6531–6541 (2014). (see p. 107)

[222] I. Silveiro and F. J. García de Abajo, *Plasmons in inhomogeneously doped neutral and charged graphene nanodisks*, Appl. Phys. Lett. **104**, 131103 (2014). (see pp. 107 and 108)

[223] Robert W. Boyd, *Nonlinear optics*, Academic Press, Amsterdam 3 edition (2008). (see pp. 107 and 108)

[224] S. Thongrattanasiri, A. Manjavacas, and F. J. García de Abajo, *Quantum finite-size effects in graphene plasmons*, ACS Nano **6**, 1766–1775 (2012). (see pp. 108 and 144)

[225] William M Haynes, *CRC handbook of chemistry and physics*, CRC press, London (2014). (see p. 111)

[226] BO Dabbousi, J Rodriguez-Viejo, Frederic V Mikulec, JR Heine, Hedi Mattoussi, R Ober, KF Jensen, and MG Bawendi, *(cdse) zns core-shell quantum dots: synthesis and characterization of a size series of highly luminescent nanocrystallites*, J. Phys. Chem. B **101**, 9463–9475 (1997). (see p. 111)

[227] Moonsub Shim and Philippe Guyot-Sionnest, *Permanent dipole moment and charges in colloidal semiconductor quantum dots*, J. Chem. Phys. **111**, 6955–6964 (1999). (see p. 111)

[228] I. Russier-Antoine, E. Benichou, G. Bachelier, C. Jonin, and P. F. Brevet, *Multipolar contributions of the second harmonic generation from silver and gold nanoparticles*, J. Phys. Chem. C **111**, 9044–9048 (2007). (see p. 112)

[229] Paolo Galletto, Pierre F. Brevet, Hubert H. Girault, Rodolphe Antoine, and Michel Broyer, *Size dependence of the surface plasmon enhanced second harmonic response of gold colloids: towards a new calibration method*, Chem. Commun. pages 581–582 (1999). (see p. 112)

[230] Isabelle Russier-Antoine, Julien Duboisset, Guillaume Bachelier, Emmanuel Benichou, Christian Jonin, Natalia Del Fatti, Fabrice Vallée, Ana Sánchez-Iglesias, Isabel Pastoriza-Santos, Luis M. Liz-Marzán, and Pierre-François Brevet, *Symmetry cancellations in the quadratic hyperpolarizability of non-centrosymmetric gold decahedra*, J. Phys. Chem. Lett. **1**, 874–880 (2010). (see p. 112)

[231] Anant Kumar Singh, Dulal Senapati, Adria Neely, Gabriel Kolawole, Craig Hawker, and Paresh Chandra Ray, *Nonlinear optical properties of triangular silver nanomaterials*, Chem. Phys. Lett. **481**, 94–98 (2009). (see p. 112)

[232] L. Novotny and B. Hecht, *Principles of Nano-Optics*, Cambridge University Press, New York (2006). (see p. 126)